



TECHNISCHE
UNIVERSITÄT
WIEN
Vienna University of Technology

DISSERTATION

Investigation of current filament behavior in smart power technology ESD protection devices subjected to long ESD-like pulses

ausgeführt zum Zwecke der Erlangung des akademischen Grades eines
Doktors der technischen Wissenschaften

Unter der Leitung von
a.o. Univ.-Prof. Dipl.-Ing. Dr. Dionyz Pogany
Insitute für Festkörperelektronik

eingereicht an der
Technischen Universität Wien
Fakultät für Elektrotechnik und Informationstechnik

Von
M.Eng. Wasinee Mamanee
Matrikelnummer 0627312
Chatchai 260/125, Lampang 52100, Thailand

Wien, im März, 2012

.....

Abstract

Due to downscaling of modern technologies, integrated circuits (ICs) are more and more vulnerable to the Electrostatic Discharge (ESD) pulses. ESD damage can occur during the manufacturing phase or operational state of the IC. Therefore every input output pin of an IC chip is protected by an ESD protection device. Such devices, operating in breakdown regime, have to sustain current pulses of the orders of Amperes for duration from ns to about 150 ns. In some applications, like automotive electronics, where smart power IC technology is used, the ESD protection devices have to sustain also longer pulses of the duration up to 1 μ s but with lower current amplitude. Former studies showed that the current conduction under such pulses occurs in a form of localized current filaments (CFs) which can move along the device active area. In this thesis, physical characteristics of single and multiple CFs and related device failure modes due to thermal breakdown are investigated in smart power technology NPN-transistor ESD protection devices. The work is important not only from practical point of view but also gives some new insight into current filament interactions in bistable semiconductor systems with S-shape current voltage characteristics.

The CF behavior was analyzed using transient interferometric mapping (TIM) technique which monitors thermal signals in the devices with ns time and μ m space resolution. The devices were electrically stressed by different kind of transmission line and solid state pulsers. The spatio-temporal behavior of the CFs in the devices is related to voltage waveforms, making thus a unique relation of internal device behavior to measured electrical parameters. Such knowledge can substantially simplify the device analysis and can be used for optimization of ESD protection devices to enhance their robustness.

The behavior of CFs has been studied in devices of linear, circular and oval geometries as well as in specially designed test structures. Basic properties of single CFs, like speed, size, stopping time, etc. have been analyzed. It was shown that the random position of the filament creation along the device width and the thermal prehistory due to previous current filament passage is crucial to understand the behavior of time to thermal breakdown t_{TB} in the devices. While in the linear devices t_{TB} is random, in the circular ones it is deterministic, making these devices suitable for ESD protection. It was found that complex multiple filament modes can occur at high current, where the thermal breakdown can occur due to redistribution of current between the current filaments, leading to shortening of t_{TB} in comparison to the single CF mode. As well other CF interactions, like meeting and splitting have been studied in details. The thermal prehistory due to multiple filament movement and CF interactions also plays crucial role in failure mechanisms.

Furthermore, the CF behavior has been studied as function of ambient temperature and temperature gradient along the device width, mimicking thus the operation of ESD protection devices in powered chips. In linear devices the time to breakdown is shortened step-wise with the increase of ambient temperature which was found to be consistent with the results of thermal simulations.

CHAPTER 1 INTRODUCTION	7
1.1 Motivation.....	7
1.2 Scope of thesis	8
1.3 Electrostatic Discharge	9
1.3.1 Three common models of Electrostatic Discharge.....	10
1.3.1.1 Human Body Model (HBM)	10
1.3.1.2 Machine Model (MM).....	11
1.3.1.3 Charged Device Model (CDM).....	12
1.3.2 ISO pulse	12
1.3.3 IEC 61000-4-2 (Gun test).....	15
1.4 Smart Power Technologies	16
1.4.1 DMOS as Smart power device	17
1.5 ESD Protection.....	18
1.5.1 On chip protection concept.....	18
1.5.2 ESD Protection Window	19
1.5.3 ESD Protection devices	20
1.5.3.1 Diode	20
1.5.3.2 NPN device.....	21
1.5.3.3 SCR device	22
1.6 Current filament phenomena	23
1.6.1 IV characteristic in aspect of Current filamentation.....	23
1.6.2 Theory of CF formation	25
1.6.3 On state spreading of inhomogeneous current distribution.....	25
1.6.4 Moving current Filament.....	26
1.7 Thermal Breakdown	30
1.7.1 Current filament during thermal breakdown event	31
CHAPTER 2 INVESTIGATION TECHNIQUES	32
2.1 Electrical Investigation by the Transmission Line Pulsing (TLP) system ..	33
2.2 Transient Interferometric Mapping Techniques	36
2.2.1 The extracted phase change due to induced temperature	38
2.2.2 Scanning Heterodyne Interferometer	39
2.2.3 Dual Beam Michelson Interferometer	41
2.2.4 2D Holographic Transient Interferometric Mapping	44

2.2.4.1	2D TIM at single time instant measurement	44
2.2.4.2	2D TIM at two time instant measurement	45
CHAPTER 3 EXPERIMENTAL RESULTS		49
3.1	Investigated Devices	49
3.2	Current Filament study	50
3.2.1	Randomness in triggering position of Current Filament	51
3.2.2	Initial time before traveling	52
3.2.3	Size of Current Filament	54
3.2.4	Speed of Single CF	55
3.2.4.1	Filament speed at room temperature by the electrical measurement	56
3.2.4.2	Filament speed at room temperature by Dual beam Michelson Interferometry	57
3.2.4.3	Filament speed at room temperature by Heterodyne Scanning Interferometry technique	59
3.2.5	Time consumption of CF at device edge	60
3.2.6	Heat energy profile	64
3.2.6.1	Heat energy distribution in the linear device	64
3.2.6.2	Heat energy distribution in the circular device	65
3.2.7	Temperature in the moving CF	66
3.2.7.1	Transient temperature at a fixed point on DE during CF turning around ..	68
3.2.8	CF as a probe of access resistance in different device shapes	69
3.2.8.1	Moving CF in Meander structure	69
3.2.8.2	Moving CF in Oval structure	73
3.2.9	Effect of buried layer resistance change during CF passage on the change in filament speed	74
3.2.10	Effect of preheated region induced by moving Current Filament	75
3.2.10.1	Effect of preheated region on the device voltage	75
3.2.10.2	Effect of preheated region on filament speed	76
3.3	Multiple Current Filaments	78
3.3.1	The dependence of filament numbers on stress current	78
3.3.2	Multiple current branches in IV characteristic	79
3.3.3	Size of Multiple Current Filaments	80
3.3.4	Nondestructive interaction between two filaments	81
3.3.4.1	Meeting of two filaments by 2D TIM	81
3.3.4.2	Meeting of two filaments by Heterodyne Scanning TIM	83
3.3.4.3	Splitting of two filaments by 2D TIM	85

3.3.4.4	Splitting of two filaments observed by Dual Beam Michelson Interferometry.....	86
3.3.4.5	Modified TLP setup for observing the splitting of CF	87
3.3.4.6	Controlled splitting of a CF	88
3.3.5	Comparison of single CF with two CFs	89
3.4	Thermal breakdown	90
3.4.1	Thermal breakdown of Single Current Filament mode.....	91
3.4.1.1	Effect of preheated passage on the thermal breakdown event	91
3.4.1.2	Effect of different widths on the thermal breakdown in linear structure ..	93
3.4.2	Thermal breakdown of Two Current Filaments mode	94
3.4.2.1	The early thermal breakdown of two CFs in linear device observed by 2D TIM technique	94
3.4.2.2	The early thermal breakdown as a result of CF disappeared on DE observed by the Dual Beams Michelson Interferometer technique.....	95
3.5	Temperature Effect on CF behavior	97
3.5.1	Effect of Elevated Temperature.....	98
3.5.1.1	Decrease of Filament Speed at the elevated temperature.....	98
3.5.1.2	The shortened time to Thermal Breakdown at the elevated temperature..	99
3.5.1.3	The consistency of thermal breakdown temperature in all devices at the elevated temperature.....	100
3.5.2	Effect of temperature gradient to filament behavior	103
3.5.2.1	The random distribution of triggering CF positions influenced by the temperature gradient.....	104
3.5.2.2	The shortened time to Thermal Breakdown under the temperature gradient.....	105
3.5.2.3	The controlled time to Thermal Breakdown under temperature gradient.....	107
3.6	Summary of CF(s) modes	108
CHAPTER 4 CONCLUSION		111
REFERENCES.....		114
LIST OF PUBLICATIONS.....		117
SYMBOLS AND ACRONYMS.....		119
ACKNOWLEDGEMENT.....		121
BIOGRAPHY.....		122

Chapter 1

Introduction

1.1 Motivation

Electrostatic discharge (ESD) normally occurs all around us in daily life. One is zapped by the ESD during touching a door knob, making a contact with a person, or slipping into a car. The events are perceived as a mild shock with small spark flashes between human body and the contacted objects. The charging mechanism involves two motion objects with at least one of them being insulator. The process is called tribology charging. The charge is built up giving rise to the potential difference causing the current flow. The discharge event is due to the charge flowing from a region with higher electrostatic potential to a lower potential region. In general the ESD events are more nuisance rather than serious threats, and will not damage properties.

On the one hand ESD event is considered to be a serious threat in semiconductor devices. Since the CMOS and the bilpolar-CMOS-DMOS (BCD) technologies have been developed to minimize the gate lengths, gate oxides, and depth of junction for shrinking transistor size and increasing their performance, the thinner conductive and non conductive regions in semiconductor devices cannot withstand high voltage and high current density generated by ESD event. The device failure due to ESD events approximately costs more than 40% than the design cost of circuits. [1] Therefore the reliability issue of electronic components becomes a very important industry's concern.

A semiconductor device is susceptible to ESD damage not only in wafer fabrication house, but also in assembly and packaging process, integration with ICs component, and during its normal operation. Hence the life time of semiconductor device can be shortened or its performance is lowered by ESD events. Consequently the ESD protection devices (ESD PDs) are necessarily fabricated on chip in order to comfort the using of electronics in various environments. In telecommunication applications, the Smart Phones, Navigation systems, and cordless devices are unavoidable from the ESD events. In automotive application, the electronic components in cars have to face with discharged high voltage pulses from humans.

Basically the ESD devices function as a low impedance path for discharging the high voltage of ESD pulses to ground. Therefore the chip designer should understand the consequence of high voltage stressing onto the device response and how the thermal energy dissipates in the ESD protection device. From an earlier study of Infineon's BCD technology ESD PDs it is known that device subjected to pulses in ESD time domain exhibits failure in a form of destructive current filaments [2]. However at low current and long duration stress the device can exhibit a current transport in a form of travelling non-destructive current filaments (CFs) [3]. In this thesis we focus on investigation of failure

mechanisms related to the regime with such traveling current filaments. The knowledge of this study is relevant for the optimization of device structure in the pre-silicon state, so before the chip fabrication. The current transport is investigated with unique technique called transient interferometric mapping (TIM) [4]-[5] which allows visualizing the position of CF at the interesting moment and relate it to the measured change in the device voltage. Behavior of single and multiple CFs is analyzed as a function of device layout, stressing conditions, ambient temperature and temperature gradient, the latter two emulating conditions in powered chips.

1.2 Scope of thesis

Although the former investigations have been made to understand the preliminary characteristics of current filament, there are still many doubts about CF behaviors in BCD ESD devices that will be elucidated in this thesis.

The content of study is categorized into three chapters as followed:

In this chapter, the common models for ESD testing that are typically found in most environments are discussed. And the standard ESD pulse (ISO pulses) used for testing the chip for the automotive applications has also been explained. Furthermore the Smart Power Technology is briefly introduced and some examples of the basic ESD protection device will be demonstrated how the devices function under the high voltage stressing. The aftermost part discusses about the S-shape IV characteristic relating to the formation of current filament and the thermal breakdown event.

The second chapter explains the electrical measurement and all optical techniques that used for investigating current filament characteristics. It begins with the Transmission Line Pulsing (TLP) system for electrical stressing the device under test (DUT). Subsequently the Transient Interferometric Mapping (TIM) techniques are used for recording the phase change in response to the induced temperature by CF, while the DUT has been applying with the ESD-like pulses generated from the TLP system or the solid state pulser (i.e. DMOS pulser). Various device structures and different doping profiles are investigated showing the trade offs between the linear, oval, meander, and circular structures of bipolar transistor devices.

The third chapter demonstrates the experimental results of 2D phase images and transient phases under stressing with different criterions of ESD pulses. The discussion about CF behaviors is deliberated according to the magnitude of current stress. The speed of localized CF, the time consumption at device end, and the time of standing CF are measured.

The temperature rise in the filament due to self-heating effect, the thermal breakdown, and the effect of ambient temperature and temperature gradient leading to the thermal destruction are experimentally investigated and compared to simulations. In addition, the multiple current filaments are observed in various device structures that they could lead to more complex situations and induce the temperature change in different manner.

Conclusion of filament behaviors in different ESD structures shall be addressed in the last chapter.

1.3 Electrostatic Discharge

Electrostatic Discharge (ESD) is subset of Electrical Overstress (EOS) due to exceeding of voltage and current in the range of several Kilo-volts and 1-10 A in a very small semiconductor device. Although ESD event occurs within a very short duration (in range of ns), the fatal device degradation can still happen in the ICs such as the shorted/opened wires in metallization layer, gate oxide damage, junction breakdown causing to the permanent damage..

The hot spot in Figure 1 (a) is created from overheating during ESD event in bipolar junction transistor device. At very high current of ESD pulse, the free carriers, with their high traveling speed and high energy, can knock atoms out from metal wires leading to opened/shorted interconnections demonstrated in Figure 1 (b). The damage due to the gate oxide breakdown is shown in Figure 1 (c).

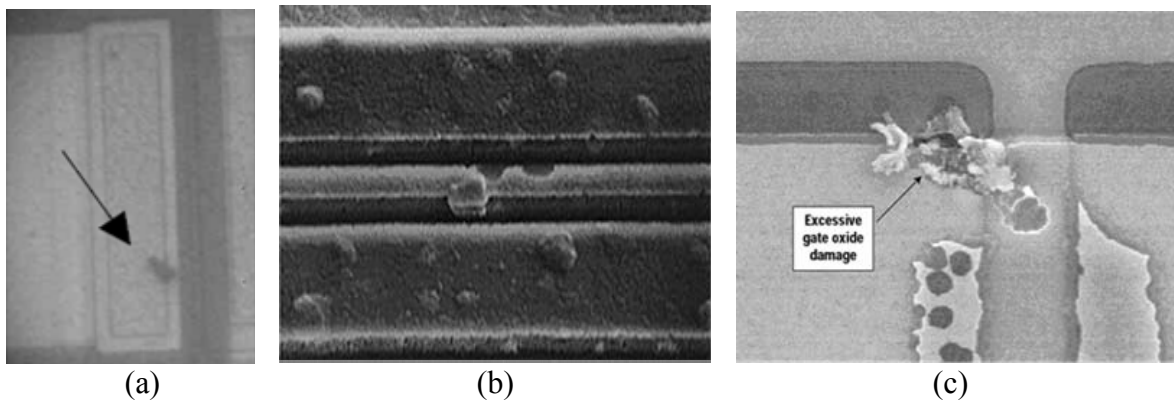


Figure 1 (a) Infrared image of the backside of NPN transistor device. Under ESD damage at high current stress, the dark spot happens at the emitter edge. [5] (b) Failure in the interconnection due to electro migration in the metal wires. [6] (c) Damage at the gate Oxide. [7]

The ESD phenomenon relates to the charge accumulating on a body or an object with increase of the electrical potential. ESD devices should withstand both positive and negative charges by serving as the conduction current path of ESD currents for both polarities. In general the amount of charges on an object depends on the process of charge generation, material characteristics and the dissipation sources.

For the automotive applications the ESD standard (ISO 10605: 2001) [8] substantially differs from the commercial ESD testing standard IEC 61000-4-2, which is commonly known as “ESD gun test” and is obligatorily required for all electronics component in Europe. [9]. In automotive areas the environment is harsh requiring the high robust ESD devices and high reliability than the others operations. ESD devices should operate efficiently at high temperature range and switch on immediately in case of fast rise time of ESD pulses. To meet the standard, the protection device should overcome more than 8 kV and is robust to different ESD pulse shapes with duration of about 100 ns to ms. The ESD Association agrees to classify three common ESD models as the standard testing to verify the reliability of the protection circuit including Human Body Model (HBM) [10], the Machine Model (MM) [11], and the Charged Device Model (CDM) [12].

1.3.1 Three common models of Electrostatic Discharge

The following three standards are universal methods for uniform testing in microelectronic industries.

1.3.1.1 Human Body Model (HBM)

The Human Body Model (HBM) is implemented on the purpose of simulating the discharged from human to grounded integrated circuits via a finger tip. The HBM model is one of the major ESD events that is frequently observed. For instance, as an operator walks along the floor, the electrostatic discharge accumulates in his body, and subsequently leads to an electric discharge to ICs components. HBM is modeled by a 100 pF capacitor (C_{HBM}) and discharged through a switching component and a series resistor (R_{HBM}) 1.5 k Ω . [EOS, MIL]. Figure 2 shows the circuit elements of HBM model; a C_{HBM} will be firstly charged by the high supply voltage ($V_{C,HBM}$), then discharged to the Device Under Test (DUT) via resistance R_{HBM} . The measured transient current across the short load (R_L) is demonstrated in Figure 3, when the high voltage ($V_{C,HBM} = 500$ V) discharge to the short via R_{HBM} . A typical rise time (t_r) has value of 5 ns to 10 ns, and the normal duration is between 100 ns to 150 ns.

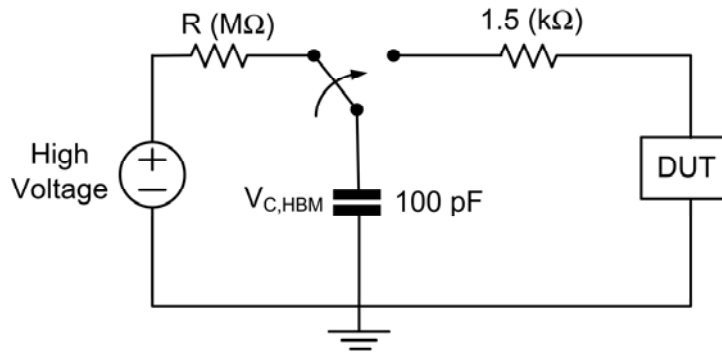


Figure 2 The circuit schematic for typical Human Body Model (HBM). [10]

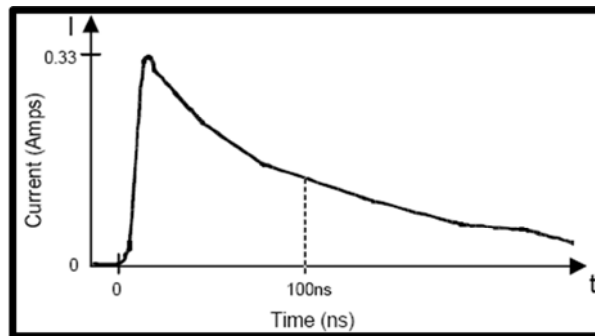


Figure 3 HBM waveform for a discharge through a short load ($R_L = 0 \Omega$) for the charged voltage 500 V. [13]-[14]

1.3.1.2 Machine Model (MM)

The accumulated static charges from equipment machine or metallic tool can discharge themselves through ICs device to ground during automated manufacturing or handling, called Machine Model (MM). For instance the fast discharge from metal contacts on a charged board or from a charged cable can discharge to IC components or from handle arms of automatic tester, introducing the more severe degradation than HBM. This model is unintentionally discovered during the attempt to create the worst case HBM event.

To test the device by Machine Model using ESD standard ESD STM5.2: Electrostatic Discharge Sensitivity Testing, the Machine Model as depicted in Figure 4 is nearly similar to HBM testing and comprises of the charged 200 pF capacitor (C_{MM}) for discharging directly to the ICs component without the series resistance ($R_{MM} = 0 \Omega$) to the output circuit. The MM does not have a series resistance to load as HBM version, and then the energy will be mainly dissipated through ICs. In the absence of R_{MM} the inductance (i.e. $L_{MM} = 0.5 \mu\text{H}$) becomes the important parasitic resistance, and it strongly influences to the shape of the MM waveform (see the responded waveform in Figure 5). The inductance value L_{MM} is indirectly defined in the model specification in the same fashion as other parameters such as rise time (t_r) or pulse duration. [11], [15]

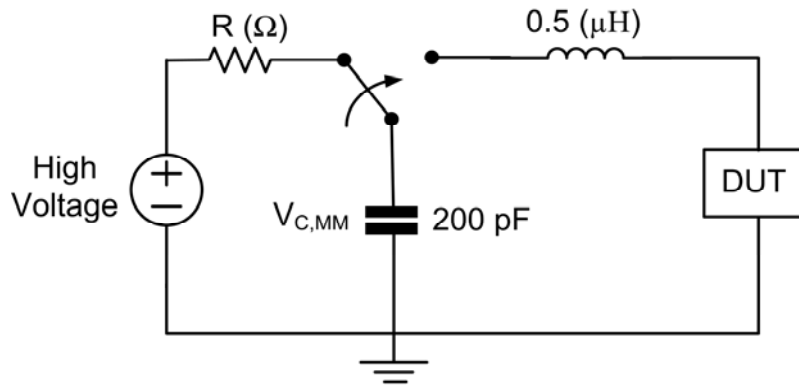


Figure 4 Circuits Model of Machine Model (MM) is alike HBM, however the series resistance here is zero. The total energy can dissipate in DUT, causing strong wear out. [15]

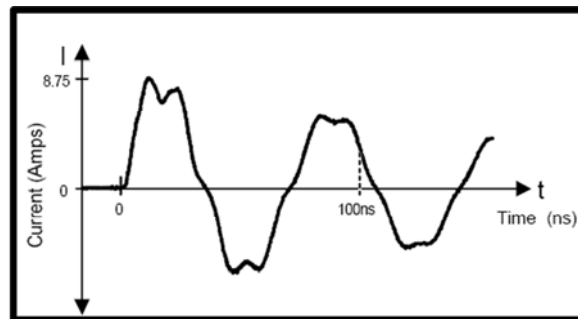


Figure 5 Current waveform of Machine model under the 500 precharged voltage ($V_{C,MM}$); the discharged is through a short ($R_L = 0$) with RC network ($C_{MM} = 200 \text{ pF}$, small $R_{MM} = 8.5 \Omega$, and inductance $0.5 \mu\text{H}$). [15]

1.3.1.3 Charged Device Model (CDM)

ICs can charge themselves and discharges to ground via some low impedance path (see Figure 6, $R_{CDM} \leq 25 \Omega$ and $L_{CDM} \leq 100 \text{ nH}$), this event is so called Charged Device Model (CDM). In a fabrication house, a device can be charged during the sliding down the feeder in an automated assembler. When a charged device contacts the insertion head or conductive surface that has a lower surface potential, the rapid discharge can happen from charged devices to the metal objects. Then the damage from CDM event commonly causes the gate oxide damages.

An example of CDM waveform is given in Figure 7; the typical rise time (t_r) is normally less than 1 ns and the pulse duration does not exceed nanosecond range. Even the pulse duration is very short; the peak current can reach several amperes. This current depends on the package type, which is defined by the capacitance to the grounded plate ($C_{chip-plate}$). To meet the requirements of automotive industry, the charged voltage should be compatible with the voltage value from 500 V up to 750 V. [12]

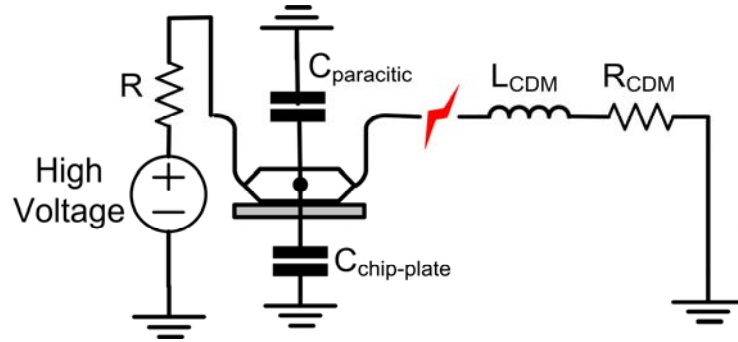


Figure 6 The typical Charged Device Model (CDM) circuits. [12]

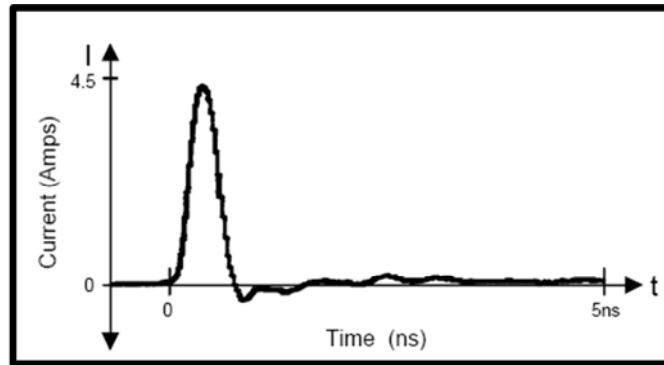


Figure 7 CDM waveform is measured from the investigated IC device under 500 V precharged voltage from another IC device. [12]

1.3.2 ISO pulse

With the increase of electronic components inside each vehicle, the electrostatic discharge becomes more critical situation. The testing of electrostatic discharge from Humans is

commonly used for various industry fields; however, it is not sufficiently applicable to automotive environment. Consequently, the appropriate ESD test for automotive application has been additionally developed.

The International Organization for Standardization [16] defined the main parameters of testing pulses for five standards as described in Table 1.

12V Battery system	Name	ISO-1	ISO-2	ISO-3a	ISO-3b	ISO-5
Maximum Over-Voltage	VMAX	-25 to -200 V	12 to 50 V	-37 to -150 V	25 to 100 V	22 to 87 V
Generator Internal Resistance	R _i	10 Ω	10 Ω	50 Ω	50 Ω	0.5 to 4 Ω
Pulse duration	t _d	2 ms	0.05 ms	0.1 μ s	0.1 μ s	40 to 400 ms
Rise time	t _r	< 1 μ s	< 1 μ s	< 5 ns	< 5 ns	5 to 10 ms
Period	t ₁	0.5 to 5 s	0.5 to 5 s	100 μ s	100 μ s	-
Supply switch-off duration	t ₂	200 ms	200 ms	-	-	-
Supply off duration before pulse	t ₃	< 100 μ s	-	-	-	-
Burst duration	t ₄	-	-	10 ms	10 ms	-
Burst period	t ₅	-	-	90 ms	90 ms	-
Test time	-	5000 pulses	5000 pulses	1 hour	1 hour	1 pulse

Table 1 Pulse shape parameters of ISO pulses in 12V battery system. [16]

Different automotive standards require different transient testing pulses (i.e. varied parameters such as amplitude, impulse, frequency, pulse energy, and pulse methods/test setup), which are probably caused by wiring harness, components, and generators, etc. The different ISO pulses and their circuit schematics are discussed as followed.

“ISO-1”- The ISO-1 pulse shape in Figure 8 (a) is designed for testing, monitoring the transient results from the voltage supply disconnection from inductive load. It applies to DUT, as used in a vehicle, which remains connected in parallel with the induction load (see Figure 8 (b)). The shunt resistor (R_{shunt}) models the resistance between the disconnected switch and ground. The pulse duration is in the range of milliseconds. During ISO-1 event ESD protection devices or DMOS devices can be driven to the saturation or the avalanche process.

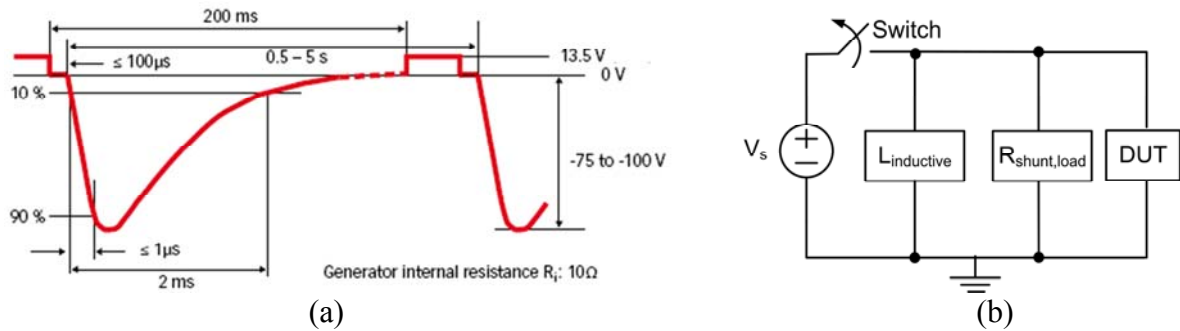


Figure 8 (a) Pulse shape (b) Circuit diagram for producing ISO-1 pulses. [16]

“ISO-2” – The ISO-2a pulse shape in Figure 9 (a) has a purpose to simulate the transient results due to the sudden interruption of currents through components. Circuits are connected in parallel with the DUT due to the inductance of the wiring harness, represented by the inductance symbol (L_{WIRING}) in Figure 9 (b). The maximum pulse duration is 50 μs . During ISO-2 event a DMOS device can be driven into the saturation regime.

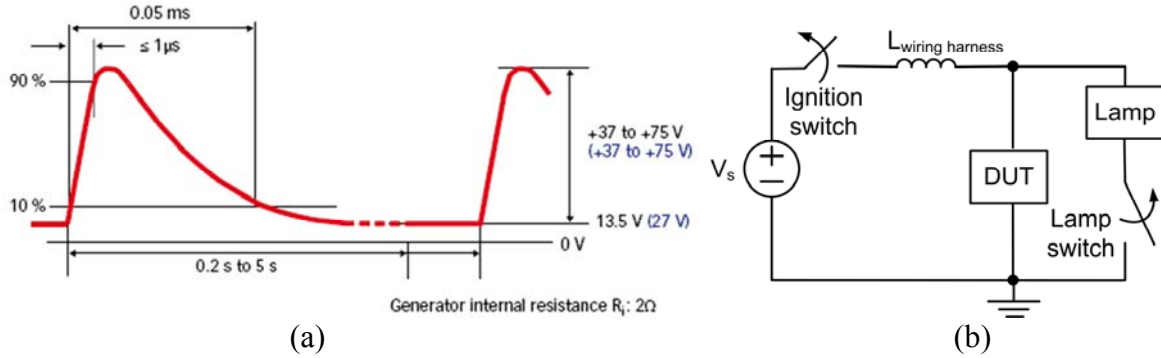


Figure 9 (a) Pulse shape (b) Circuit diagram for producing ISO-2a when load switch is opened. [16]

“ISO-3” – The ISO-3a and ISO-3b pulse shapes are designed to simulate the transient results, which occur as a result of switching processes (see waveforms in Figure 10 (a)). The characteristic of these transient pulses are due to the distributed inductance and capacitance of the wiring harness, represented in the simplified schematic in Figure 10 (b). The pulse duration of this pulse model will not exceed 100 ns, one burst consists of 100 pulses, and the burst period is 100 ms. Time and energy can be compared with the HBM model. These ISO pulses can lead to the saturation or breakdown regime.

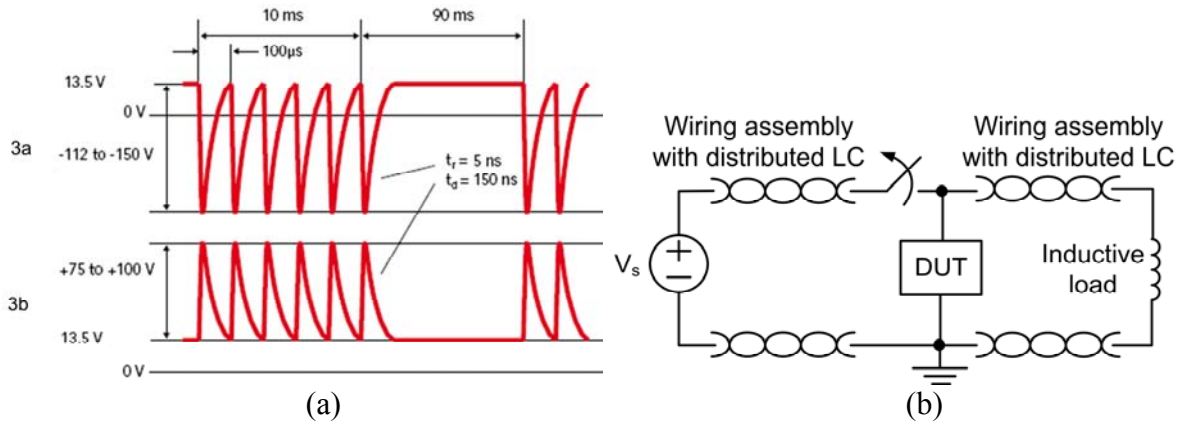


Figure 10 (a) Pulse shape for ISO-3a and ISO-3b (b) Circuit diagram for producing ISO-3a and ISO-3b. [16]

“ISO-5” – The ISO-5 pulse shape is designed to simulate the sharply rising voltage produced by the spinning alternators when the battery or another load is accidentally disconnected, see the pulse in Figure 11 (a) and the related circuit schematic in (b). The produced energy by the results of rising voltage is very high and can easily degrade the

unprotected internal devices. As a result, the disconnection of battery can be caused by cable corrosion or an intention disconnection.

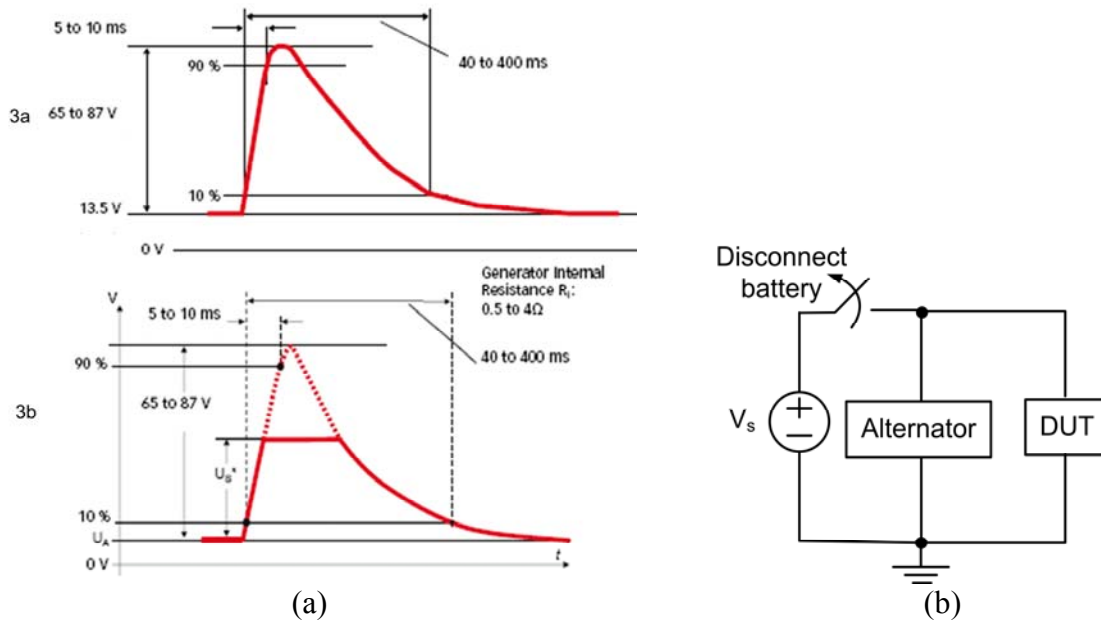


Figure 11 (a) Pulse shape for ISO-5a without load dump and ISO-5b with load dump. (b) Circuit diagram for producing ISO-5a and ISO-5b. [16]

1.3.3 IEC 61000-4-2 (Gun test)

The IEC 61000-4-2 standard was established for ESD testing in system level, not designed for stressing an individual component or an integrated circuit. [9] The general IEC standards intend to stress a single component; therefore the stressing of pins combinations is not addressed in the standard. Without the specification, the test engineers face off the variable in the output waveforms. Additionally, the commercial IEC generators could not meet the same specifications yielding the low reproducibility. The ESD association consequently develops the new standard defining the Human Metal Model (HMM) as the standardization of IEC 61000-4-2. To describe briefly the IEC 61000-4-2 standard, this standard could be classified into two main issues with respect to “Contact-discharge test” and “Air-discharge test”.

In Contact-discharge test [17], the ESD gun is charged and the gun tip should be contacted to the device surface to be stressed. The relay inside the gun is closed initiating the stress pulse. The output waveform can be characterized by the rise time (t_r) and the current magnitude at 30 ns and 60 ns (i.e. 53% and 27% of the peak current I_p), see the current waveform generated from the IEC gun pulser.

In Air-discharge testing, the relay inside the ESD gun initiating contact discharge remains closed throughout the test. The capacitor inside the gun and the gun tip are simultaneously charged; afterwards, the tip of ESD gun is moved toward the observing stress point until the arc forms.

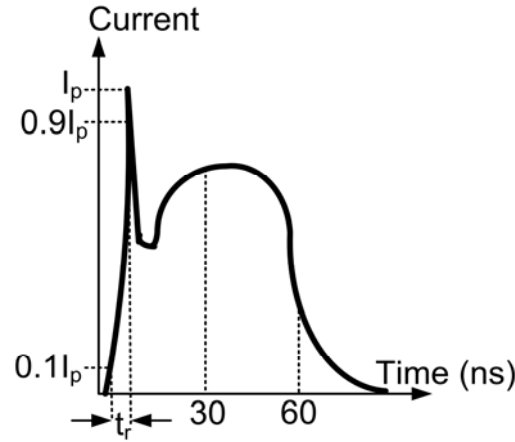


Figure 12 Contact-current waveform is generated from the IEC 61000-4-2 generator. [9]

The reference [18] demonstrates that the IEC 61000-4-2 generators can charge the DUT before the real ESD pulse is applied. This pre-pulse voltage (PPV) leads to the problems with $\frac{dV}{dt}$ -triggered ESD PDs by introducing the delayed avalanche breakdown in

silicon junctions. This is a critical phenomenon for the ESD Protection Devices, which requires the fast switching time. The present of PPV could introduce a different failure mechanism due to the delayed time in avalanche breakdown process.

To stress the various electronic components in automotive applications, the pulse standard must be appropriately chosen for each field. In this study, the parameters of stress pulse are similar to the HBM model, which are the fundamental specification used widely by the test engineers.

1.4 Smart Power Technologies

The Smart Power devices have functions like power control, sensing, protecting and interfacing, etc. The smart power devices can be classified by the isolation technique, by the power structure, or by the position of drain/collector contact. A simple cross section of general Smart Power devices is demonstrated in Figure 13. The current path in the smart power device allows very high current flowing in the vertical direction, and makes this technology to be low on-resistance (R_{on}) for fast switching. [19] In order to have low on-resistance during switching, the silicon area would be more consumed. Therefore this technology requires paying more expenses for fabrication. For instance, the design of DMOS (Double diffused MOS) will consume more than 50% of silicon area, and then it should take into account of on-resistance R_{on} .Area, which strongly depends on the thickness of N-Epi thickness, see the next examples of general smart power devices.

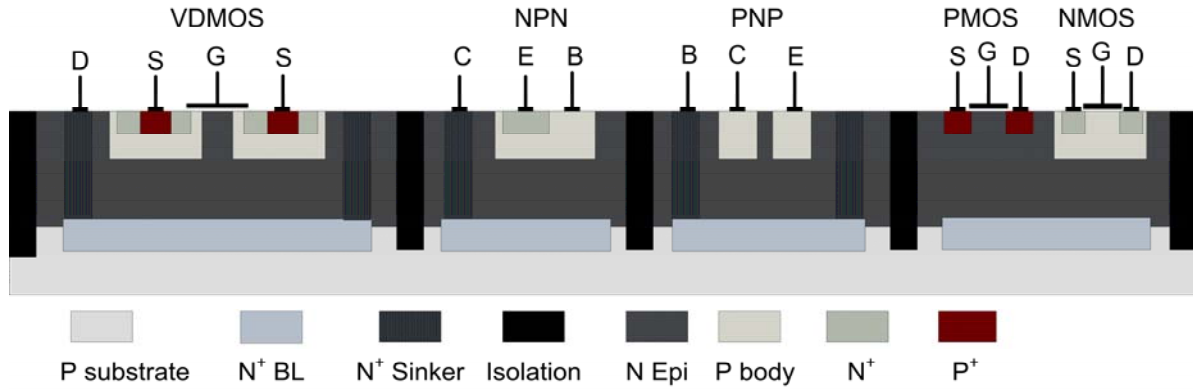


Figure 13 Overview of various devices in a Smart Power Technology. [19]

1.4.1 DMOS as Smart power device

The smart power technology (SPT) becomes more and more important as the microelectronic devices move towards the system integration. A smart power chip powerfully integrates the DMOS (power), CMOS (logic) and bipolar transistors (analog) within one substrate, building up the Smart Power System based on Silicon. A single chip contains several integrated power devices without connection wires.

The cross section of two vertical DMOS device (VDMOS) with n-channel is depicted by Figure 14 and the cross section of lateral DMOS (LDMOS) is demonstrated by Figure 15. The layout of smart power device is required to electrically isolate individual devices on the same chip. The crosstalk between different parts of ICs is unavoidable. This trouble is resolved by the junction isolation. Another possible resolution is done with the silicon on insulator (SOI) technology [20]. ESD robustness is an important aspect to concern for the smart power device that was formerly investigated in [21].

The smart power technology process starts with P-doped substrate, the highly doped N⁺ Buried Layer and P⁺ bottom isolation are implanted. Subsequently, a low N-doped Epitaxy layer is developed and P⁺ top isolation are then implanted. Then N⁺Sink is grown for contacting the buried layer to the surface pad. The P-body and N⁺Source regions are diffused to the self-aligned N-Epi layer through the opening of Polysilicon gate. The channel length is a consequence of the differential out-diffusion of the P⁺ and N⁺dopants, so called "Double Diffused". This technique is independent of the lithography process accuracy. The P-body and N⁺ are short-circuited to fix the potential voltage during the operation.

The difference between VDMOS and LDMOS devices is the direction of current flow. For VDMOS the electron current flows vertically through the N Epitaxy layer presented by the downward arrow in Figure 14. In LDMOS device the drain is formed by shallow N⁺ region. This shallow drain induces the lateral current flow along the top silicon surface depicted by the horizontal arrows in Figure 15.

To achieve high breakdown voltage at the reverse biased N-Epi/P-body junction, the doping concentration of N-Epi layer should be low. The impedance of N-Epi layer strongly influences to on-resistance (R_{on}) of device that is required to be minimized. In order to achieve the low value of R_{on} , the doping concentration of N-Epi should be increased.

Additionally the DMOS technology should be cautiously designed with concerning of the tradeoff between breakdown voltage (V_{BD}) and on-resistance. [19]

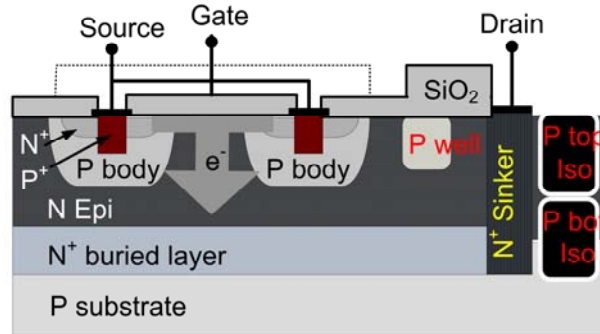


Figure 14 Schematic of cross section for Vertical DMOS (VDMOS). [19]

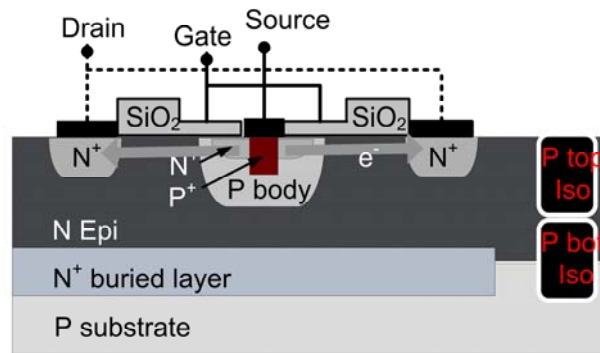


Figure 15 Schematic of cross section for Lateral DMOS (LDMOS). [19]

1.5 ESD Protection

1.5.1 On chip protection concept

Nowadays all ICs components that incorporated with the vehicles have continued to shrink their geometries. The integration of digital and analog become very dense with the independent power/ground, and its ICs package must be more fastened. The minimized semiconductor device is prone to encounter with the Electrostatic Discharge (ESD) event that associates with the transferring of electrostatic charge between two objects with different electrical potentials. Most of ESD events are unintentionally caused by discharging from human, charged devices, and operating machines.

The ESD protection circuits are one of serious concerns for enhancing the reliability of electronic components. The ESD failure is catastrophic phenomena causing the intermediately interrupted function of the whole IC chip. The failures are frequently caused by thermal degradation in silicon bulk, or metal disconnection, or dielectric breakdown in gate oxide due to high current and high voltage overstress [22].

In order to withstand multiple ESD pulses, the On-Chip protection circuits [23]-[24] have to be incorporated at every Input- port, Output- port, and power pads limiting the voltage across the internal circuits. The On-chip ESD PDs can securely clamp high voltage

down to safety value by converting electrical energy into heat dissipation. The triggering of protection devices must be certainly activated during ESD event; nevertheless, the ESD PDs should be “hidden” during the normal operation of ICs. The ESD protection circuits should sustain ISO pulses at high current in harsh environment (i.e. temperature in range of -40 to 200 °C for automotive applications). The location of the internal circuits together with perfect protection circuits are illustrated by Figure 16. [25]

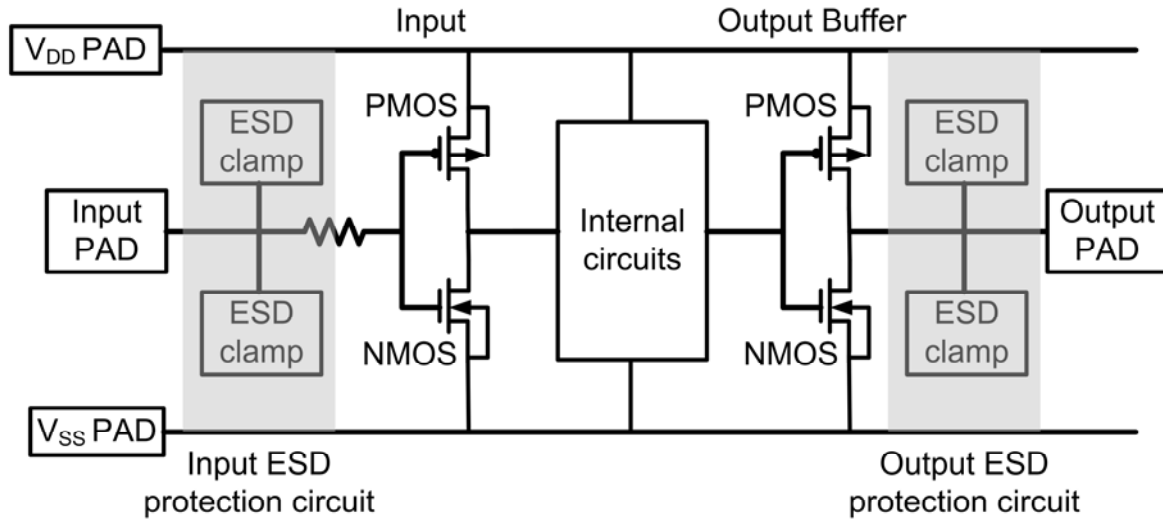


Figure 16 The schematic presents the location of ESD Protection Devices (PDs) incorporated with internal Integrated Circuits. [25]

1.5.2 ESD Protection Window

The ESD protection devices (ESD PDs) have to cope with two basic purposes. One is to clamp the voltage at each I/O pin down to a value below the gate oxide breakdown ($V_{BD,OX}$). Another purpose is to lower the current below the thermal failure (the second breakdown).

The IV characteristic of ESD PDs should align within the designed protection window (see Figure 17); they should be triggered below the breakdown voltage of ICs for preventing the oxide breakdown ($V_{BD,OX}$). According to the miniaturizing technology, the oxide breakdown tends to shift toward left direction (see the horizontal arrows), while the limit of thermal failure moves continuously downward (see the vertical arrows). The trend of ESD design window becomes smaller and smaller in order to fit into the shrinking window of future technology.

To align the S-shape IV characteristics into the ESD protection window, the ESD PD should be activated at voltage V_{t1} (at trigger current I_{t1}) to enter on state, see Figure 17. After the device is activated, the high voltage will be clamped to a lower safe value, called the holding voltage (V_H). The holding voltage should not lie within the operating regime of internal ICs and the safety margin area for preventing the interruption of ICs operation. More heat has been continuously accumulated until the temperature reaches the limit of thermal failure threshold at second breakdown voltage V_{t2} at the failure current ($I_{FAIL} = I_{t2}$). The generated heat can physically change the device properties leading to the device degradation or malfunction.

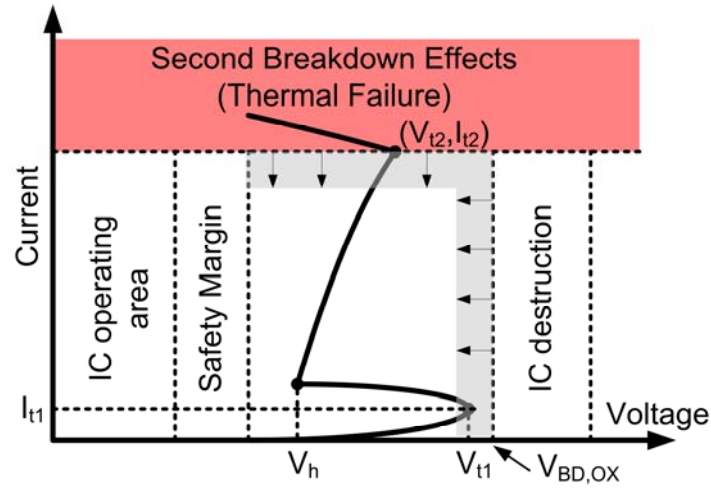


Figure 17 ESD Protection Window shows the S-Shaped IV characteristic of a clamp ESD device with the shrinking window for future technologies.

The negative temperature coefficient has a strong influence to the avalanche breakdown of ESD device. Then the demanding of a safety margin that achieves the 6-Sigma standard is required. For instance, the temperature drift of -2 V at $T = -40^{\circ}\text{C}$ and plus a breakdown variance $\sigma = 1\text{ V}$, the additional offset voltage value becomes $|-2| + 6.1 = 8\text{ V}$ [26]. Hence the ESD design window should protect ICs under the fluctuation and temperature variation effect.

1.5.3 ESD Protection devices

To integrate the ESD PDs with integrated circuits in the CMOS technology, various type of ESD devices have been developed. As the IC designer requires miniaturizing chip area with high switching speed, the evolution of protection circuits has been developed to against higher ESD level with longer duration. The PD devices should be improved its discharge ability with low power consumption, and behaves itself as high impedance and low capacitance for avoiding some disturbance during internal ICs operation. Some examples of effective ESD PDs in smart power technology such as diodes, NPN transistor and Silicon-controlled rectifier (SCR) are discussed below.

1.5.3.1 Diode

One of the simplest ESD protection devices is the diode. In CMOS technology two categories of diodes are illustrated by the schematics of Figure 18. The top schematic of PN diode in Figure 18 (a) is formed by the junction of P^+ Diffusion/N-well on P-substrate. For the middle schematic, the NP diode is formed by the junction of N^+ Diffusion/P-well without isolation to the P-substrate. Incorporated PN and NP devices with floating P-substrate can protect both negative bias and positive bias (see the circuit schematic at the bottom schematic). By integrating the circuits with these diodes can withstand a large current within device with very small dimension. [27]-[28]

Another type of PN diode is the vertical high voltage diode presented by Figure 18 (b) [26]. This diode type is capable to clamp the reverse breakdown voltage, which has

superior performances beyond the diodes in Figure 18 (a). The breakdown voltage takes place at the bottom of the P-body/N⁺Buried Layer (N⁺BL) junction that locates deep in the bulk of silicon for an excellent heat sink property. The planar of PN junction (marked with the eclipse) has a large area building the uniform current conduction under the reverse breakdown voltage.

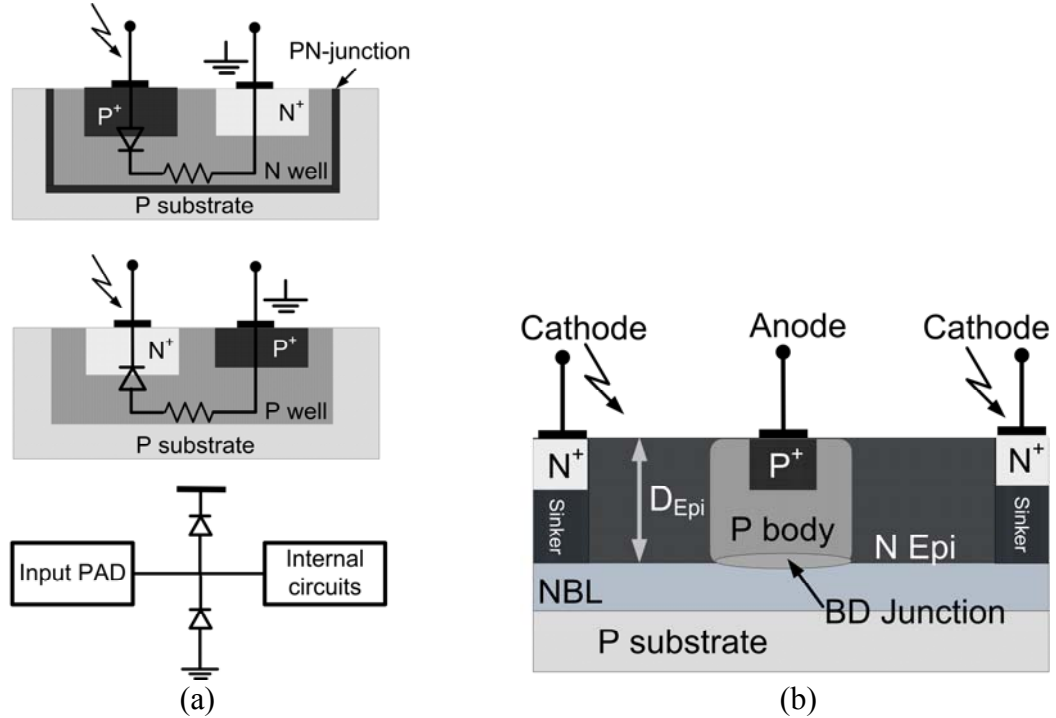


Figure 18 (a) Top: Cross section of P⁺/N-well diode, Middle: Cross section of N⁺/P-well diode, Bottom: The circuit schematic of ICs with two incorporated diodes. (b) The layout of vertical high voltage diode. [26]-[27]

1.5.3.2 NPN device

The parasitic NPN in NMOS device is another type of ESD device (see Figure 19). The junction of N⁺drain/P-well and the junction of N⁺source/P-well are applied with reverse bias and forward bias respectively, forming the parasitic lateral NPN transistor. During the normal operation, the gate voltage (V_G) is grounded in order to ensure the device in “off” state ($I_{sub} = 0$ A). Then the ESD pulse is applied at drain ($V_D > 0$ V), the electric field across the depletion region between N⁺drain/P-well becomes sufficiently high to exhibit the avalanche multiplication. Subsequently the free electron-hole pairs are generated. The electrons flow to high potential at the drain, and the holes are attracted to the low potential in substrate. The holes current in substrate (I_{sub}) raises the potential across base due to the existence of substrate resistance (R_{sub}). When the substrate potential is enough to forward bias the N⁺source/P-well, the parasitic NPN can be triggered on. The ESD current can be discharged from drain to ground via this lateral NPN. The turn-on time of parasitic NPN depends on the dimension of base width that is equivalent to the channel length of nMOS transistor. Therefore the channel length should be minimized for the small turn-on time but the punch through limited in channel will be affected. [27]

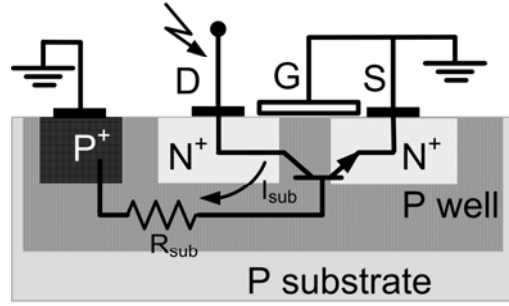


Figure 19 The cross sectional of parasitic lateral NPN in Grounded-Gate nMOS device. The drain is stressed with positive voltage, and the gate/source are shorted to ground. [27]

1.5.3.3 SCR device

The Silicon-Controlled Rectifier (SCR) device is widely implemented as ESD PD. The cross section of SCR device is displayed by Figure 20 (a). During the normal operation, the PN junction of N-well/P-substrate has been reverse biased and the SCR device has not been activated. During the ESD event, the PN junction between N-well/P-substrate is biased in the reverse direction, creating the avalanche multiplication process. The current flows from N⁺Diffusion through R_{Nwell} to substrate. With the sufficient voltage drops across a parasitic R_{Nwell} , the vertical PNP transistor (T1) is switched on. Therefore the large ESD current can flow from P⁺Diffusion through the parasitic resistance in substrate (R_{sub}) to the ground. Once the voltage drop across the R_{sub} increases and is sufficient to trigger on the lateral NPN bipolar device (T2). These two transistors latch up to release the ESD stress current to ground. In case of the negative ESD pulse, the lateral NPN transistor (T2) will only be triggered on.

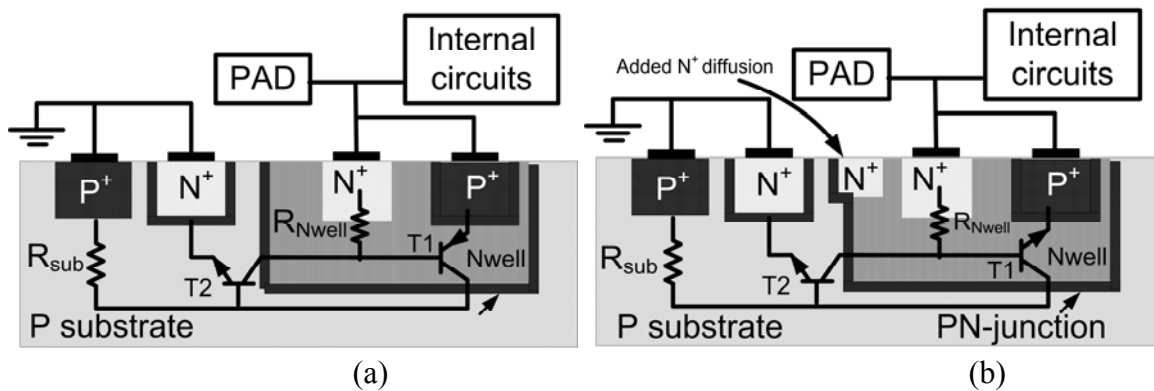


Figure 20 (a) The simplified cross section of the Silicon-controlled rectifier (SCR) device comprises the vertical PNP and the lateral NPN transistors. (b) The simplified cross section of the Silicon-controlled rectifier (SCR) device with modification by adding a N⁺ diffusion at the N-well/P Substrate junction. [27]

The SCR device behaves as the high breakdown device because the voltage across PN junction of N-well/P-substrate is higher than the voltage drop across the junction of N⁺Diffusion/P-substrate. Nevertheless, the highly triggered voltage has a drawback, whose

effect leads from the early destruction in the internal circuits before the ESD PDs will be activated. The solution has been achieved by adding the N^+ Diffusion to the junction of N-well/P-substrate for bringing the avalanche multiplication process to happen at lower breakdown voltage, and reducing the junction width of N-well/P-substrate (see the device cross section in Figure 20 (b)).

The bipolar ESD device in Figure 21 is developed for using in the harsh environment. Once the positive pulse is applied at the cathode via N^+ Sinker, the vertical PN diode at the junction of P-body/ N^+ BL undergoes avalanche breakdown generating the holes current to P-body (base). The holes current flows through the parasitic resistor R_{NPN} increasing the voltage drop across the emitter/base junction of the vertical NPN. Thereafter the NPN device is triggered on, and the electrons from collector flow into the substrate biasing the parasitic resistance in buried layer (R_{PNP}). Then the lateral PNP is subsequently activated. By coupling of lateral PNP to vertical NPN, the uniform current distribution could be achieved. [29]

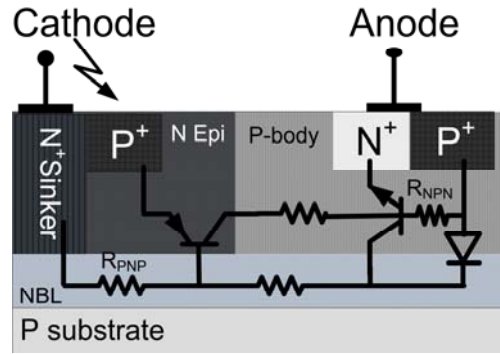


Figure 21 the cross section of High voltage bipolar device composes of the vertical NPN and lateral PNP transistors. [29]

The ESD protection devices with different layouts and varied doping concentration were explored here for the study of CF behavior, which will be discussed directly in sub topics of the experiment chapter. With the investigation of CF behavior, the experimental results made us understood how the device shape and the doping concentration influence on moving CF and the temperature distribution in various devices. Therefore, one could design a robust ESD protection device exploiting the knowledge of this dissertation.

1.6 Current filament phenomena

1.6.1 IV characteristic in aspect of Current filamentation

The S-shaped IV characteristic of ESD PD demonstrates the significant voltage drop to lower voltage, see Figure 22. The voltage drop from the bistable point “X” (at V_{TR}) to the voltage of AB branch (at U_{CO}) determines the transition from homogeneous to inhomogeneous current distribution. The averaged current density $\langle J \rangle$ can homogeneously distribute throughout device with a small width. But the current distribution becomes inhomogeneous in a large device width. Within the Negative Differential Resistance (NDR)

regime, inhomogeneous current or the Current Filament (CF) is formed in the device with sufficiently large width (W_D). [30]-[31]

The inhomogeneous current can be seen in large variety of ESD PDs [32], but also in the other devices such as power thyristors, CMOS, and DMOS that exhibit the S-shape IV characteristic. [33]-[35]

The CF formation is considered as isothermal and possibly destructive event for the ESD PD; however, in practical the localizing CF inducing the temperature change can inevitably effect to the device reliability. For the benefit of all, the CF behaviors and the induced temperature are worthy investigation.

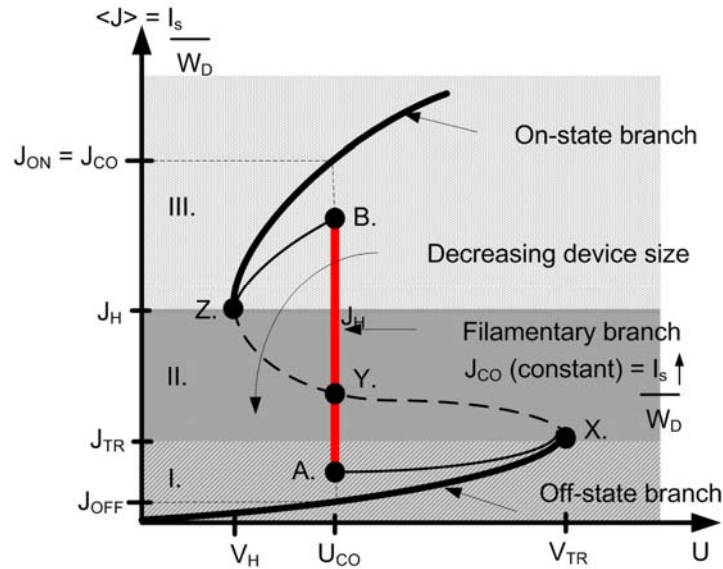


Figure 22 The S-Shape IV characteristic exhibits the NDR regime where the inhomogeneous current flows observed in a large device width. The vertical branch (AB) presents in the large W_D and the inclined slope of negative resistive branch (XYZ) is observed in relevant to the smaller W_D . [30]

The CF behaviors can be classified by considering the current magnitude along IV characteristic into three regimes as followed, see three shaded areas (I, II, and III) in Figure 22:

“Off state branch” (lies in “I” regime) is defined by the device voltage (U) below the triggered voltage ($U < V_{tr}$), where the current density is $J < J_{tr}$. The ESD PD device is in the off-state and the emitter-base junction is unbiased.

“On state branch” (lies in “III” regime) is specified for $U > V_H$ and $J > J_H$, where V_H is the holding voltage. The ESD device is fully switched on allowing the high current to flow. The emitter-base junction is forward biased and the transistor device is fully switched on allowing the ESD current to flow to the ground.

“NDR branch” (lies in “II” regime) is determined by $V_H < U < V_{tr}$ and $J_H > J > J_{tr}$. In general, this NDR branch could not be observed by the conventional TLP measurement, but possibly accessed by the modified multilevel TLP (ML-TLP) system as this technique offers a steep load line. [30] Within this hidden regime, the current instability and the CF formation can be observed in the snapback devices that are primarily discussed in this study.

1.6.2 Theory of CF formation

The vertical IV branch AB (see Figure 22) exhibits a nearly zero differential resistance in large device (Along the line of OFF + XA + AB + BZ + ON). A negative differential resistance region can be visible as the device width decreases, see Fig.25; the XYZ branch is found in small device width with large load resistance (Along the line of OFF + XYZ + ON). By increasing the stress current (I_S) along the AB branch, the device voltage remains nearly constant at the coexistence voltage (U_{co}). The U_{co} allows the device to exhibit both On-state and Off-state leading the unstable state within NDR branch. [36]

The NPN device studied by us exhibits the S-shaped IV characteristic. The collector/base junction is stressed with the positive ESD pulse via N^+ Sink in reverse biased direction. Once the reversed junction reaches the avalanche breakdown (V_{BD}), the avalanche multiplication process forms the homogeneous current distribution; see schematic A in Figure 23. In the wide junction, for currents above I_{TR} the current density $\langle J \rangle$ loses its balance as illustrated by schematic B. These phenomenon responses to the change from uniform current in off state to the non-uniform current in bi-stable region $V_H < U < V_{TR}$ state (see Figure 22). As a result, the homogeneous current distribution contracts itself to form the non-uniform current density pattern, called current filament (CF). The current flow in the CF corresponds to the high-conductivity on-state (high $\langle J \rangle$), while the current flow in the off-state corresponds to the low conductive off-state (low $\langle J \rangle$). [36]

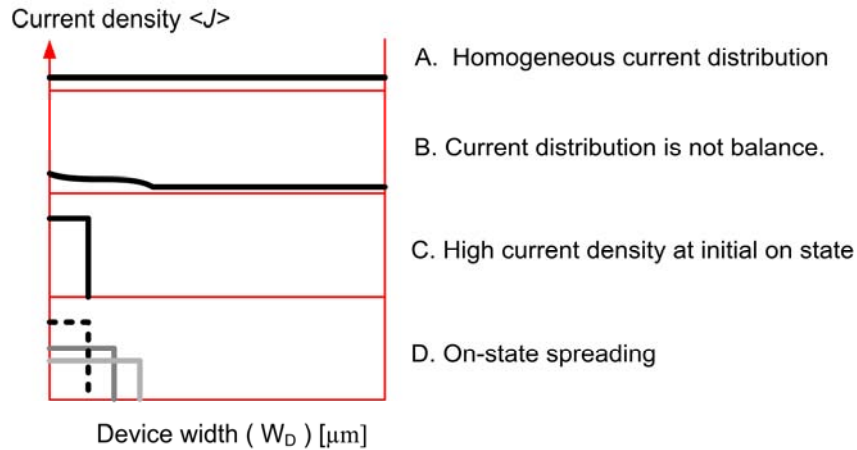


Figure 23 Due to the current instability of large device width, the homogeneous current distribution in Off-state changes to the inhomogeneous current distribution leading to the locally high current density, forming thus a CF. [36]

1.6.3 On state spreading of inhomogeneous current distribution

The on-state spreading is a phenomenon which occurs in every device with S-shape IV characteristics, at the transition between the low conductivity off-state and high conductivity on-state [30], [36], [37]. In the off state at low current (I_S) of IV characteristic,

the current density $\langle J \rangle$ of point 0 in Figure 24 (a) distributes homogeneously throughout the device width (W_D). If we bias the device at constant voltage and trigger it over the trigger point (e.g. by a short voltage pulse) then current distribution will collapse into the high on-state with current density $\langle J \rangle$ within a small area (W_1), see Figure 24 (b). This initial on-state will spread with a constant speed until reaching final current condition. In case of the current in the triggered device increases from points 1 to point 3 at a constant voltage (i.e. $V_{TR} > U > U_{CO}$ at the dashed vertical line), the constant $\langle J \rangle$ expands laterally at a constant speed from W_1 to W_3 , where the W_1 , W_2 and W_3 are determined from;

$$W_{1-3} = \frac{I_s}{J}$$

So long as the current increases further along the vertical branch, the profiles of current distribution have continuously expanded from partial width of on-state W_1 to W_2 and W_3 respectively, so called the on-state spreading. The on-state spreading will stop whenever the current homogeneously distributes from one device wall to another wall ($W_4 = W_D$). From point 4 onwards, the entire width is fulfilled with the homogeneous current turning the device into on-state. At a further increase current (i.e point 5) the magnitude of current density will uniformly increase throughout the W_D .

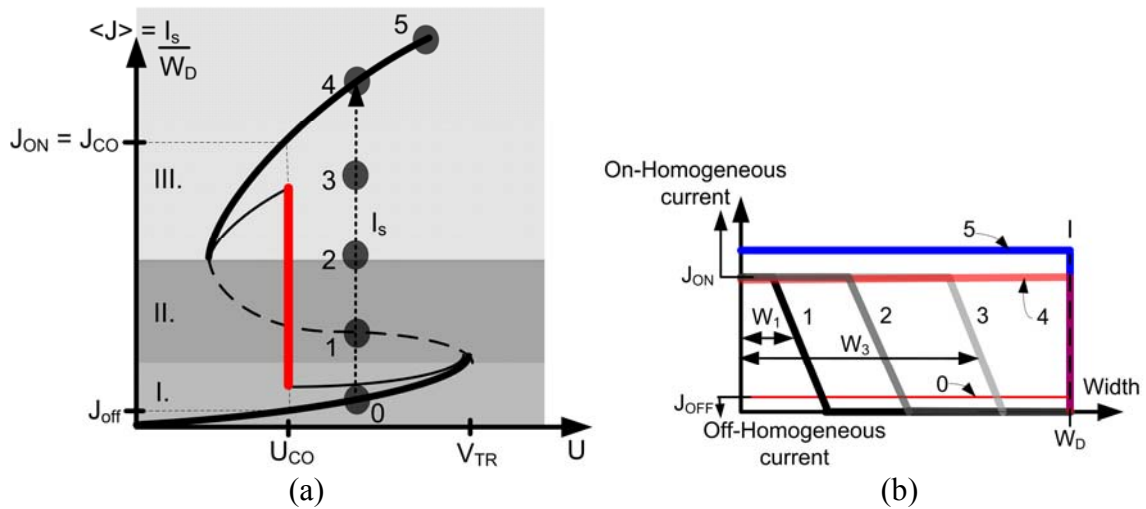


Figure 24 (a) The vertical branch in IV characteristic are marked with five points; 0 = Homogeneous current in off-state, 1-3 = On-state spreading, 4 = homogeneous current flow over the width, and 5 = On-state of homogeneous current with a higher current density. (b) The profiles of current density are presented for currents marked with five points in (a). [36]

1.6.4 Moving current Filament

CF movement is an effect which is different to the on-state spreading. The latter effect is an isothermal transient effect. For $I > I_{TR}$ and $I < I_{CO}$ (see Figure 24 (a)) a stable

current filament with a width $W_F = \frac{I}{J_{CO}}$ will originate after some transit time. [30] This time is composed of time corresponding to the time necessary to form the initial on-state at the moment of bipolar triggering and the time related to on-state spreading. In the studied devices, exhibiting the S-shaped IV characteristic of Figure 25, this time is about or below 1 ns. After this time all effects occur due to temperature rise in CF.

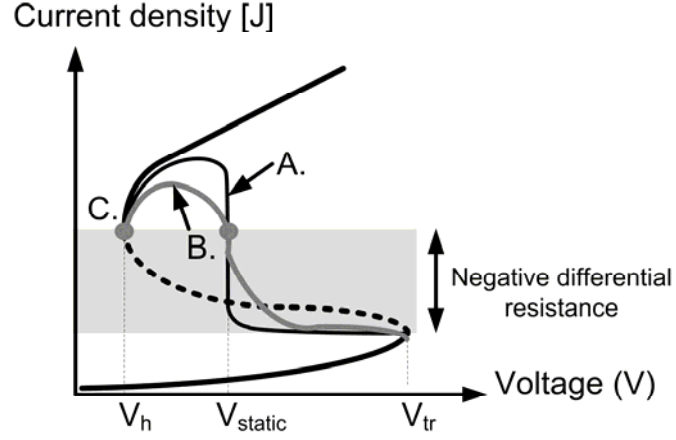


Figure 25 The NDR branch in S-shaped IV characteristic has the nearly zero resistance in the large device width (curve A), and the negative resistance in a smaller device width (curve B).

The CF movement is a result of self-heating effect [3]. At the pulse beginning the temperature in CF rises from the avalanche multiplication process. The temperature at initial CF location (within W_{CF}) has symmetrical profile. With progressing time, the temperature can fluctuate and transform its symmetrical profile into asymmetric profile, and then the impact ionization rate at the front wall becomes larger than in its middle. This temperature gradient between front wall (T_{FRONT}) and back wall (T_{BACK}) can drive CF to move, see the temperature distribution and $\langle J \rangle$ inside the moving CF in Figure 26 [3]. At the back location, the wall will be heated for the longest time, where T_{BACK} has the maximum temperature. The motion of CF in the linear structure of bipolar device was experimentally demonstrated in [38]-[39] by exploiting the 2D Transient Interferometric Mapping technique (TIM).

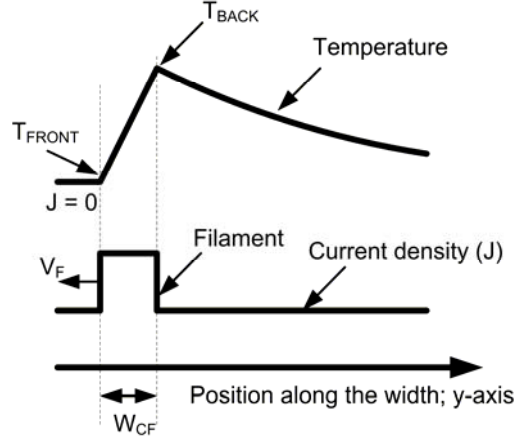


Figure 26 Schematic of temperature profile and current distribution of moving CF.

As long as the higher impact ionization rate exists in the front end of CF, the CF can move toward the colder region. The temperature distribution in CF for a short time is simulated in the relevant to the heat diffusion in the moving plane (xy -plane). The heat diffusion can be neglected if the filament width is larger than the thermal diffusion length $L_{th} = \sqrt{D_T t_F}$, where D_T is the thermal diffusion coefficient for Silicon $\approx 0.9 \text{ cm}^2/\text{s}$ and t_F is characteristic time defined the filament width (W_{CF} , see Figure 26) and filament speed V_{CF} (i.e. $t_F = \frac{W_{CF}}{V_{CF}} = \frac{\approx 20 \mu\text{m}}{0.5 \mu\text{m} / \text{ns}} \approx 40 \text{ ns}$). Then the diffusion length L_{th} is approximate to about $1.89 \mu\text{m}$, the heat diffusion in this case can be neglected and CF can be considered as in the adiabatic system.

Within the adiabatic system the temperature increases with a constant rate in any point inside W_{CF} . In addition, the references [3], [40] mention the V_{CF} is directly proportional to the temperature difference between front end and back end; the V_{CF} increases linearly with respect to the magnitude of current in the device, expressed by the following relation;

$$\frac{dT}{dt} t_F \propto (T_{back} - T_{front}) \propto \frac{I_S V}{W_F c_V}$$

where I_S is the stress current, T_{FRONT} and T_{BACK} are the temperature at filament boundaries and c_V is the volume specific heat in silicon. This relation can be summarized by;

$$V_{CF} \propto (T_{BACK} - T_{FRONT})$$

In [3] the speed V_{CF} was measured in two identical layouts of NPN device at I_S in range of 0.15-0.35 A presented in Figure 27. The range of I_S was restricted by the fact that for $I_S < 0.15 \text{ A}$ the device has not exhibited the NDR in IV characteristic and for $I_S > 0.35 \text{ A}$ the situation became sophisticated due to the occurrence of more filaments number (N). The V_{CF} increases with the increase magnitude of I_S and the total dissipated power that can be expressed by the relation of square root power dependence; [3], [40]

$$V_{CF} \propto \sqrt{P}$$

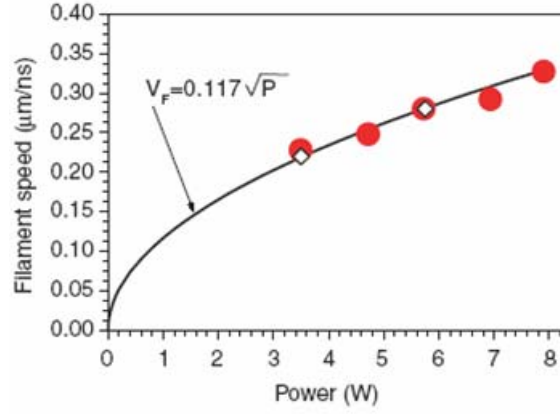


Figure 27 the relation between the power dissipation of CF and its speed for two different devices, and the curve fitting of speed was done by the square root of power. [3], [19]

From [3], the measured voltage $V(t)$ changes within one pulsing period according to the localized CF induces the temperature along the linear device (W_D). The device voltage depends on the position of CF in respect to device features: it is dependent on how the impact ionization rate and temperature in CF depends on the device position. In [3] the $V(t)$ waveform changes in repetitive manner due to the CF behaves similarly from pulse to pulse; therefore, the $V(t)$ can be analogous to the footprint of CF during its motion. The $V(t)$ waveform and the evolution of temperature along device width are presented with together in Figure 28 (a) and (b).

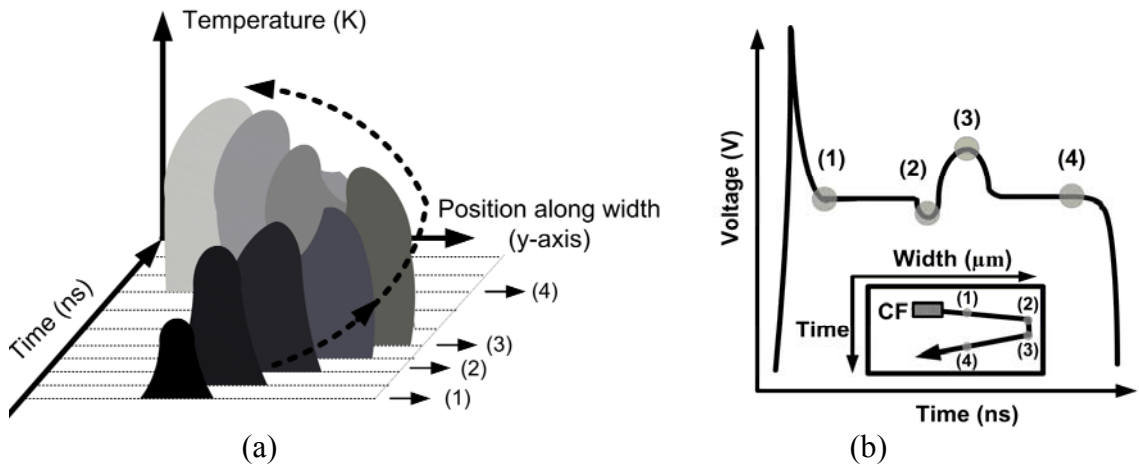


Figure 28 (a) The schematic of temperature distribution (y-axis) induced by moving CF in linear device in time evolution. (b) The $V(t)$ waveform, observed in the previous device technology, is marked at instants (1)-(4) in relevant to (a). The inset demonstrates CF movement by the time-position plot. [3], [19]

The temperature profile at time (1) in Figure 28 (a) is induced by CF that is generated at the middle device. The CF has left its initial position form $t > (1)$ and travels close to the right device end (DE) at time (2). The voltage drop at $t = (2)$ in Figure 28 (b) was observed in the former smart power technology with the dedicated doping at the device end. [3] At

time (3), the CF stands at the right DE inducing the temperature to maximum as the appearance of maximum voltage peak. Higher voltage relates to the fact that the impact ionization rate is low in region with high temperature; as a result, the voltage has to increase for compensating and maintaining the constant current. The inset of Figure 28 (b) illustrates the CF movement in the evolution of space-time.

1.7 Thermal Breakdown

Within the avalanche regime of ESD device such the studied NPN devices in this thesis the avalanche current (I_{AV}) is generated from the collector/base junction during the reverse biasing. The voltage across this pn junction determines the breakdown voltage (V_{BD}). As a consequence of the temperature rise during the avalanche multiplication, the further carriers are thermally generated (I_{TH}) supporting the I_{AV} . The device current after the breakdown event comprises of two components;

$$I = I_{AV} + I_{TH}$$

The avalanche terms dominates the device current in the early stage ($I_{AV} > I_{TH}$). Once the generated holes in base (I_B) are enough for forward bias the emitter/base junction, the NPN device will be activated at the voltage V_{TR} and then the device voltage significantly drops to the holding voltage (V_H), see the S-Shaped IV characteristic in Figure 29. The V_H is determined by the voltage at the emitter/base junction.

By stressing the device with long duration the I_{TH} increases gradually according to the accumulated temperature until it plays a dominant role over the I_{AV} in device current ($I_{TH} > I_{AV}$). So long as the temperature rises, the I_{AV} decreases accordingly with the lower impact ionization rate. At the critical temperature (T_{CRIT}), the I_{AV} will drop to zero as thermal generation current can sustain the injected current ($I_{TH} \gg I_{AV}$). Consequently the voltage at collector/base junction is reduced to the second or thermal breakdown voltage V_{TB} . [41]

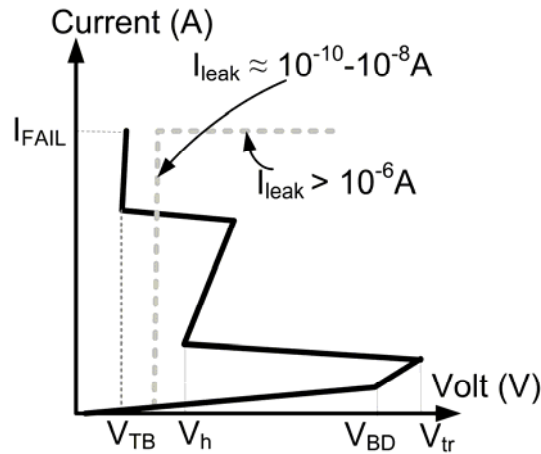


Figure 29 The S-Shape IV characteristic illustrates the breakdown voltage (V_{BD}), the triggered voltage (V_{TR}), and the thermal breakdown voltage (V_{TB}). The device is degraded at I_{FAIL} in the thermal breakdown regime, determined by the leakage current ($I_{LEAK} > 10^{-6} A$).

The criterion of device failure is specified to 10^{-6} A measured by the DC measurement; see the dotted line in Figure 29. The I_{LEAK} has the typical magnitude in range of 10^{-10} - 10^{-8} A for device in the normal operation. The compliance value is limited by $I_{LEAK} < 10^{-6}$ A, and the device will be judged to fail at the failure current (I_{FAIL}) for $I_{LEAK} > 10^{-6}$ A.

1.7.1 Current filament during thermal breakdown event

The induced temperature in device increases until the concentration of thermally generated carriers equals to the back ground doping concentration (n_d) at the critical temperature (T_{CRIT}). The relation between T_{CRIT} and n_d is expressed as followed; [42]

$$n_d = 1.69 \times 10^{19} e^{\left(\frac{-6.377 \times 10^3}{T_{CRIT}}\right)} \cdot \left(\frac{T_C}{300}\right)^{\frac{3}{2}} \quad [\text{eq-1}]$$

where n_d is the background doping concentration per cubic centimeter in the volume with the maximum heat dissipation. In [43], T_{CRIT} varies in range of temperature about 400 °K (for $n_d \approx 10^{13}/\text{cm}^3$) to 1000 °K (for $n_d \approx 10^{18}/\text{cm}^3$) that can approach to the melting point of Silicon ($T_{MELT} \approx 1688 \text{ K} = 1415 \text{ °C}$). In long pulse duration, the localizing CF introduces T_{CRIT} to the location, where the local resistance becomes low. The current is allowed to flow more through the junction at this region with T_{CRIT} [44]. The current becomes immobilizing and is attracted to the highly heated region with high conductance. In [45], the local heating by CF in bipolar device during TB event was optically presented by using the 2D Holographic Interferometry technique. [38] Not only are the bipolar devices observed, but the diodes are also found the TB event. This thermal breakdown mechanism can eventually destroy the ESD PD devices.

The mechanism of TB mentioned previously in [46] depends on many important factors such the device geometries, the doping concentration, the complex filamentary modes and the ambient temperature, etc. Therefore, the TB event induced by CF in various structures of NPN devices was further investigated and discussed in this thesis.

Chapter 2

Investigation techniques

The failure analysis (FA) in semiconductor industry can be classified into the passive technique and the active technique. For the passive techniques, the signal (the energy information) is retrieved from the electrical measurements such as the laser voltage probe technique. In the active techniques, a probe is contacted directly with the DUT, and either an external detector or the device itself will be used as detector such as the optical beam induced current.

Since the semiconductor device responses to the ESD stress by releasing the thermal energy, many investigation techniques have been developed on the basis of temperature measurement by utilizing of the interaction between light and temperature. Light is performed as the non-contact probe because it can access to varieties of investigated fields. For instance, the Infrared Thermography is one of thermal imaging techniques that make use of the black body radiation. The radiated light is emitted from a semiconductor device. [47] The black-body radiation will be shifted in wavelength to a shorter wavelength with temperature increase. The emitted light depends on the emissivity of that materials fabricated in ICs, and the temperature can be estimated by monitoring the radiation from the device substrate.

Another example of FA technique works on the principle of Fluorescent Microthermal Imaging (FMI) technique for hot spot localization in semiconductor device [48], based on Europium-III-Thenoyotrifluoroacetate Trihydrate (EuTTA). This material generates the fluorescence light in the visible wavelength of 612 nm when it is exposed to UV light. The quantum efficiency decreases with the increasing temperature. The sample device is coated with the special thin film. Then the temperature is determined by the imaging intensity of the visible fluorescence light of coating film. The light is separated from the excitation light in UV. The temperature mapping is calculated from the comparing images during operation and non-operation.

In addition, the FA technique bases on FMI concept is Scanning Reflectance Thermometry yielding the surface temperature of device [49]. This method is based on the change in reflectance of the surface with respect to the temperature variation under stressing. However this technique is limited to some circuits without passivation layer. [49] This limitation can be resolved by the Optical Interferometry technique. The Optical Interferometry method is a measurement technique exploiting the temperature-induced displacement of the surface or the interference of light beam probing inside device [50]-[52]. The surface displacement is accurately measurable. This displacement provides the thermal expansion information at a position of the light beam. The interference of probe beam and reference beam produces the Interferogram of the heated area or the thermal expansion of surface, yielding the information of heated spot along the lateral device. In silicon material, the Infrared probe beam penetrates through a wafer and the multiple

reflections at the substrate surface can happen. The reflected intensity can be evaluated from the substrate temperature, so called “Fabry-Perot Thermometry” [50]-[51]. This method is applied for observing the wafer temperature during the device operation. Nevertheless the difference of temperature whether it increases and decreases cannot be simply distinguished.

In BCD technology, it has been known that the high current density during ESD event can cause the destruction by CF activities [53]-[56]. Many authors experimentally studied the CF behavior and its thermal effect. For instance, current filaments (CFs) in ESD protection devices are studied by measuring the recombination radiation [57], and CFs were investigated in thin-film SOS diode using stroboscopic absorption measurement [58]. In this work, the variation in the temperature or the carrier density is changeable with the refractive index change (Δn) in silicon substrate. This variation can be detected from the “thermo-optical effect” and the “plasma-optical effect”, which is distinguished by the time-resolved measurements. The phase change contributes the information of induced temperature change by CF that is interpreted with voltage waveform as followed topics.

2.1 Electrical Investigation by the Transmission Line Pulsing (TLP) system

The S-shaped IV characteristic can manifest the electrical properties of ESD devices such as the presence of localized CFs and the thermal breakdown events. The IV curve represents the averaged voltage over the selected window as a function of increasing current. The ESD PD device responds differently to the dissimilar pulse shape and dissipated power in device. To designate the testing standard, the different shapes of ESD pulse are restricted to the pulse rise time ($t_r \approx 0.5 - 10$ ns) or the pulse duration ($\tau \approx 10 - 100$ ns), in which the TLP system is comfortable to reproduce the identical pulses and to adjust the pulse shapes [59].

The IV characteristic in Figure 30 was measured in the NPN device presenting the breakdown voltage (V_{BD}), the snapback voltage (or the triggered voltage: V_{TR}), and the holding voltage (V_H). The DC measurement was measured at each increment of I_S until the leakage current reaches the compliance at $I_{LEAK} \geq 10^{-6}$ A, which determines the failure current (I_{FAIL}).

The electrical schematic of TLP setup is simplified by Figure 31. A transmission line cable has the characteristic impedance of 50Ω and the wide frequency range of up to 2 GHz. This transmission cable can be loaded up to very high voltage. The high voltage in cable is discharged through the Device Under Test (DUT) via a series resistance i.e. $1 \text{ k}\Omega$ (see R_{TLP} in Figure 31). A matching resistance of 50Ω is connected in parallel with the DUT for a reflection with the impedance in transmission cable. The 50Ω matching impedance can divert a part of total current limiting the maximum stress current.

The pulse width ($\tau \approx 100$ ns to $1 \mu\text{s}$) is adjustable by changing the length of transmission cable. For instance, the 10 meters length cable provides the pulse duration (τ) of 100 ns. The relation of pulse duration and cable length can be expressed by; [59]

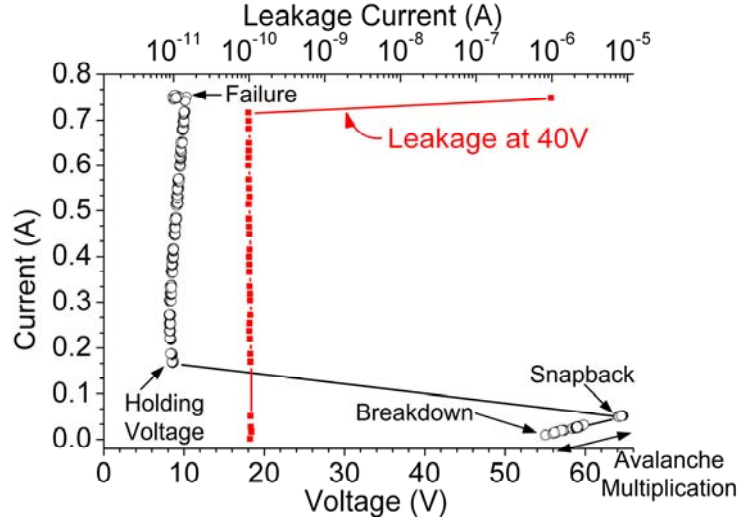


Figure 30 Current-Voltage (IV) characteristic of NPN device is plotted with leakage current (I_{LEAK}). It shows the snapback of voltage to holding voltage. The failure threshold was determined from the leakage measurement ($I_{LEAK} \geq 10^{-6}$ A).

$$\text{Pulse duration } \tau = \frac{2 \times \text{Length}_{\text{tran-cable}}}{V(\text{propagation speed})} \quad [\text{eq-2}]$$

where $\text{Length}_{\text{tran-cable}}$ is length of the transmission cable multiplied by factor of two due to the wave propagates back and forth. V is the propagation speed of wave in transmission cable (≈ 0.2 m/ns). The pulse rise time (t_r) can be varied from the standard value at 0.5 ns by adding R-L elements between the termination of cable and the TLP resistor (R_{TLP}). The measured transient voltage and current of DUT are given as an example in Figure 33 (a).

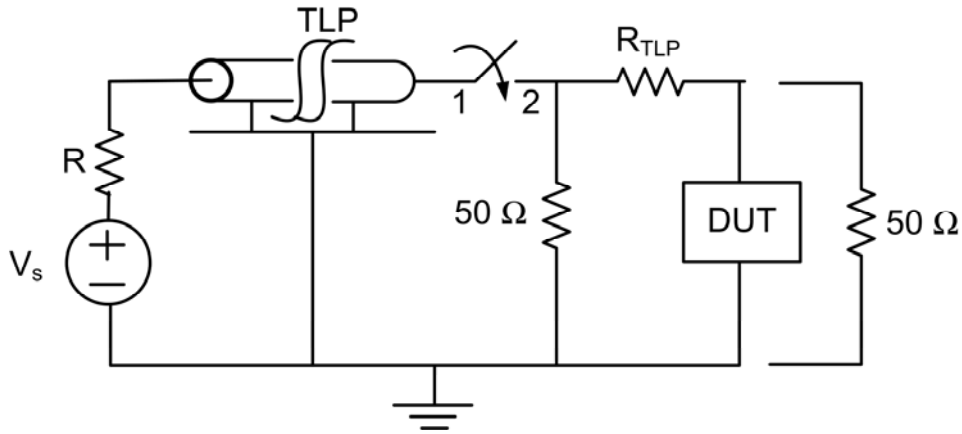


Figure 31 The equivalent circuit schematic of Transmission Line Pulsing with 50 Ω system [$R = 20$ MΩ, $R_{TLP} = 1$ kΩ, $R_{\text{coaxial}} = 50$ Ω]. [59]

The incident voltage waveform (V_{inc}) from the transmission line cable with the characteristic impedance (Z_0) of 50 Ohms enters the discontinuity point A (see Figure 32). For the next medium with impedance (Z), the presence of impedance discontinuity or

mismatch impedance can change the amplitude of signal or shift the phase of sinusoidal wave. The reflected voltage (V_{ref}) can be determined by the relation:

$$V_{ref} = + \left(\frac{Z - Z_0}{Z + Z_0} \right) V_{inc} \quad [\text{eq-3}]$$

where Z_0 is the characteristic impedance of the transmission cable, and Z is the total impedance [$50\Omega // (50 + R_{TLP})$].

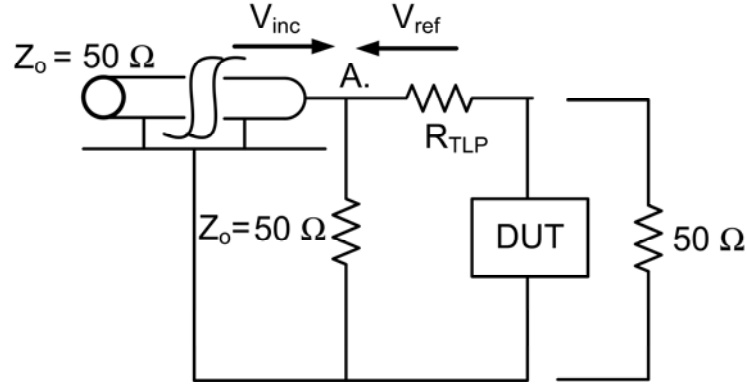


Figure 32 The circuit schematic of the termination shows the reflection point A. [59]

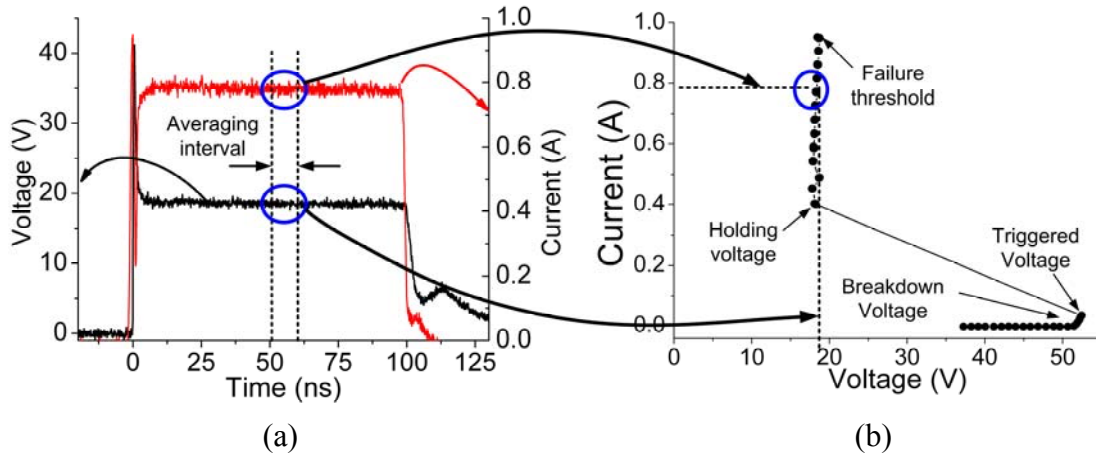


Figure 33 (a) The example of voltage and current waveforms are measured in NPN device under stressing with pulse with rise time (t_r) of about 1 ns and duration (τ) of 100 ns. (b) IV characteristic is averaged over the selected window marked with two dotted lines in (a) Each data point is averaged from 10 voltage waveforms.

The voltage amplitude is averaged over the selected window of each waveform for reducing the effect of voltage oscillation within a single stress. And each data in IV characteristic of Figure 33 (b) has been averaged over several different waveforms at a constant I_S . After stressing at each current step, the leakage current (I_{LEAK}) is periodically checked by the DC measurement in the dark, in order to avoid the emitting of extra carriers in the light sensitive device. Two primary evolutions of I_{LEAK} are monitored and simplified by Figure 34 (a) and (b) and named with two terminologies as followed;

“Soft failure” is defined by the marginally increase in the I_{LEAK} that develops below the compliance at 1 μA . The low range of I_{LEAK} probably relates to the charge trapping in the gate oxide or the melt silicon.

“Hard failure” is specified by the I_{LEAK} reach the failure threshold at 1 μA . This mechanism could be relevant to the highly induced temperature that melts the metal contacts to penetrate the device junction.

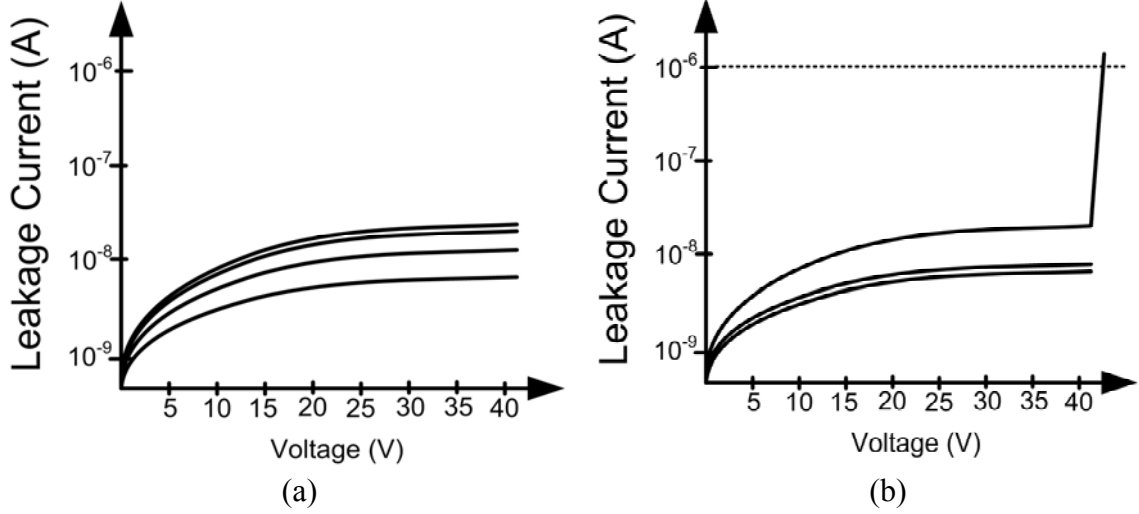


Figure 34 (a) The development of leakage currents (I_{LEAK}) by the DC measurement with the reversed bias from 5-40 V with voltage increment of 5 V ($V_{BD} = 54$ V) shows the slightly increasing currents as I_S increases (soft failure). (b) I_{LEAK} reaches suddenly the compliance of 1 μA determining the device degradation (hard failure).

2.2 Transient Interferometric Mapping Techniques

To understand the CF dynamic and the electrical response of ESD PD, the measurement based on the optical technique has been developed, allowing visualizing the localized current filament and the heat dissipating in device [60]-[61]. The thermal energy mapping method using holographic interferometric technique [38] enables us to image the hot spot due to self heating effect of current filament and the heat distribution during destructive event, in which the temperature rises occurs in short time scale (100 ns or shorter) [1], [62].

The investigation of CF behaviors in this study has a working principle based on the Transient Interferometric Mapping (TIM) technique. The DUT is illuminated and focused from the device backside by a laser beam with wavelength (λ) of about 1.3 μm that is not absorbed in Silicon substrate. This method measures the changing of the refractive index (n) induced by the temperature change [63]-[64] and by the carrier concentration change. [65]-[66] The principle of TIM technique is simplified with the schematic in Figure 35.

The laser beam is initially split into “the reference beam” and “the probe beam”. The probe beam passes through the substrate from device backside and then it reflects back from the metallization layer near the topside of device. In the device with highly dissipated power, the induced temperature causes a change in the refractive index (Δn) of the probe beam.

Simultaneously, the reference beam propagates to reflect on the reference mirror. Afterwards the reflected probe beam interferes with the reference beam and results in the interference signal at the photo detector. The phase shift represents the change in the spatial information in time evolution caused by the electrical stress. The detected phase change ($\Delta\phi$) can be expressed by the following relation; [67]-[68]

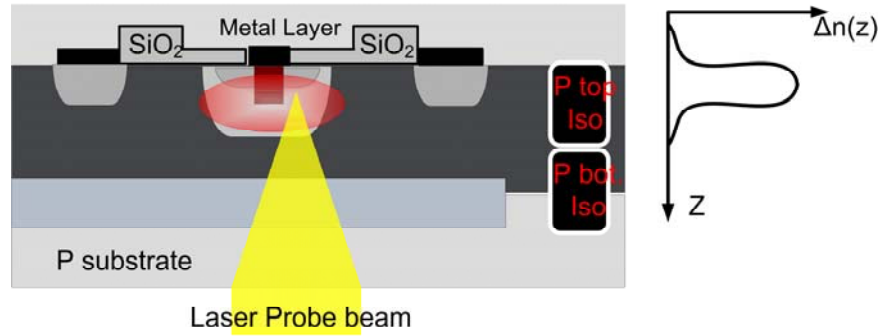


Figure 35 The principle of Transient Interferometric Mapping (TIM) technique exploits the change of refractive index (n) of focusing Laser beam at the locally heated area. The extracted phase provides the information of temperature change. [38]

$$\Delta\phi = 2\frac{2\pi}{\lambda} \int_0^l \Delta n(x, y, z, t) dz \quad [\text{eq-4}]$$

where λ is the free space wavelength of laser beam, l is the thickness of bulk substrate, and $\Delta n(x, y, z, t)$ is the change of refractive index (n) at the electrical stressing compared with non stress. It is derivable from the relation of $\Delta n(x, y, z, t) = n(x, y, z, t) - n_o(x, y, z, t)$. The factor of two in equation [eq-4] is a consequence of the twice passing of probe beam in forward and backward directions through the Silicon substrate. The total refractive index comprises of two significant terms including the thermal term (Δn_{th}) and the free carrier term (Δn_{fc}); [68]

$$\Delta n(x, y, z, t) = \Delta n_{th}(x, y, z, t) + \Delta n_{fc}(x, y, z, t) \quad [\text{eq-5}]$$

The term of Δn_{th} is the thermally induced change of refractive index. It has the positive value expressed by;

$$\Delta n_{th}(x, y, z, t) = \frac{dn}{dT} \Delta T(x, y, z, t) \quad [\text{eq-6}]$$

In equation [eq-6], the thermal optical coefficient of silicon $\left(\frac{dn}{dT}\right)$ is about $1.9 \times 10^{-4} \text{ K}^{-1}$ for light beam with λ of $1.3 \text{ } \mu\text{m}$ [69]. The term of Δn_{fc} in equation [eq-5] is relevant to the change of refractive index induced by free carrier. It has the negative value that composes of the change of electrons and holes concentration;

$$\Delta n_{fc}(x, y, z, t) = \Delta n_{electrons}(x, y, z, t) + \Delta n_{holes}(x, y, z, t) \quad [\text{eq-7}]$$

From equations [eq-4]-[eq-6], the evolution of phase shift is calculated by the integral of thermal change (ΔT) and carrier densities change ($\Delta N_{electrons}$ and ΔN_{holes}) along the optical beam that is expressed by the followed relation; [67]-[68]

$$\Delta \varphi(t) = 2 \cdot \frac{2\pi}{\lambda} \cdot \int_0^L \left(\frac{\partial n}{\partial T} \cdot \Delta T(z, t) + \frac{\partial n}{\partial N_{electrons}} \cdot \Delta n_e(z, t) + \frac{\partial n}{\partial N_{holes}} \cdot \Delta n_{holes}(z, t) \right) dz \quad [\text{eq-8}]$$

The derivative terms of $\frac{\partial n}{\partial T}$ is the induced temperature coefficient. $\frac{\partial n}{\partial N_{electrons}}$ and $\frac{\partial n}{\partial N_{holes}}$ are the plasma coefficients of the refractive index in silicon for electrons and holes. And L determines the thickness of Silicon substrate. [68]

2.2.1 The extracted phase change due to induced temperature

The different sign distinguishes the effects between the temperature change and the free carrier contribution in equation [eq-5]. The positive phase ($\Delta \varphi_{th}(x, y, t)$) relates to the change of refractive index induced temperature change, but the negative phase ($\Delta \varphi_{fc}(x, y, t)$) is changed by the change of carrier density as followed; [67]

$$\Delta \varphi(x, y, t) = \Delta \varphi_{th}(x, y, t) + \Delta \varphi_{fc}(x, y, t) \quad [\text{eq-9}]$$

$\Delta \varphi_{fc}(x, y, t)$ with negative sign can be negligible, if the high power is significantly dissipated in the DUT, and the change of carrier concentration is much faster process than the responsive time of temperature change. The sample situation that $\Delta \varphi_{fc}(x, y, t)$ is neglected is during the device power is turned off immediately, the highly induced temperature during operation still remains at a high degree at time $t \gg \tau$. The phase shift $\Delta \varphi(x, y, t)$ is considerably proportional to the two dimensional energy density (E_{2D}) expressed by; [68], [70]

$$E_{2D}(x, y, t) = \frac{\lambda c_v}{4\pi} \frac{1}{\frac{dn}{dT}} \Delta \varphi(x, y, t) \quad [\text{eq-10}]$$

where the light wavelength $\lambda = 1.3 \times 10^{-6}$ m, the volume specific heat $c_v = 1631 \times 10^{-6}$ $\left[\frac{J}{Kg \cdot K} \right]$. Consequently the energy density in equation [eq-10] can be simplified as;

$$E_{2D}(x, y, t) \approx 0.88 \times \Delta\phi(x, y, t) \left[\frac{nJ}{\mu m^{-2}} \right] \quad [\text{eq-11}]$$

The thermally induced phase shift describes not only the instantaneous power information but also the history of power dissipation in the device. The measured phase offers the information of dynamic changes in the heat dissipation. In addition, the instantaneous power dissipation density (P_{2D}) is calculated from the derivative of phase shift by the followed relation; [71]

$$P_{2D}(x, y, t) = \frac{\lambda}{4\pi} \frac{dn}{dT} \left\{ c_v \frac{\partial \Delta\phi(x, y, t)}{\partial t} - k \left[\frac{\partial^2 \Delta\phi(x, y, t)}{\partial x^2} + \frac{\partial^2 \Delta\phi(x, y, t)}{\partial y^2} \right] \right\} + j_{th,z}(x, y, z=0, t) \quad [\text{eq-12}]$$

where k is the temperature independent heat conductivity, and $j_{th,z}(x, y, 0, t)$ is the normal component of the heat flow density vector at the top surface representing the thermal power transferred from bulk to the top layer, which is negligible.

2.2.2 Scanning Heterodyne Interferometer

To achieve a better resolution in space and time evolution, the scanning heterodyne interferometer is a technique for determine quantitatively the thermal energy and free carrier concentration [68], which also provides a means to observe the thermal degradation. To obtain the information of phase change at each scanning position, the automatic movable stage allows scanning with precise movement along the active region in x- and y- directions or the arbitrary path.

The simplified schematic presented with Figure 36 begins with the laser beam with wavelength (λ) of 1.3 μm generated from the laser diode. (A silicon device is transparent to $\lambda > 1.1 \mu m$.) The laser beam is split up into two frequency beams by the Acoustic Optic Modulator (AOM). A zero order beam with frequency ω_0 remains the same frequency and then it will be blocked by the beam stopper. The first order beams of other two frequencies are slightly shifted to frequency ω_1 and ω_2 driven by the AOM. Then these two diffracted beams have functions as the probe beam and the reference beam for a planar investigation. One of the diffracted beams (LB2) is deviated from the optical axis by mirror1 prior to entering the microscope objective. This beam subsequently reflects back on mirror2 to the AOM, functioning as the reference beam LB2. On the optical axis the probe beam (LB1) is focused by the Infrared microscope objective lens on the interesting area. The probe beam (LB1) reflects on the metal layer at topside of DUT. Then LB1 interferes with the reference beam (LB2) at the photo detector labeled with the solid line in Figure 36. It is important to

note that the length of the reference branch and the length of the probe branch should be balanced within the coherence length of the laser light. The measured output signal from a fast digital oscilloscope is the heterodyne beat signal expressed by relation; [72]-[73]

$$s(t) = s_{ref}(t) + s_p(t) + s_{dis}(t) + 2\sqrt{s_{ref}(t)s_p(t)} \cdot \cos(2\Delta\omega t + \Delta\phi(t)) \quad [\text{eq-13}]$$

The beating frequency $2\Delta\omega$ represents the twice passages (back and forth) of laser through the substrate with the frequency shift $\Delta\omega = 2\omega_1$. The phase change ($\Delta\phi$) is due to the temperature change at the position of focusing beam. The three terms of dependent signals s_{ref} , s_p , and s_{dis} are the reference beam, probe beam and the disturbance signal respectively.

During the experiment, the investigated chip is glued with PCB and connected to the electrical pad with Au wire bonding. The chip on PCB is mounted on the movable stage in xy -plane with precision of $0.1 \mu\text{m}$ controlled by stepping motor. At each scanning position, the device is stressed by multiple identical pulses for improving the signal to noise ratio ($\frac{S}{N}$). All electrical instruments and the moving stage are automatically synchronized by the computer. And, the phase shift is extracted from the heterodyne signal by the principle of Fast-Fourier Transform [72]-[73].

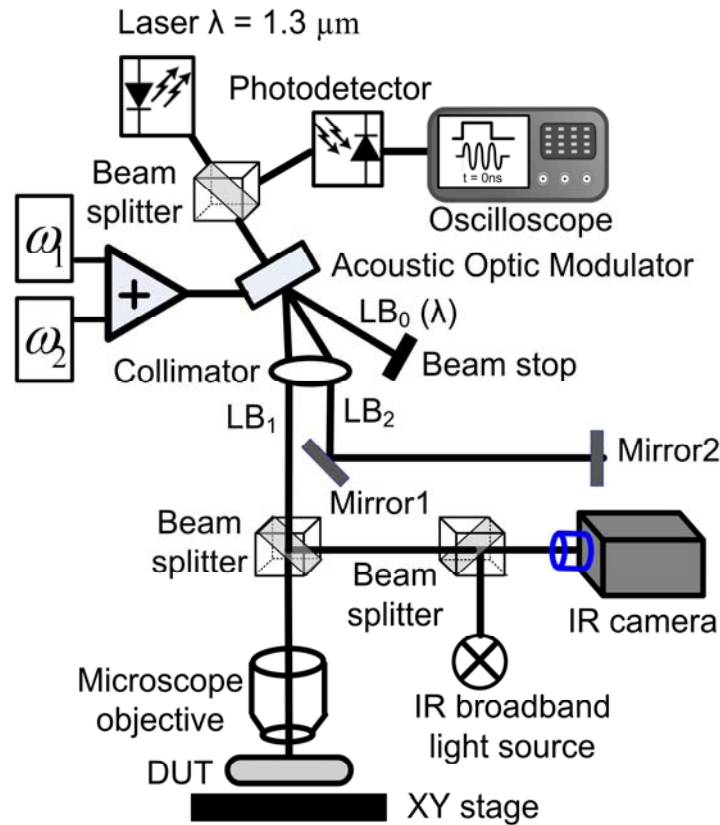


Figure 36 Schematic of the scanning heterodyne interferometry set-up consists of main components including laser diode, photo detector, beam splitters, Infrared camera, Acoustic Optic Modulator (AOM), frequency generator(ω_1 and ω_2), microscope objective lens, and DUT on the movable stage in xy -plane. [2], [72]-[73]

In the configuration of "slow" Heterodyne Scanning Interferometry, the beating frequency is defined by the different frequency between two beams $2\Delta\omega = 2(\omega_1 - \omega_2)$. For slow heterodyne scanning schematic in Figure 36, the diffracted beam is modulated with two frequencies (ω_1, ω_2); the parameters of scanning heterodyne setup are summarized in Table 2. In case of the "fast" heterodyne scanning set-up the beam is modulated with single frequency (ω). The beating frequency of fast heterodyne setup is then calculated from $2\Delta\omega = 2(\omega)$. The light beam in heterodyne scanning setup with wavelength (λ) of $1.3 \mu\text{m}$ will not introduce the extra free carriers in all studied devices for this thesis. This method is considered as the non-invasive investigation method that allows us to stress the DUT with plenty of repetitive pulses.

Configuration	
Beating frequency ($2\Delta\omega$)	2-10 MHz
Detector Bandwidth	28 MHz
Time resolution	15 ns
Phase sensitivity	16 mrad
Signal to Noise Ratio	~ 60

Table 2 Parameters of the Scanning Heterodyne Interferometric set-up. [72]-[73]

To interpret the phase with the heterodyne scanning technique, the identical pulse and the stability in device dynamic are required; otherwise, the data analysis could deviate in high degree from the actual characteristic. The more numbers of stress pulses can narrow the distribution of quantitative phase from pulse to pulse, but the trade-off is introducing of device degradation before completing one scanning path.

2.2.3 Dual Beam Michelson Interferometer

The Dual Beam Michelson Interferometer is built for measure the absolute phase shift from dual beams with the resolution of 0.4 ns. Two laser beams are probed simultaneously at two different positions for sensing the temperature change in time. This technique can provide the information of the dynamic change in device under stress such as the CF speed, which cannot achieve by single probe beam method.

The schematic in Figure 37 presents two laser diodes of wavelength (λ) $1.3 \mu\text{m}$, which are orthogonally polarized to each other. To have the orthogonal polarization the $\frac{\lambda}{2}$ attenuator plates are installed with cube polarizer. These two beams are combined afterwards by the polarizing beam splitter (PBS). Two probe beams are focused on the DUT by the microscope objective lens. The DUT is installed on the manually rotated stage in X-, Y-, and Z- directions. Each laser branch (LB1 and LB2) is split into the reference and probe beams by the beam splitter (Beam splitter1 and 2 respectively). Two reference beams individually reflect on the Mirror1 and Mirror2. These two mirrors are mounted on the stage

with the Piezoelectric control that enables to adjust the signal to have the maximum sensitivity. The probe beam of LB1 is fixed on the optical axis, but the probe beam of LB2 is adjustable by Mirror3. This adjustable mirror allows correcting the distance between two probe beams. To visualize the position of two focusing beams, the broadband Infrared light source provides the visibility of device layout with two lasers on the Infrared camera. [74]

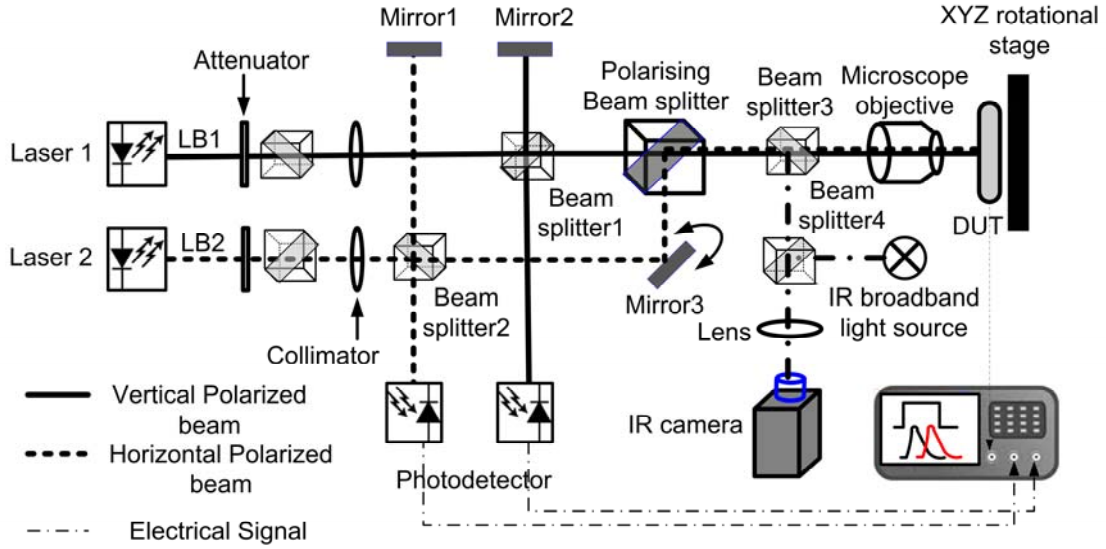


Figure 37 Schematic set-up diagram of the dual beam Michelson Interferometry comprising two laser diodes, two photo detectors, a microscope objective lens, beam splitters, an Infrared camera, and DUT on the movable stage in xy -plane. [74]

Table 3 is the summary of important parameters of the dual beam interferometer setup. Two magnifications ($20\times$ and $50\times$) of microscope objective are chosen that are suitable for visualizing the different dimensions of all studied devices (i.e. linear NPN device widths $W_D = 100\text{-}400\text{ }\mu\text{m}$). In most experiments the objective $50\times$ was suitably used for W_D of $100\text{-}200\text{ }\mu\text{m}$, the beam spot has the diameter $2.3\text{ }\mu\text{m}$ determining the spatial resolution for this setup. One important parameter is the distance between two probe beams that is restricted by the objective magnification; see the light schematic in Figure 38 (a). The distance between two probe beams (S_{2BEAMS}) should not exceed $110\text{ }\mu\text{m}$ in case of using the objective with magnification $50\times$. The time resolution of this set-up involves with the responsive time of detector that is about 0.4 ns for a detector bandwidth of 1 GHz .

Since the electrical stress is applied to the DUT, the refractive indexes of two laser probes (n) unequally change with respect to temperature change at two locations. The sinusoidal signals from two detectors are detected and recorded by the fast digital oscilloscope (4 GHz). The phases are directly calculated from the measured signal according to the followed relation; [75]

The measured signal;
$$S = \frac{AC}{2} \sin(\Delta\phi) \quad [\text{eq-14}]$$

The absolute phase

$$\Delta\varphi = \arcsin\left(2 \cdot \frac{S}{AC}\right) \approx 2 \cdot \frac{S}{AC} \quad [\text{eq-15}]$$

The measured sinusoidal wave (S) in Figure 38 (b) has the linear relationship with the absolute phase change ($\Delta\varphi$), where AC is the peak to peak of sinusoidal magnitude. This relation is valid for small phase ($\Delta\varphi \leq \frac{\pi}{2}$) and the working point has to locate at the middle regime of phase amplitude. [75]-[76] For the repeated measured signal, several pulses should be measured for averaging the results in order to improve the signal to noise ratio $\left(\frac{S}{N}\right)$.

Objective	20×	50×
Field of View	520 × 390 μm	210 × 160 μm
Pixel size	0.6806 μm	0.2768 μm
Beam diameter	6.1 μm	2.3 μm
Distance between two lasers	110 μm	34 μm

Table 3 Parameters of the dual beam Michelson Interferometry for two magnifications. [75]

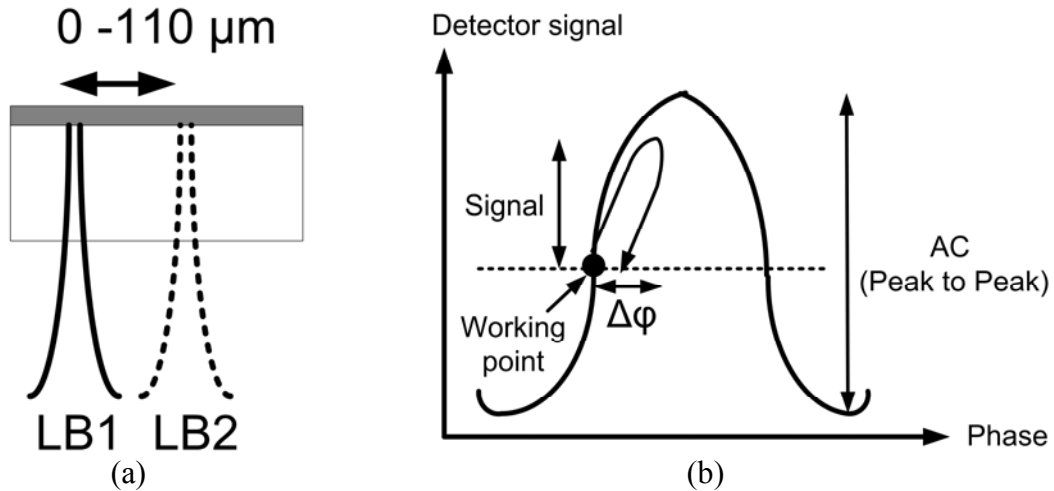


Figure 38 (a) Distance between two focused probe beams (110μm) depends on the magnification of objective lens (50×) (b) The detected signal shows working point in the middle of the sinusoidal waveform for $\Delta\varphi < \frac{\pi}{2}$ [rad]. [75]-[76]

2.2.4 2D Holographic Transient Interferometric Mapping

The two dimensional interferometer based on the holographic microscopy provides the information of spatial temperature distribution in xy -plane of ESD device. This inspecting technique exploits the short pulse to illuminate the backside of DUT that is suitable for the unrepeatable device characteristics that varies from pulse to pulse. [77] This measurement technique is flexible to perform the thermal imaging at one time instant or two time instants within a single stress.

2.2.4.1 2D TIM at single time instant measurement

The two dimensional TIM (2D TIM) setup is illustrated by Figure 39; the schematic depicts the light path incorporated with the electrical instruments. The laser beam, generated from the Nd-YAG pulser having wavelength of 1300 nm, illuminates on the device backside and penetrates through Silicon substrate without absorption (The λ of 1250 nm practically offers a superb quality of Interferometric fringes) The laser beam is partially separated to incident on the photo detector before entering the part of Interferometer setup, in order to point out the illuminating instant and synchronize with the device stressing.

Once the beam has entered the Interferometer part, it is split by the non polarizing beam splitter into two beams including the probe beam and the reference beam. On the probe beam branch, the diffracted beam passes through the device backside to reflect on the topside of DUT during ESD stressing. Simultaneously the reference beam goes reflecting on the adjustable mirror. The optical distances between the probe branch and reference branch have to be equivalent within the laser coherence length for creating the interference pattern at the Infrared camera. [75]

The light schematic in Figure 40 demonstrates the diffracted probe beam passes through the lens (Lens1) on the optical axis and is collimated by the microscope objective for focalizing on the DUT. The beam diameter is adjustable in range of 100 μm - 5 mm, which determines the field of view as a set-up parameter. The probe beam and the reference beam eventually pass through the optical lens (Lens2) to interfere at the Infrared camera. The Infrared Image of DUT can transform to project on the plane of camera, and the DUT position is adjustable. To adjust the fringes orientation and the width of fringes, the angle of reference mirror can be rotated. The schematic of IR light is labeled by the dotted lines. [75]

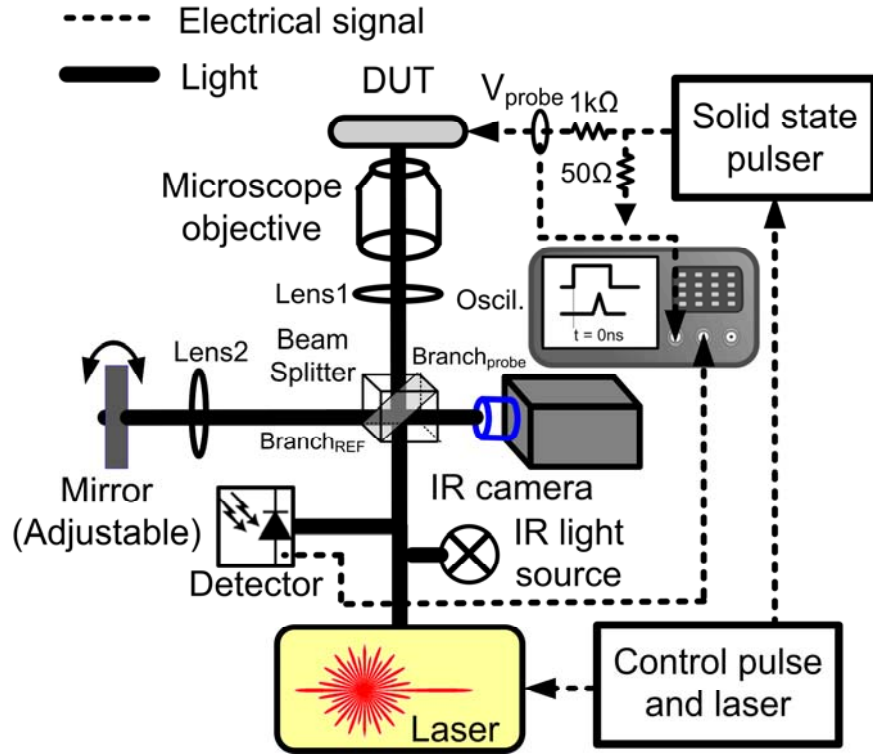


Figure 39 Schematic of 2D TIM setup for measurement at single time instant. [38], [75], [78]

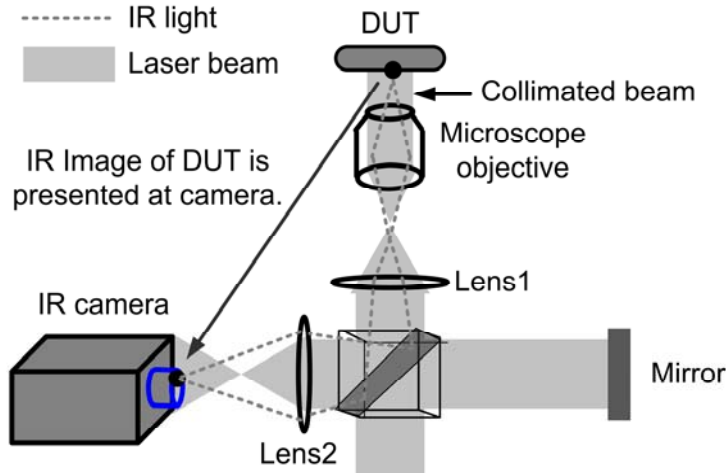


Figure 40 Schematic of laser beam and IR light in the Michelson Interferometer.

2.2.4.2 2D TIM at two time instant measurement

One 2D phase image might be insufficient to present the induced temperature change or the complex CF behaviors. But the 2D TIM at two time instant measurement offers two 2D phase images within a single stress, in which the information of temperature evolution at two interesting instants can be obtained.

The additional laser is incorporated with the conventional set-up of 2D TIM at one time instant, see Figure 41. The polarized direction of the added beam must be perpendicular to the polarized direction of the formal beam. At the beginning of setup, these orthogonal beams are combined with the polarizing beam splitter (splitter1). These beams are partially split to the photo detector by a beam splitter to indicate the illuminating instants on the digital oscilloscope. The delay time between two imaging instants and the time to stress are synchronized that are adjustable by the computer. The Interferograms of the reference image and the stressed image should be recorded immediately after one other to reduce the optical system instability e.g. the vibration on optical table.

These two orthogonal beams enter the Michelson Interferometry setup at two consecutive times that are split up into the probe beam branch and the reference beam branch. In sequence of two orthogonal beams function likewise as discussed in the one time instant measurement of 2D TIM. Two orthogonal probe beams conveying the phase shift information interfere consecutively with two orthogonal reference beams. Two orthogonal beams are collimated with lens2, and split by the polarizing beam splitter2 to enter individually two Infrared cameras. [79]

The laser diameter illuminated on DUT is in range of 100-500 μm determined by the magnification of microscope objective lens; see the parameters of 2D TIM technique in Table 4. The time resolution of 2D TIM setup is determined by the specification of laser pulser. The resolution of laser is limited by the illuminating time on the DUT corresponding to the exposing time of Interferogram on the Infrared camera. The entire backside of DUT is captured in the pixel format, and the minimum pixel size is calculated by the magnification of lens. The distance between two light sources should be greater than the limit of light diffraction (d_{diffract}) for optimizing the fringe pattern contrast expressed by the Reyleigh's criterion as followed;

$$d_{\text{diffract}} = \frac{1.22\lambda}{2N_A} \quad [\text{eq-16}]$$

The resolution of laser1 (Opolette laser) is about 5.3 ns and the resolution of laser2 (Vibrant laser) is 3.4 ns. The spatial resolution depends on the pixel of Interferogram image and the diffraction of the optical system. [75]

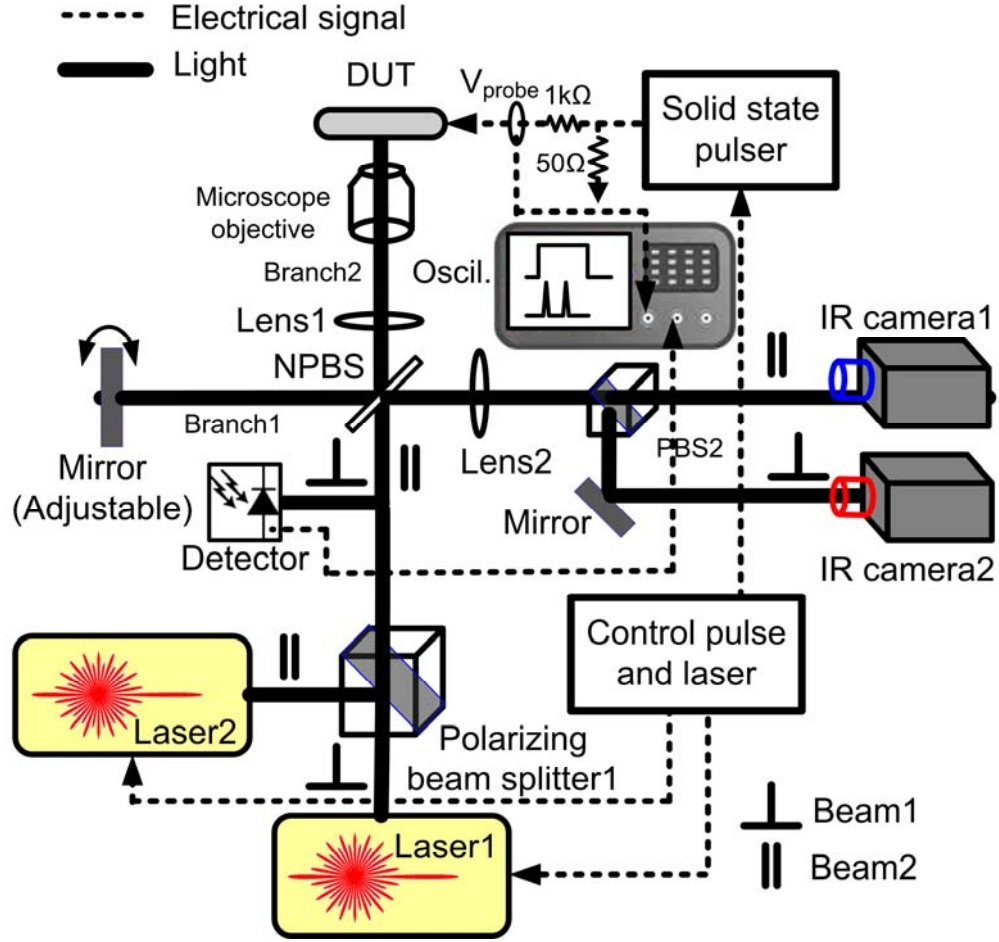


Figure 41 Schematic of 2D TIM measurement at two time instants. The delay time between two consecutive shots is controllable and synchronized with the electrical stressing on DUT. [75], [79]

Objective	10×	20×	50×
Maximum Field of view (μm)	1500 × 1000	850 × 500	430 × 230
Pixel size (μm)	1 × 0.9	0.6 × 0.5	0.3 × 0.3
Numerical Aperture (N_A)	0.26	0.4	0.42
d_{diffract}	3	2	1.9

Table 4 Setup parameters for lens with two different magnifications of the 2-dimensional Holographic Interferometer. [75]

The parameters of stress pulse including the pulse amplitude I_s , the pulse duration (τ), number of stress pulses and the delay time of laser τ_{delay} are adjusted by the in-house software. The DUT is stressed with by the ESD pulses generated from the DMOS pulser. High voltage is converted to the current pulse by a high series resistance (i.e 1 k Ω) to the DUT.

The change in Interferogram of stressed image is extracted by subtraction the stressed device image from the non-stressing image (or the reference image) done by the Fast Fourier Transform method programmed in MATLAB. The fringe pattern is expressed by the following relation:

$$I(x, y) = A(x, y) + B(x, y) \cdot \cos[k \cdot r + \phi(x, y)]$$

where $A(x, y)$ is the background signal in space xy -plane, $B(x, y)$ is the amplitude of the fringes, k is the wave vector of the laser beam, r is the vector in space, and $\phi(x, y)$ is the total phase shift induced from the electrical stress. [75]

In the heterodyne scanning TIM technique, the device has to be stressed with plenty of stress pulse so long as the scanning completes the inspected region. This method is considered as a time consumption measurement and not suitable for the non-repetitive device characteristics. The 2D holographic TIM technique presents the phase images, which the information of temperature change in 2D can be achieved at once, but the temperature evolution cannot be obtained with this method.

Since each setup has the trade-off, the investigator should select an appropriate optical technique to suit with the different characteristic of ESD device.

Chapter 3

Experimental Results

3.1 Investigated Devices

The listed devices in Table 5 were experimentally investigated and discussed in all thesis content. In fact, not only these devices had been analyzed. Other device structures, such devices with inclined doping of emitter edge or with the modified doping concentration, were also preliminarily characterized. Nevertheless, the measurement results are not presented here according to the limited time to investigate them in details.

The layouts of investigated device will be presented and discussed in each sub-chapter of experiment results.

Name	Device Type	Structure	Description	Discussed in
NPN_Std	NPN	Linear (Standard)	Devices have four different widths including 100, 200, 300, and 400 μm .	Figure. 42
NPN_Heat	NPN with the side heater	Linear	Heater (size $30 \times 30 \mu\text{m}$) is located at 60 μm away from a device end of NPN (NPN_Std) device.	Figure. 101 (d)
NPN_Dope	NPN with highly doping P-Body in middle	Linear	NPN (NPN_Std) devices have solid doping of P-Body in the middle for the deterministic starting CF position. The device widths are 200, 400, and 600 μm .	Figure. 45
NPN_Round	NPN	Circular	P ⁺ Diffusion locates at the center, enclosed collinearly with the round Emitter and the outermost N ⁺ Sink layers ($R_{\text{Emitter}} = 17 \mu\text{m}$)	Figure. 60
NPN_Meander2	NPN	Meander 2 Fingers	The N ⁺ Emitter/P ⁺ Diffusion are nonparallel with N ⁺ Sink. (Ohmic length (L) changes.)	Figure. 64 (a) and Figure. 65 (a)
NPN_Meander3	NPN	Meander 3 Fingers	Device has the similar doping profile to the NPN Meader2.	Figure. 64 (b)
NPN_Oval	NPN	Oval	N ⁺ Sink has a stripe structure and locates close to one side of oval coupling regions of N ⁺ Emitter and P ⁺ Diffusion.	Figure. 68 (f) And Figure 69 (a)

Table 5 List of investigated bipolar transistor devices with different layout, doping concentration, and shapes. The cross sections of listed devices are displayed and discussed in each sub-chapter guided in the last column.

3.2 Current Filament study

As the device dimension has been scaled down, the ESD devices in Table 5 were fabricated by the recent fabrication technology of smart power device. Figure 42 demonstrates the ESD NPN device layout that was mainly tested with ESD pulses for CF behavior observation; the location of CF was marked with the dashed oval in the schematic.

The CF, observed in devices of Table 5, did not behave repetitively and could not be determined its behavior beforehand due to the current instability from pulse to pulse. The heat dissipation in DUT contributed by CF depends on the magnitude of current (I_S); the temperature in CF highly depends on power. CF was observed that it behaves differently as the I_S increases. However there are some common features at a fixed I_S .

Many experiments of the CF study were done in the NPN device of Figure 42, and to group CF behaviors two regimes of current I_S are taken into account as followed;

- 1) $I_S < 0.41\text{-}0.45$ A, the single CF (1CF) is generated at random starting positions found likewise in all structure types.
- 2) $I_S \geq 0.41\text{-}0.45$ A, there was a small probability of multiple current filament (CFs) compared to single CF. Modes of multiple CFs have the increasing trend as the magnitude of I_S increases.

The IV characteristic consists of multiple current filamentary branches, in which each branch represents the number of CF (N). At the interval of current $I_S = 0.45\text{-}0.8$ A, N is alternately 1 or 2 from pulse to pulse [80], which the experimental study will be discussed further in this chapter. Not only was the alteration of N observed with change of I_S , but the degree of current instability, the induced temperature by CF(s), and the thermal breakdown event also depend strongly on the magnitude of I_S . Behavior of single or multiple CFs are investigated by the optical TIM methods and correlated to the IV waveforms. Each activity of localized CF relates to the voltage change and contributes the certain power dissipation into the ESD device. Randomness of current instability, traveling speed, standing time on initial CF position, time consumption on DE, the CF size, and interaction of multiple CFs have been experimentally investigated with varied measurement techniques for comparison as discussed in following sub-topics.

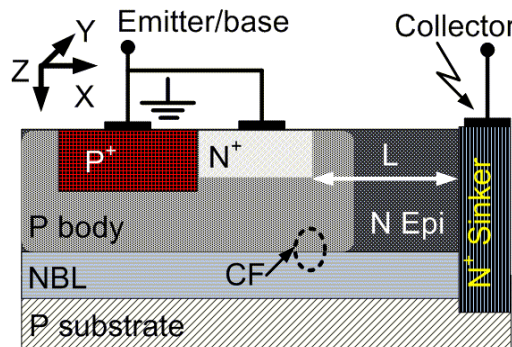


Figure 42 The cross section of NPN_{Std} device that was mainly investigated and marked the CF location with the dotted oval. The N⁺Buried Layer (collector) was applied positive voltage pulses via N⁺Sink and the N⁺Emitter/P⁺Diffusion were shorted to ground. The distance between N⁺Sink and N⁺Emitter determines the Ohmic length (L).

3.2.1 Randomness in triggering position of Current Filament

The repetitive and therefore deterministic triggering position of CF has been found in the previous study of [3], [70]. Nevertheless, all bipolar devices in Table 5 exhibits the random initial CF position at low current in range of $I_S < 0.45$ A, furthermore the heading direction was accordingly nondeterministic.

Figure 43, the voltage peak (V_{PEAK}) indicates the temperature increases at the moment of CF turnabout the DE. The time intervals of t_{PEAK1A} and t_{PEAK1B} in Figure 43 (a) consists of the standing time of CF at triggering position (t_{STAND} , discussed in next topic) and the time consumption of CF on moving from its triggering position to the DE. The shift in the 1st maximum V_{PEAK} of waveforms A and B determines the triggering CF instability at random position ($t_{PEAK1A} \neq t_{PEAK1B}$). The time between two maximums V_{PEAK} ($t_{PEAK1-2}$) is the traveling time across the device width.

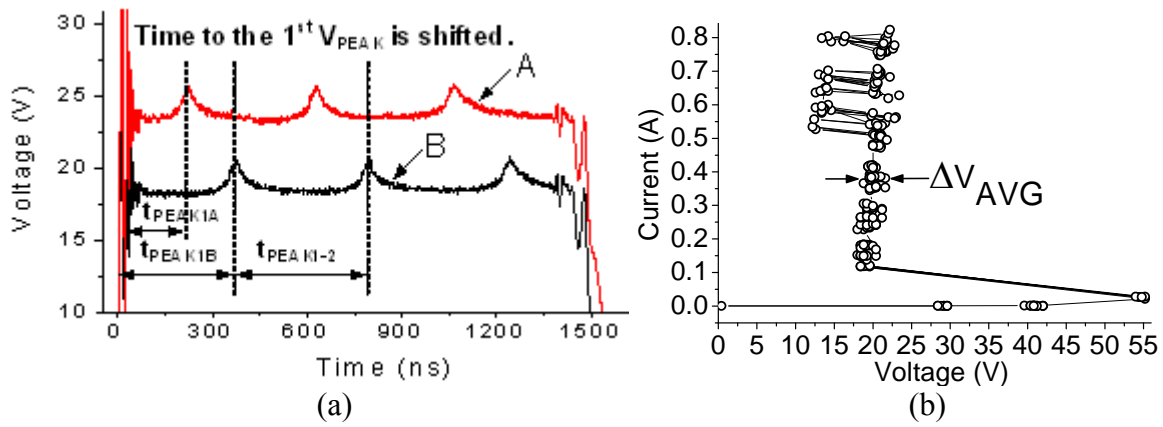


Figure 43 (a) Overflow plots of $V(t)$ waveforms A and B demonstrates the shifting of V_{PEAK} at $I_S = 0.3$ A (b) The data scattering has been observed along IV characteristic.

Since the unpredictable CF due to current instability brings some difficulties to determine the failure criteria, the study of randomness would be beneficial for understanding how the random degree of initial CF position changes as a function of stress current I_S . The random triggering of CF leads to the shift of V_{PEAK} ; therefore the small deviation in voltage along IV curve in Figure 43 (b) (ΔV_{AVG}) was the result of selecting the averaged window over the randomly shifted V_{PEAK} and V_H . The IV characteristic could not explicitly demonstrate how the triggering CF position distributes along width at each current step.

Therefore, to study the effect of current I_S to the CF randomness, the NPN_Std device (the device layout in Figure 42) was stressed with 100 TLP-pulses at three current steps including $I_S = 0.256$ A, 0.41 A, and 0.45 A. The duration of stress pulse (τ) was set to 500 ns that was long enough for CF traveling from the 1st DE to 2nd DE as the presence of the 1st and 2nd V_{PEAK} .

Each voltage waveform was searched for two maximum V_{PEAK} done by using the programmed software in MATLAB. Instants of the two maximum peaks were recorded in time evolution and statistically plotted as a function of three currents ($I_S = 0.256$, 0.41, and 0.45), see Figure 44.

Each column demonstrates two scattering zones of maximum peaks (V_{PEAK1} and V_{PEAK2}) in time. Time to the 1st peak at $I_S = 0.256$ A distributed widely more than at $I_S = 0.41$ and 0.45 A, indicating CF at the lowest I_S has the high degree of current instability, and the randomness decreases with the increase of I_S magnitude. This means the triggering position of CF becomes more deterministic with increasing of I_S . In addition, the CF would turnaround the closest DE solely at $I_S = 0.256$ A, but it preferred to turnaround the far DE at higher I_S . Therefore the averaged times to the 1st V_{PEAK} had extended to about $\frac{t_{TURN}}{2}$ at $I_S \geq 0.45$ A. (t_{TURN} is the traveling time of CF to complete one round trip.) This statistical experiment demonstrates the distribution degree of initial CF position depending on the I_S magnitude; however, it could have been effected by the distributed resistance at the device contacts as observed in references [73].

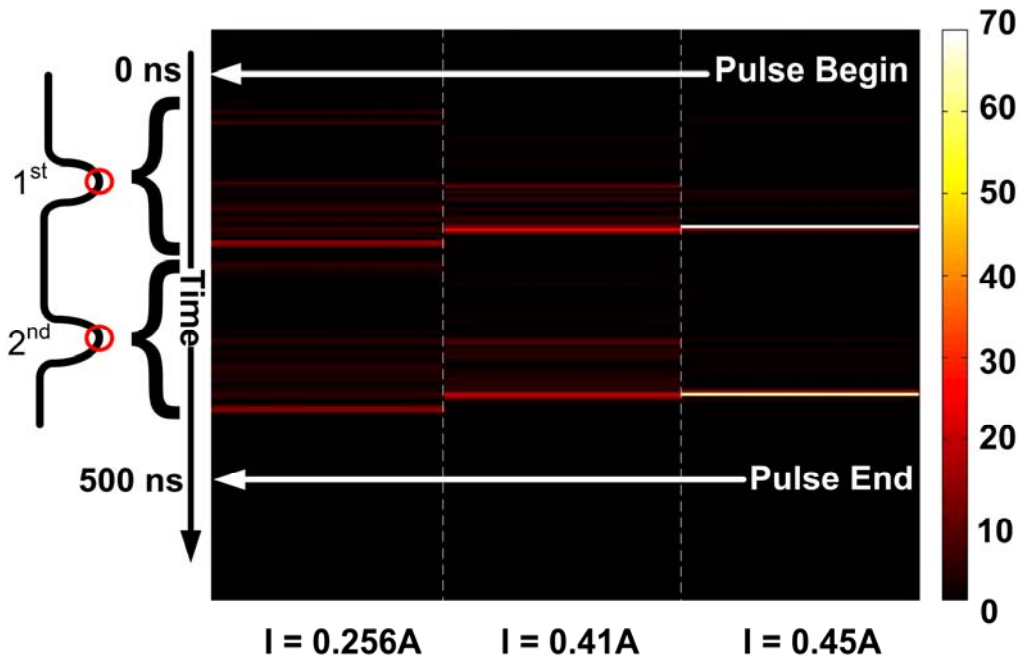


Figure 44 The 200 μm NPN_Std device was observed the random distribution of initial CF position under stressing with multiple pulses at three current steps (Pulse duration = 500 ns). Each voltage waveform was recorded two instants of two maximum peaks and plotted as a function of time.

3.2.2 Initial time before traveling

In references [3] , [81], the simulation of temperature distribution induced by CF shows CF spends a certain time on standing ($t_{STAND} \approx 30$ ns) at its triggering position before localizing. In order to measure the t_{STAND} , it was impossible with all discussed techniques in chapter 2 due to the randomness of starting position in this device technology.

To measure the time t_{STAND} , the linear NPN device (NPN_Dope) with the high doping concentration in center of P-body width of transistor device was suitable for this investigation because it has a low base resistance (R_B) that attracts current to flow through, see the layout in Figure 45. The large solid doping of P-body region is sandwiched between

the plug arrays of P-body doping. With this doping pattern the repetitive initial position of CF can be fixed at the device center; therefore, it was possible to measure the time t_{STAND} with our optical TIM setup.

To estimate the t_{STAND} of triggered CF, the temperature distribution or phase shift ($\Delta\phi$) in time, measured by the Heterodyne Scanning TIM technique, was extracted during the early period before the phase envelope will laterally shift. The scattered plots in Figure 46 (a) and (b) are the plots of the temperature evolution ($\Delta\phi$) and the power distribution (P_{2D}) during CF standing at initial location. (Each plot has time step of 5 ns and the resolution of heterodyne scanning setup is 3 ns)

The envelope of induced temperature has gradually risen and then the envelope of P_{2D} began shifting toward a direction after a certain time passed. The time of rising phase equals to the time of CF standing at its initial position (t_{STAND}) that was required for raising the temperature gradient inside CF until it could initial to move from $t \geq 30$ ns. The t_{STAND} of about 30-35 ns were consistent with the results in [3].

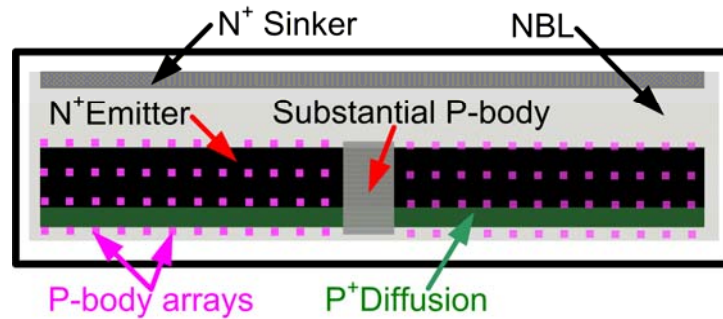


Figure 45 The layout of *NPN_Dope* device is nearly similar to *NPN_Std* device except the substantial P-body doping at center that is sandwiched between P-body plug arrays. This structure was dedicated for fixing the starting CF position at the middle.

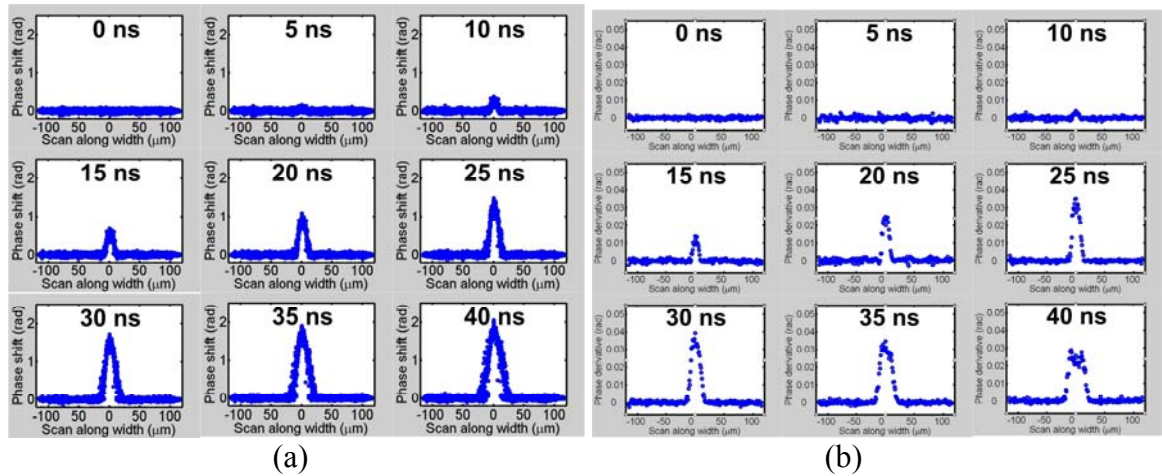


Figure 46 The scattered plots of (a) Phase distribution and (b) Power (P_{2D}), investigated in the *NPN_Dope* device with repetitive triggering CF position, show the standing time of CF (t_{STAND}) \approx 30-35 ns at $I_s = 0.6$ A.

3.2.3 Size of Current Filament

To estimate the filament size (W_{CF}), the 2D TIM technique at one time instant was utilized to capture the size of hot spot induced by standing CF. There was necessary to capture at ahead of time during CF standing ($t < t_{STAND}$) before localizing or before heat diffusion for achieving the closest approximation. The heat region in 2D phase image at the imaging time about 30 ns is suitable for approximating size of CF.

The size W_{CF} was calculated by taking the ratio between numbers of pixels and the actual dimension (in μm -scale). Figure 47 (a) and (b), captured from backside of the NPN_Std device, show the hot spot induced by CF at currents $I_S = 0.6$ and 0.9 A respectively. Size of W_{CF} at $I_S = 0.6$ A was approximately $20 \mu\text{m}$ and enlarged to about $28 \mu\text{m}$ at $I_S = 0.9$ A.

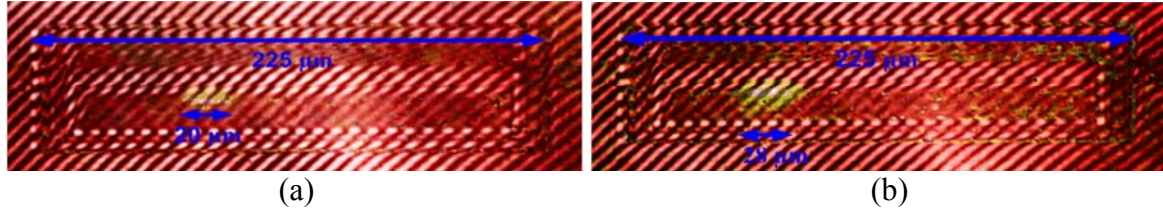


Figure 47 The 2D phase images of $200 \mu\text{m}$ NPN_Std were captured at the early imaging instant of 30 ns and overlaid on the Interferogram image showing the CF size of about $20\text{--}30 \mu\text{m}$ at (a) $I_S = 0.6 \text{ A}$ (b) $I_S = 0.9 \text{ A}$.

To diminish the effect of heat diffusion or any imprecise estimation from 2D phase images, the Dual Beams Interferometer technique having two probe beams with small diameter of $2.3 \mu\text{m}$ was used that provides the smaller discrepancy in W_{CF} measurement. The obtained signal from photo detector of this setup yields the linear response to the temperature change within CF wall. The phase evolution will sharply increase when the front-wall of W_{CF} enters the position focusing beam at time t_1 , and the phase increases continuously until the back-wall of W_{CF} leaves the probe beam at time t_2 , see the illustration in Figure 48.

The probe beam diameter is much smaller than the W_{CF} , the period of rising phase between t_1 and t_2 (DP: or in the interval $[t_1, t_2]$) was measured for determination of W_{CF} using the known traveling speed V_{CF} (discussed in the next topic).

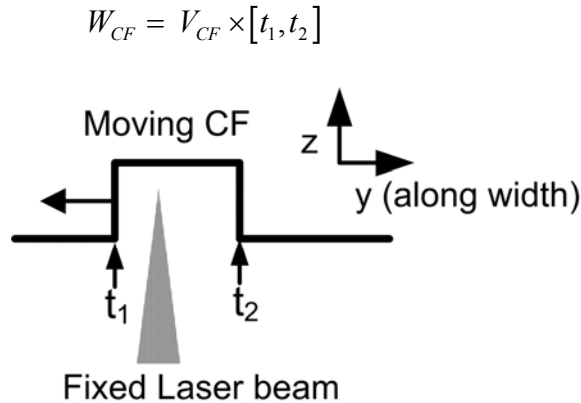


Figure 48 The simplified schematic of CF moving past the focusing laser beam.

The temperature profiles at a position of focusing beam induced by traveling CF were plotted with $V(t)$ waveforms shown in Figure 49 (a) and (b). The 2nd rising phase in Figure 49 (a) means CF came back to the position of focusing beam within one pulse duration. Once the averaged filament speed V_{CF} has value about 0.51 $\mu\text{m}/\text{ns}$ at I_S in range of 0.45-0.8 A, the W_{CF} can be computed as followed;

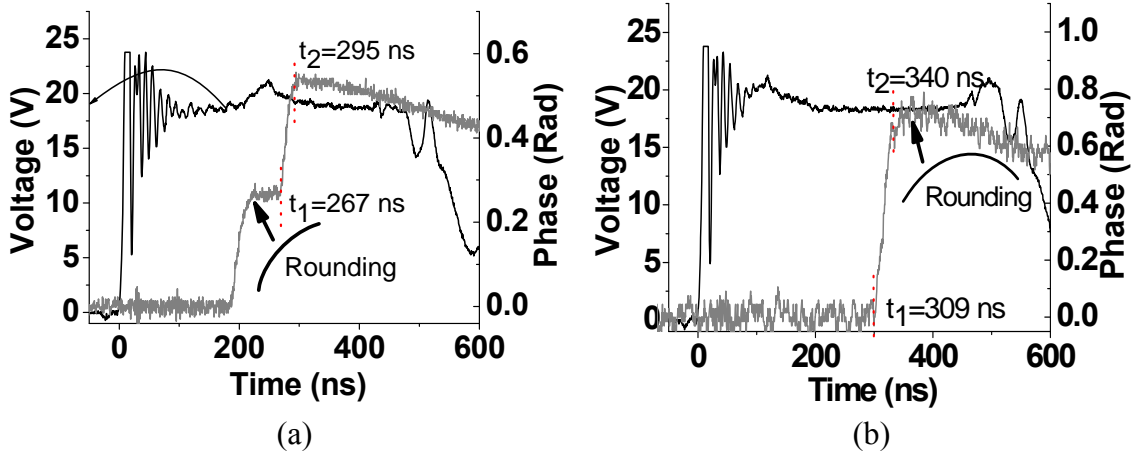


Figure 49 (a) and (b) Transient phases, investigated by a beam of the Dual beam Michelson Interferometry setup, were plotted with $V(t)$ for calculating the CF size.

The CF size of phase in Figure 49 (a) $W_{CF} = V_{CF} \times (t_2 - t_1) = 0.51 \times 28 \approx 14.3 \mu\text{m}$

The CF size of phase in Figure 49 (b) $W_{CF} = V_{CF} \times (t_2 - t_1) = 0.51 \times 31 \approx 15.8 \mu\text{m}$

By approximating V_{CF} to be constant for this stressing current, the averaged W_{CF} at I_S of 0.45-0.8 A has value of about 14-16 μm . The W_{CF} , computed from V_{CF} and time of CF passing by laser beam $[t_1, t_2]$, was reasonable and approximately accorded with the measured W_{CF} by 2D phase images.

In conclusion, at a low applied current I_S the CF has a small size, and has a larger size at higher I_S . In fact the photo detector has a fast response to the temperature change, and the recorded phase should increase and decrease rapidly with respect to the fast moving CF. However the 1st rising phase of Figure 49 (a) (marked with curve) increased slowly and its increasing period $[t_1, t_2]$ should not be taken into account of W_{CF} calculation. Even though the laser probe was fixed at a same place during stressing period, the measured phase could have different slopes between the 1st and 2nd rising phases. This non linear response was probably caused by the effect of detected signal far from the working point. (To have a linear response, the working point should be at the middle of sinusoidal waveform, see the explanation in Figure 38 (b)).

3.2.4 Speed of Single CF

The CF movement depends on the temperature effect combining with the decreasing impact ionization rate [8]. The experiment and simulation have been previously done to observe the moving CF speed in linear structure of ESD PD devices. In [81], two motions of CF were distinguished; one was a transfer from a cell to a next one and another was motion

along the diffusion region. The driving force for CF movement is the temperature gradient within the CF. [3], [40] In [3], [70], the filament speed V_{CF} has been found to increase with the increase current I_S , the experiment showed how far CF could travel for a longer distance at higher I_S compared to that at lower current I_S .

Here the traveling speed of CF had been investigated as a function of current I_S in various device shapes. The filament speed V_{CF} could be estimated from the voltage alteration and be calculated more precise from the 2D phase images or the phase evolution from the Dual beams Michelson Interferometry technique.

3.2.4.1 Filament speed at room temperature by the electrical measurement

The simplest way to measure the speed V_{CF} was done by measuring the time to the 1st V_{PEAK} . The NPN_Dope device with 200 μm W_D (the layout is shown in Figure 45) having the repetitive triggering CF position at the middle was investigated the V_{CF} at increasing currents. In a linear ESD device, V_{PEAK} as a landmark in time indicates CF spends time on traveling from center W_D to DE.

The experiment was done at room temperature and the voltage waveforms were measured at currents I_S including 0.2, 0.3, 0.4 and 0.5 A, see the overflow plot of waveforms A to D in Figure 50. The time to the 1st V_{PEAK} was shortened ($t_1 > t_2 > t_3 > t_4$) with respect to the increase current meaning a higher power CF reasonably moved with a faster speed. About half W_D was the travel distance of $\approx 100 \mu\text{m}$ for the V_{CF} calculation as the followed relation;

$$V_{CF} = \frac{\text{moving distance}}{t} = \frac{\text{half of width}(\approx 100\mu\text{m})}{t - t_{STAND}} \quad [\text{eq-17}]$$

where t_{STAND} is about 30 ns. The calculated CF speeds of waveforms A-D were including 0.44, 0.47, 0.52, and 0.57 $\mu\text{m}/\text{ns}$ with respect to the shortened traveling time t_1 - t_4 . This estimation might not be the precise method; however it offers us the convenience and the tendency of speed at this I_S regime. If more numbers of waveforms would have been averaged, a better accuracy could have been achieved with this estimation.

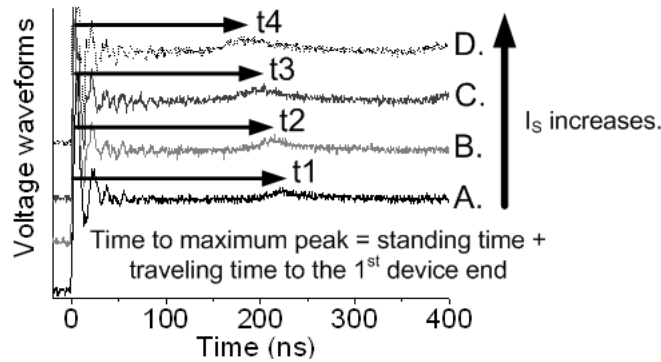


Figure 50 CF was specified to be triggered at the middle of NPN_Dope device. Time to maximum V_{PEAK} was shortened gradually from waveform A to D. ($t_1 > t_2 > t_3 > t_4$) Then the moving speed of CF (V_{CF}) increases linearly with the increase of I_S .

To improve the accuracy in V_{CF} estimation, the time to 1st V_{PEAK} of 10 voltage waveforms at five currents I_S are averaged out and plotted as a function of increase current presented in Figure 51. Between low current to intermediate current ($I_S = 0.2$ A- 0.6 A), single CF will travel with the averaged speed $\langle V_{CF} \rangle$ in range of 0.42-0.63 $\mu\text{m}/\text{ns}$ at room temperature. Although the speed done by averaging offers the improved accuracy, the Dual Beams Michelson Interferometry technique can provide the better precision in V_{CF} value by stressing device at once as discussed further.

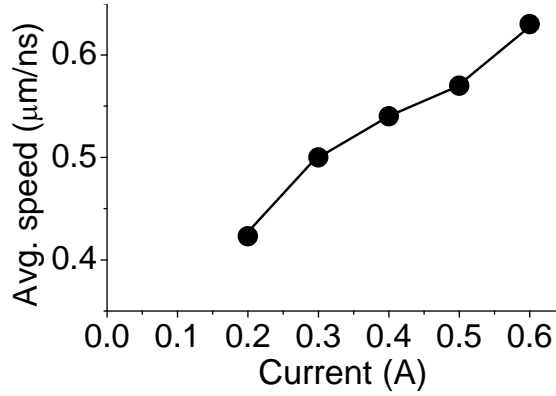


Figure 51 The CF speeds $\langle V_{CF} \rangle$ in the NPN_Dope device, measured from time to the 1st V_{PEAK} as discussed in Figure 50, are averaged over 10 voltage waveforms at currents in range of 0.4-0.6 $\mu\text{m}/\text{ns}$.

3.2.4.2 Filament speed at room temperature by Dual beams Michelson Interferometry

In Dual Beams Michelson Interferometry setup, two focusing beams are exploited for sensing the induced temperature change when CF passes by. The traveling time between dual beams (Δt) was measured, in which the distance between two beams (S_{2BEAMS}) was known and controlled manually.

The example of investigation in Figure 52 (a) shows the distance S_{2BEAMS} was 85 μm and one beam (Laser2) was focused close to the bottom DE. The moving schematic that was derived from transient phases and voltage is illustrated by Figure 52 (b). Time between two 1st rising phases in Figure 52 (c) ($\Delta t = t_2 - t_1$) responses to the visiting moment of CF at two locations of dual beams in consecutive time.

With this technique, the speed V_{CF} can be simply calculated from one stressing as below;

$$\text{Filament speed } (V_{CF}) = \frac{\text{distance between two beams } (S_{2BEAMS})}{\Delta t} = \frac{85}{150} \approx 0.56 \mu\text{m} / \text{ns}$$

In addition, the CF reached the bottom DE at the time about $t_2 + \frac{20 \mu\text{m}}{0.56 \mu\text{m} / \text{ns}} = 286 \text{ ns}$ by

estimating from the distance between Laser2 and DE (20 μm) and V_{CF} of 0.56 $\mu\text{m}/\text{ns}$, which is consistent with the time to maximum V_{PEAK} ($t_{PEAK1} = 290 \text{ ns}$) in voltage of Figure 52 (c).

The V_{CF} measurement done by the Dual beams Interferometer presents a close value to the averaged speed in the statistic result of Figure 51.

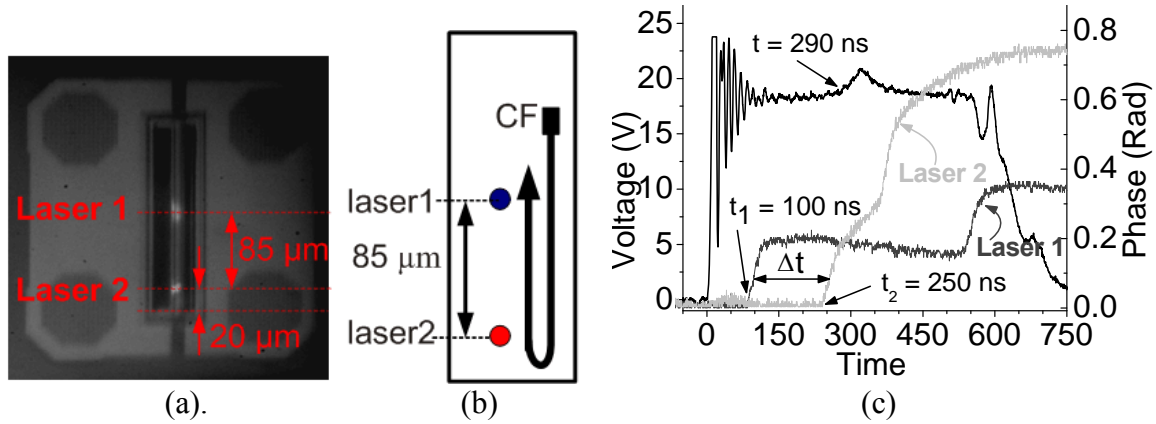


Figure 52 (a) Infrared image of 200 μm NPN from backside (b) CF movement and beams locations are illustrated by this schematic. (c) Phases of Dual beams Interferometry is plotted with transient voltage at $I_S = 0.45 \text{ A}$ from DMOS pulser.

By focusing the two laser beams on the edge of diffusion region, one probably questions whether the light beam interferes the triggering position and the travel speed or not. To observe how the speed V_{CF} deviated from pulse to pulse, the one of beams was shifted to focus at DE and the distance between two beams was narrowed to 51 μm as shown in Figure 53 (a). In the schematic of Figure 53 (b), the CF motion, derived from phases and voltage of Figure 53 (c), presents CF triggered from the bottom DE and then it passed by dual beams at t_1 and t_2 . Time to travel the distance between two beams ($\Delta t = t_2 - t_1$) was 90 ns. Then the filament speed is equal to;

$$\text{Filament speed } (V_{CF}) = \frac{\text{distance between two beams } (S_{2BEAMS})}{\Delta t} = \frac{51}{90} \approx 0.57 \mu\text{m} / \text{ns}$$

Even though the two probe beams were adjusted to focus close together, the calculated V_{CF} did not apparently change. In schematics (b) of Figure 52 and Figure 53 the triggering position of CF was random; therefore one can conclude that the focusing dual beams did not interfere the triggering instability and the V_{CF} of CF in this device technology.

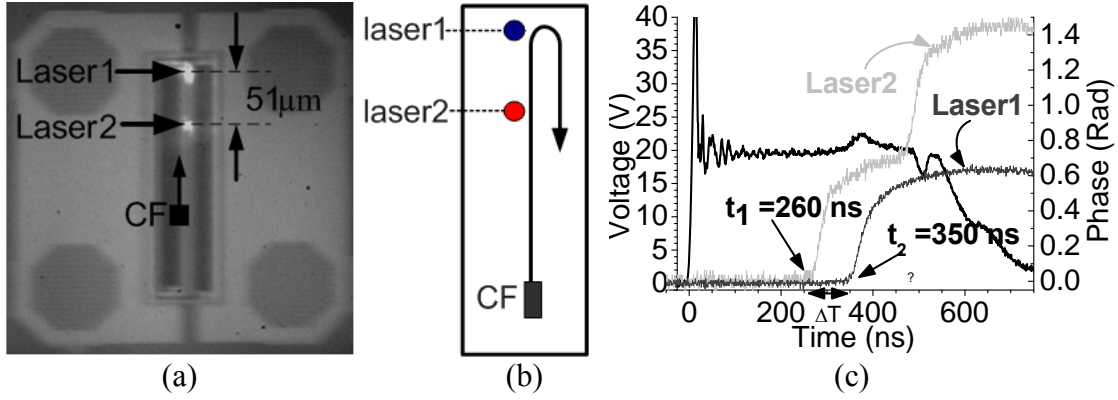


Figure 53 (a) Infrared image of 200 μm NPN_Std device from backside. (b) Starting CF position, moving direction and beam locations are illustrated. (c) Phases of the Dual beams Michelson Interferometry are plotted with voltage, measured at $I_S = 0.45$ A.

3.2.4.3 Filament speed at room temperature by Heterodyne Scanning Interferometry technique

The laser beam was proved not to interfere the CF characteristic during the electrical stressing. Therefore the statistic of V_{CF} observing at positions along CF passage (along W_D) could be achieved by the Heterodyne Scanning TIM technique, too. The 200 μm NPN_Std device in Figure 42 was applied with several ESD pulses per scanning position, and the obtained phase presented the instability of CF from pulse to pulse. With the long pulse duration ($\tau > 500$ ns for $W_D = 200$ μm), a random CF could return to the focusing beam at the 2nd time after turnabout DE.

The twice times of rising phase at consecutive times t_1 and t_2 were induced by the same CF making a roundtrip distance $2\Delta X$, see the phase evolutions in Figure 54 (b). The roundtrip time $[t_1, t_2]$ includes the time consumption on DE (t_{DE}), discussed further in the next topic. The statistic of V_{CF} was calculated from the phase evolution at each scanning position by measuring the roundtrip times $[t_1, t_2]$ of distances between scanning point and DE ($2\Delta X$).

Figure 54 (a) demonstrates the time of one-way travel from scanning point to DE ($\Delta t = \frac{t_2 - t_1 - t_{DE}}{2}$) as a function of distance (ΔX). It demonstrates the symmetrical plot at the middle

W_D ($\Delta X = 100$ μm).

Then the filament speed V_{CF} can be expressed by;

$$V_{CF} = \frac{\text{distance of round trip between the scanning point and DE}}{2\Delta t}$$

$$= \frac{2\Delta X}{t_2 - t_1 - t_{DE}}$$

where the t_{DE} has a constant value of about 30 ns. Phase evolution 1 and 2 in Figure 54 (b) were measured at distances $\Delta X_1 \approx 100 \mu\text{m}$ (at the middle of W_D) and $\Delta X_2 \approx 177 \mu\text{m}$ (at left DE), see the corresponding schematics in Figure 54 (c) and (d).

$$\text{The speed of Phase 1; } V_{CF1} = \frac{2\Delta X_{\text{PHASE1}}}{t_{1,2} - t_{1,1} - t_{DE}} = \frac{2 \times 100}{352} = 0.57 \mu\text{m/ns}$$

$$\text{The speed of Phase 2; } V_{CF2} = \frac{2\Delta X_{\text{PHASE2}}}{t_{2,2} - t_{2,1} - t_{DE}} = \frac{2 \times (200 - 177)}{90} = 0.51 \mu\text{m/ns}$$

The scanning step was precisely controlled by the stepping motor contributing in the high accuracy in the V_{CF} calculation with the scanning TIM method. The calculated V_{CF} from different scanning positions have the proximate values in range of 0.5-0.57 $\mu\text{m/ns}$ at $I_S = 0.5 \text{ A}$ that are also in accord with V_{CF} done by the other methods. [Remark: this investigation ignored the temperature effect of preheated passage.]

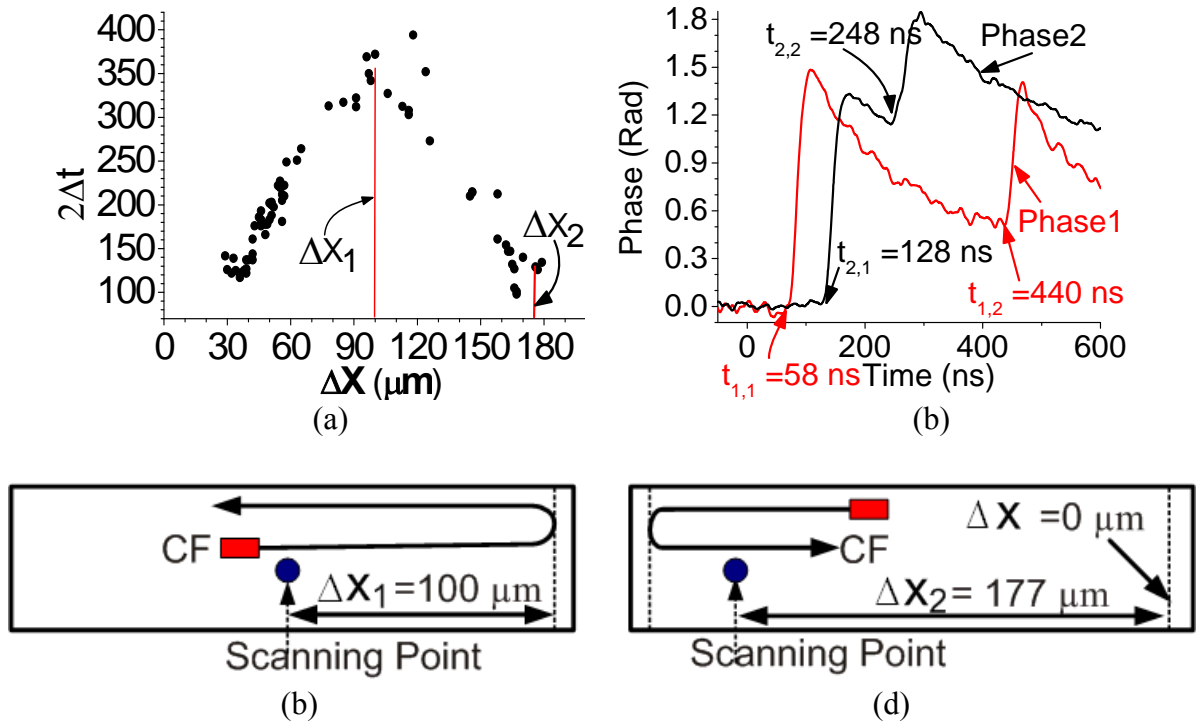


Figure 54 NPN $200 \mu\text{m}$ device was investigated by the Heterodyne scanning TIM method and stressed by 500 ns current pulses at $I_S = 0.5 \text{ A}$. (a) The distances between scanning position and the reference point (at right DE) are plotted as function of the total time ($2\Delta t$). (b) Phase1 and Phase 2 were observed at point $x_1 = 100 \mu\text{m}$ and $x_2 = 177 \mu\text{m}$, respectively. (c) and (d) The schematics of CF movement are interpreted from phases in (b).

3.2.5 Time consumption of CF at device edge

At the arrival moment of CF on DE of linear device, the lasting of induced temperature outside DE results in the insufficient temperature gradient to drive CF to move further to the opposite direction. Therefore a standing CF requires a certain time for

inducing more temperature before leaving DE. This phenomenon had been formerly noticed from the voltage V_{PEAK} in [70], [83]. On the assumption that the induced temperature in the preheated path can last its effect to CF, the time consumption on DE (t_{DE}) would have been speculated.

Figure 55 (a) illustrates the CF activities on DE corresponding to the time instants t_1 , t_2 , t_3 , and t_4 marked in $V(t)$ waveform of Figure 55 (b); t_1 CF is traveling outside DE, t_2 CF arrives DE, t_3 CF is standing at DE, and t_4 CF begins to move in opposite direction. (t_5 will be discussed in later topic.) To simplify the t_{DE} estimation, the period of time during V_{PEAK} rising is approximate to the time to spend on DE ($t_{DE} = t_2 - t_1$).

All ESD PD devices in Table 5, their rising periods $[t_2, t_4]$ of V_{PEAK} , increasing $\Delta V_H \approx 2-3$ V from the holding voltage ($V_H \approx 18-19$ V), cannot be measured simply because the exact time of beginning phase (t_2) was practically difficult to determine from the transient voltage. The t_{DE} estimated from $[t_2, t_4]$ of V_{PEAK} inevitably has a certain deviation from pulse to pulse; therefore, the t_{DE} should be measured by the other methods.

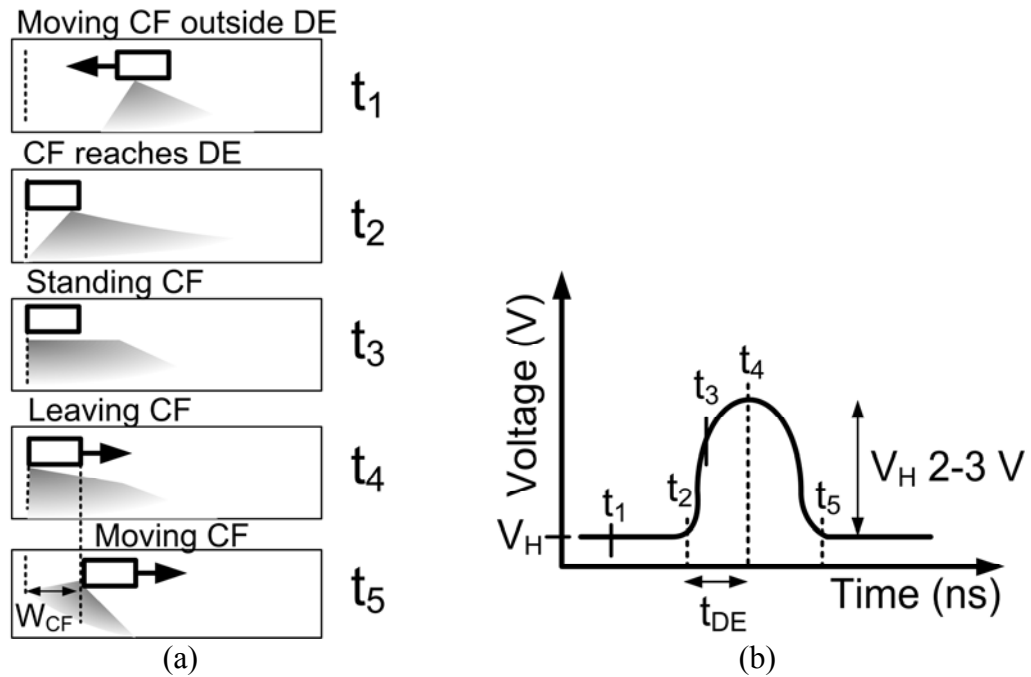


Figure 55 (a) The simplified temperature distributions during CF turnabout DE at five consecutive time instants. (b) The voltage peak, indicating CF turnabout DE, is labeled at instants of t_1 - t_5 corresponding to the activities of CF in (a).

The phase evolution obtained from the Dual Beams Michelson Interferometry offers an accurate estimation of the t_{DE} . The infrared image and moving CF schematic in Figure 56 (a) and (b) demonstrate CF turned around the top DE, where was focused by Laser1. In Figure 56 (c), times of rising signal at Laser2 and Laser1 consequentially increases at t_1 and t_2 . After CF turns around DE corresponding with the occurrence of V_{PEAK} , the increased phase was detected once again at t_3 from Laser2. Therefore the time t_{DE} can be estimated as followed;

$$t_3 - t_2 = t_{DE} + t_2 - t_1$$

$$t_{DE} = (t_3 - t_2) - (t_2 - t_1) \approx 37 \text{ ns}$$

To recheck t_{DE} , the speed V_{CF} was considered from the known distance of 51 μm between two laser beams and the period of rising phase $[t_1, t_2]$;

$$\text{The speed } V_{CF} = \frac{\text{distance between two beams (S}_{2\text{BEAMS}})}{t_2 - t_1} = \frac{51}{352 - 265} = 0.586 \mu\text{m/ns}$$

Then period of rising phase $[t_2, t_3]$ includes the t_{DE} and the time to travel between two focusing beams. Therefore the time t_{DE} is expressed from $t_3 - t_2 - \frac{51}{0.586} = 37 \text{ ns}$, which is consistent result. The time t_{DE} , estimated from the rising period of V_{PEAK} , equals to time of $\approx 40 \text{ ns}$ (marked by t_{inc-V} in Figure 56 (c)), in which a small discrepancy has been included.

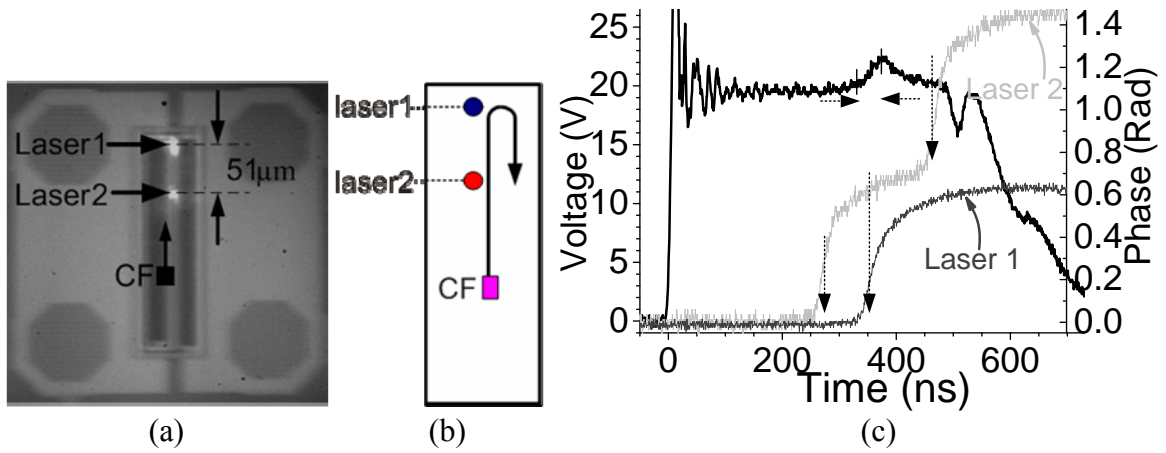


Figure 56 (a) Infrared image of 200 μm NPN_Std device from backside shows one of focusing beams located at the top DE. (b) The moving schematic of CF movement (c) The plot of phases and voltage are measured at $I_S = 0.5 \text{ A}$.

From the result of Figure 56, the t_{DE} was measured while one beam was focused on DE. To observe the deviation of t_{DE} from pulse to pulse, dual beam positions were relocated and lengthened the distance between them to 85 μm as in Figure 57 (a) and (b). The phase detected from Laser2 increased twice at t_2 and t_3 (see Figure 57 (c)), in which the time interval of $[t_2, t_3]$ included the roundtrip time for moving distance $2 \times 10 \mu\text{m}$ and the t_{DE} .

$$\text{Then the time } t_{DE} = (t_3 - t_2) - \frac{2 \times \text{distance between Laser2 and DE}}{V_{CF}}$$

where $V_{CF} = \frac{\text{distance between two beams (S}_{2\text{BEAMS}})}{t_4 - t_3} = \frac{85}{410 - 235} \approx 0.5 \mu\text{m/ns}$, the calculated t_{DE} was about 43 ns, which deviated about 6 ns from the measured result of Figure 56 ($< 16\%$).

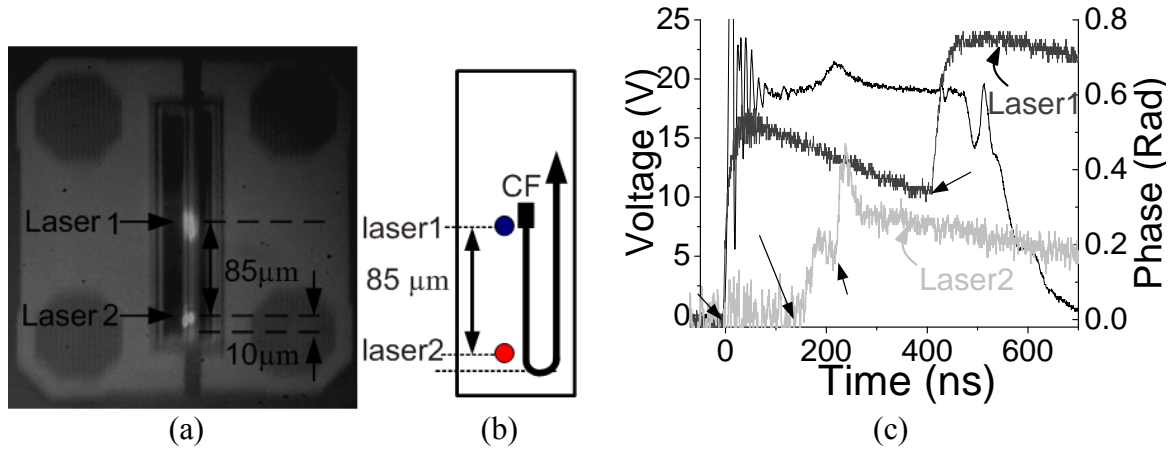


Figure 57 (a) Infrared image of 200 μm NPN_Std device from backside is probed by placing one of laser beams close to bottom edge and another close to the device center. (b) Schematic of filament movement and beams position. (c) Voltage and transient phases are recorded at $I_S = 0.5\text{ A}$, representing CF passed dual beams twice times.

Since the deviation in t_{DE} had been observed in two measurement results of Dual beam Michelson Interferometry setup, the NPN_Dope device was then examined with the Heterodyne scanning TIM method for averaging t_{DE} in case that the initial CF position was fixed.

The scattered power plots in Figure 58 display the CF activity on DE. Two symmetric envelopes of P_{2D} represent a single CF existed at once and moved horizontally from the middle (at $y = 0\text{ }\mu\text{m}$) to either left or right DE (at $y = \pm 100\text{ }\mu\text{m}$). The 1st plot of P_{2D} shows CF traveling close to DE at $t \approx 195\text{ ns}$; afterward, between $t \approx 200 - 230\text{ ns}$ the amplitude of P_{2D} continuously increased with respect to the increasing temperature induced by standing CF on DE. The last plot shows CF began to move again at $t > 240\text{ ns}$. Therefore, the averaged t_{DE} done over 10 pulses per scanning position has the averaged value in range of 30-35 ns, when the NPN device was applied with pulse current of $I_S \approx 0.6\text{ A}$.

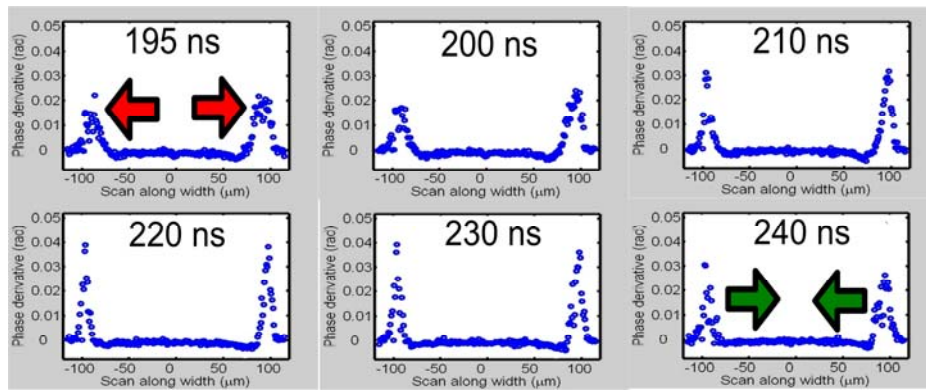


Figure 58 The scattered plots of power distribution (P_{2D}) in the 200 μm NPN_Dope device done by the heterodyne scanning TIM method at $I_S = 0.6\text{ A}$ show the time consumption of standing CF on the device end ($t_{DE} \approx 30\text{--}35\text{ ns}$). Two envelopes were induced by single CF turnabout either left or right DE at each stressing pulse.

3.2.6 Heat energy profile

The temperature distribution cannot be measured directly from the TIM setups; however, the linear relationship between the phase shift $\Delta\phi(t)$ and the temperature change $\Delta T(t)$ of equation [eq-5] allows us to express the temperature from the 2D phase image.

To obtain the information of temperature distribution in space (1-Dimension along the width or 2-Dimension in xy -plane), the cross sectional line passing through the heated spot was selected from the 2D phase image. The amplitude of phase shift $\Delta\phi(t)$ in 1D, induced by moving CF on the edge of emitter region, was investigated in the linear and circular NPN devices.

3.2.6.1 Heat energy distribution in the linear device

The temperature distribution in the linear NPN_Std device (see the layout in Figure 42) was observed by the 2D TIM technique and presented by Figure 59 at the imaging time (t_{IMAGE}) of 75 ns. The hot spot in 2D image induced by CF allows us to trace the journey of moving CF. The location of maximum $\Delta\phi(t)$ corresponds to the CF position at t_{IMAGE} that was induced by the CF temperature (T_{CF}), and the location of minimum $\Delta\phi(t)$ indicates the initial CF position because CF had left this position for the longest time.

The starting position (S), the existing position of CF (F), the 1st pixel of interesting line in space (Cr) were labeled on the 2D phase image in Figure 59 (a) and the phase amplitude was plotted in Figure 59 (b). The steep slope of $\Delta\phi(t)$ corresponds to the front-wall of CF that determines the moving direction of CF toward the right DE.

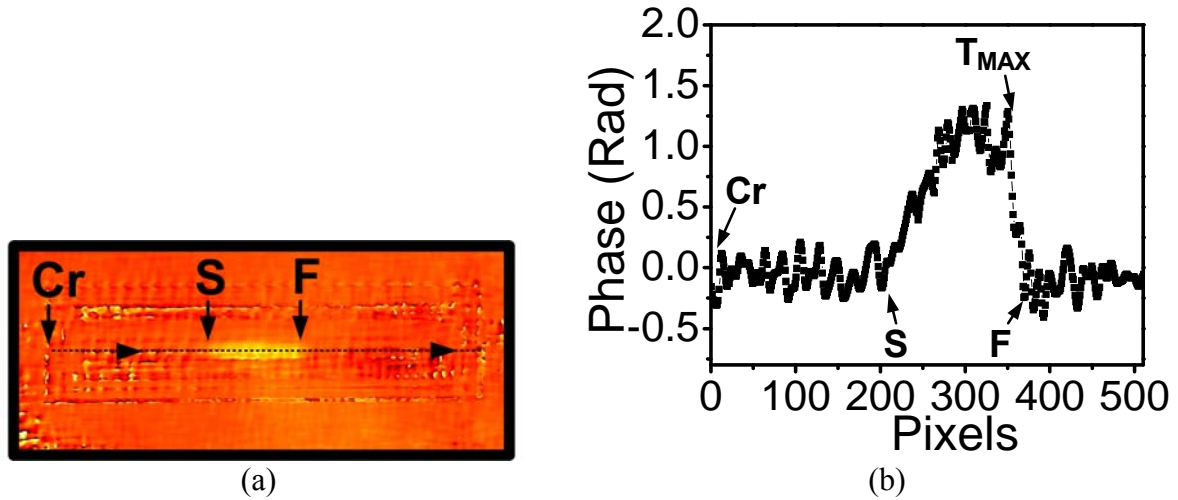


Figure 59 (a) 2D phase image of 200 μm NPN_Std device at $I_S = 0.6\text{ A}$ was captured at $t_{IMAGE} = 75\text{ ns}$ (b) The cross sectional phase along the dotted line in (a) is presented with interesting points: Cr = the 1st pixel of cross sectional phase, S = Starting CF position, F = the existing CF position at t_{IMAGE} , and T_{MAX} = Maximum temperature at the back wall of CF. (CF moved toward the right DE.)

3.2.6.2 Heat energy distribution in the circular device

The temperature distribution in NPN device with circular structure (NPN_Round) had been observed with the 2D TIM technique. The 3D schematic and cross section of Figure 60 (a) and (b) show the NPN_Round device is composed of the P⁺Diffusion as the innermost region enclosed by N⁺Emitter forming the base-emitter junction that was shorted to ground. The N⁺Buried Layer, located at the junction depth of collector-base, is electrically stressed with ESD pulses via N⁺Sink contact.

The investigated results of NPN linear device present the random CF always was triggered along the N⁺Emitter edge; therefore the perimeter of round N⁺Emitter region was expected to observe a moving CF. Figure 60 (c) is the infrared image from device backside with indicated diameter of emitter ($d_{Emitter} = 34 \mu m$), where CF moves along the perimeter. (One rotational has distance of $107 \mu m$)

2D TIM image of the circular device (NPN_Round) for ESD pulse of 115 ns, 0.45 A is given in Fig. 61 (a). The $\Delta\phi(t)$ distribution along the circular line, marked with the dotted circle, is given in Figure 61 (b). The 1st pixel of cross sectional line Cr in Fig. 61 (a) is indicated in Fig. 61 (b). The start position and the front-wall of CF are labeled with S and F respectively. The maximum $\Delta\phi(t)$ corresponds to the position of back-wall of CF, where has the maximum temperature (T_{MAX}).

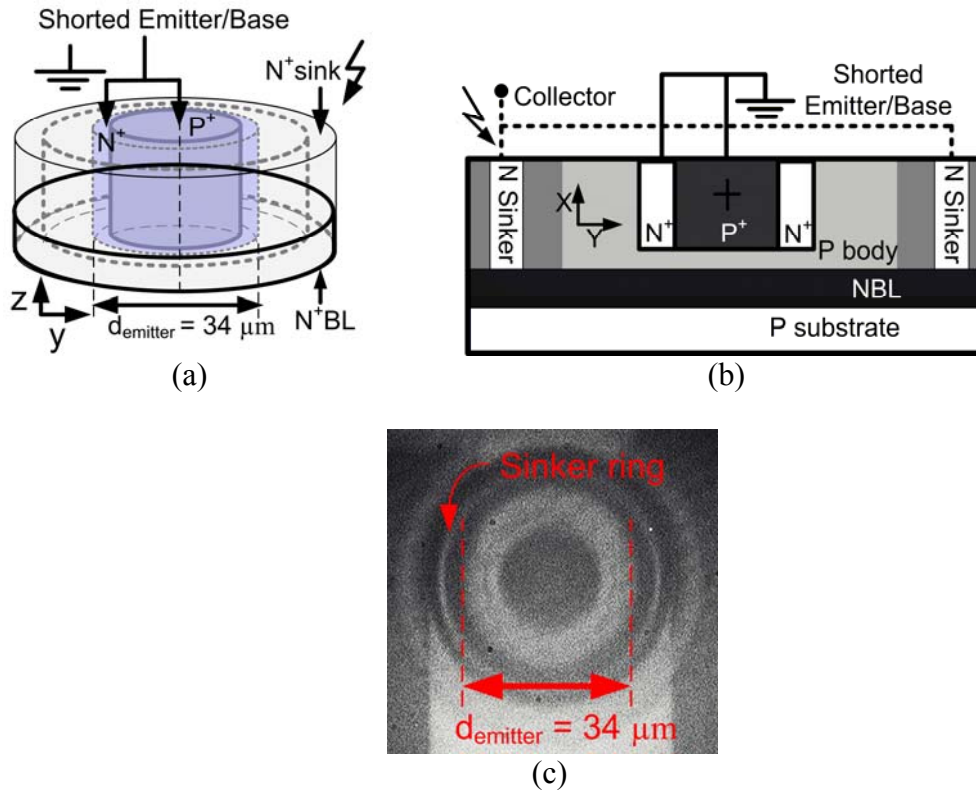


Figure 60 (a) 3D schematic of circular NPN device (NPN_Round). The P⁺Diffusion as innermost region is surrounded by N⁺Diffusion forming the emitter/base junction. The N⁺Buried Layer served as the collector is stressed with ESD pulse via the outermost N⁺Sink. (b) The cross section of NPN_Round device (c) The infrared image of device backside is marked the diameter of moving passage; one roundtrip distance is $107 \mu m$.

The steep incline of $\Delta\phi(t)$ between the 170th - 210th pixels responses to the temperature within inside W_{CF} (T_{CF}). At cold areas $\Delta\phi(t)$ is near zero. The maximum $\Delta\phi(t)$ has amplitude twice times greater than the $\Delta\phi(t)$ at S according to CF left the initial position S for 115 ns. The lasting temperature can be minimized by enlarging the circumference of emitter region that allows more heat to dissipate before CF travels in the next rotation.

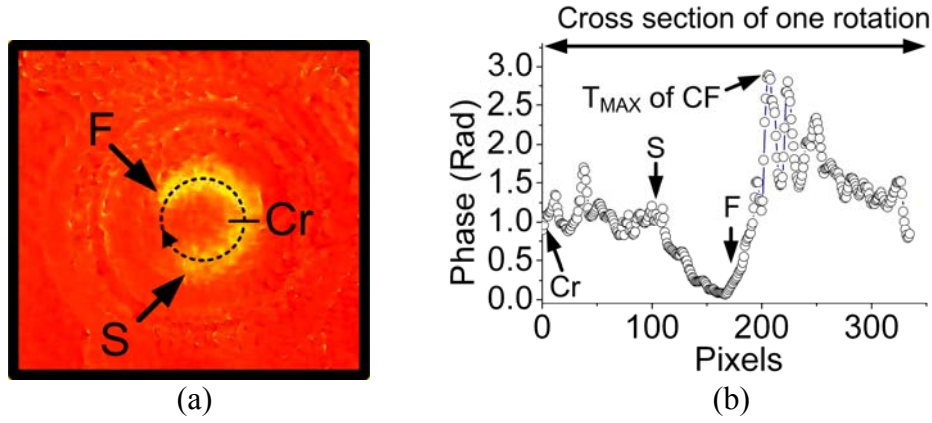


Figure 61 (a) 2D phase image of NPN_Round device at $I_S = 0.45$ A, captured at $t_{IMAGE} = 115$ ns, was marked with interesting positions; S = Starting CF position, F = Existing position of CF at t_{IMAGE} , and Cr = the 1st pixel of circular cross sectional line (b) Phase amplitude along the dotted circular line in (a) was selected in clockwise rotation.

3.2.7 Temperature in the moving CF

The temperature has a strong influence to the CF behavior and the device reliability. The optical measurement techniques cannot directly probe the induced temperature in the moving CF (T_{CF}). 3D thermal simulation was done in order to study the temperature in the moving CF by COMSOL software [84]. The simulation focused on the moving CF under adiabatic boundary conditions in the linear NPN_Std device.

The CF model with simulation parameters is summarized in Table 6 and demonstrated in Figure 62 (a). Half of CF, having symmetric xz -plane, is simulated when it was moving at constant speed $V_{CF} = 0.5$ $\mu\text{m/s}$ and its power density of 36 mW/ μm^3 ($I_S = 0.35$ A, power of 7.3 W). The temperature of traveling CF was obtained by solving quasi-steady heat equation for a localizing heat source. [85]

The 3D temperature distribution of Figure 62 (c) shows the CF temperature at the depth of collector-base junction. The maximum temperature at the back-wall of moving CF (T_{CF-MAX}) was 367 °C that happened a location where was heated by a moving heat source for the longest time, see Figure 62 (b). [84]

Parameters	Value	Comment
Speed (V_F)	0.5 $\mu\text{m}/\text{ns}$	A slight difference between the speed of incoming and returning CF is neglected
Width (W_F)	11.3 μm for $I_S = 0.35$ A	Linear interpolation is taken for other currents
Length (L)	9 μm	
Height (H)	2 μm	
Distance of CF to surface (D)	3 μm	
Power density	36 $\text{mW}/\mu\text{m}^3$	Corresponds to total power of 7.3 W ($I_S=0.35$ A)
Standing time on DE (t_{DE})	20 ns	
Device width	200 μm	

Table 6 Filament model parameters used in 3D thermal simulations in Figure 62.

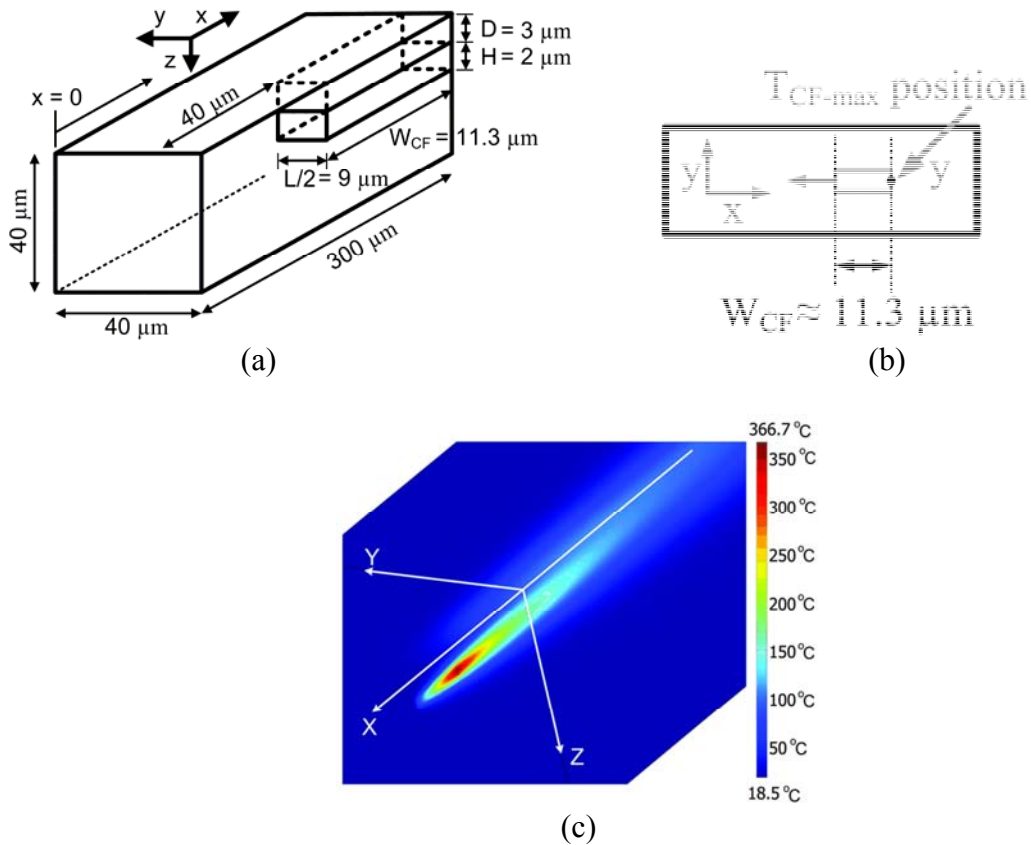


Figure 62 (a) 3D models of moving CF in the linear device with simulation parameters. (b) The layout of moving CF in xy-plane presents the maximum temperature at the CF back wall (T_{CF-MAX}). (c) 3D thermal simulation of traveling filament was done in the adiabatic conditions at $I_S = 0.35$ A. [84], [86]

3.2.7.1 Transient temperature at a fixed point on DE during CF turning around

There is interesting to observe the transient temperature at a fixed position on DE, in order to investigate how much the induced temperature by moving CF remains on DE at the return time (t_{TURN}). The transient temperature at t_{TURN} has an effect on standing CF at DE in long duration pulse.

The temperature evolutions were concentrated at five time instants as illustrated by Figure 63 (c). The explanation of CF activities are including; “1” the back-wall of CF passes by the investigated point close to left DE (at $x = W_{CF}$), “2” The standing CF begins to leave the left DE, “3” The back-wall of CF leaves the investigated position, “4” CF is turning around the right DE, and “5” CF returns to the preheated left DE at $t_{TURN} \approx 840$ ns.

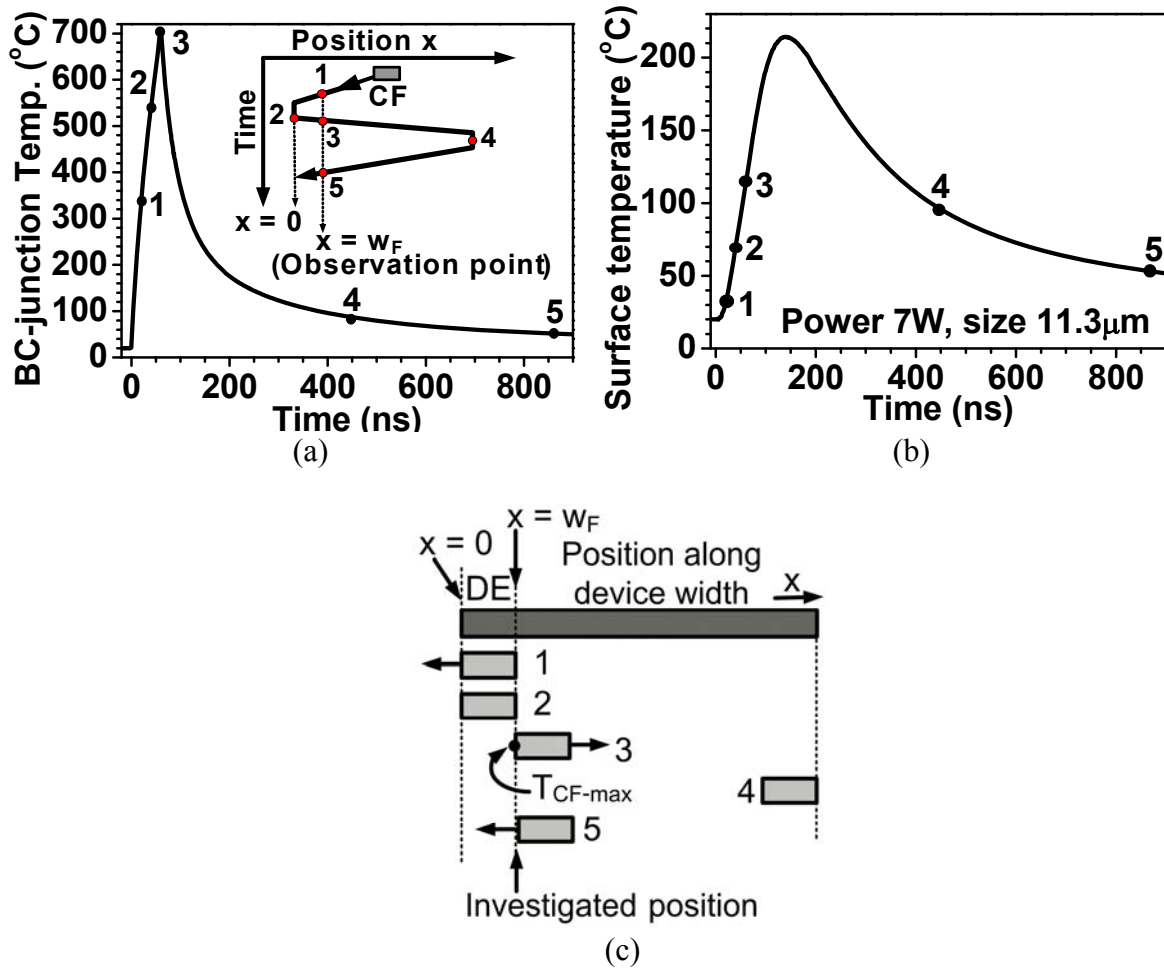


Figure 63 Temperature evolutions were simulated at (a) The depth of collector-base junction and (b) The surface of linear NPN_Std device with 200 μm width. The inset in (a) describes the CF activities at different five instants that are also marked on both curves. Time consumption of CF to reach the preheated DE, where the temperature has been lasted, was about 840 ns (t_{TURN}) (c) The schematic demonstrates the investigated position where the temperature was maximum (T_{CF-max}). [84], [86]

With the same simulation parameters of 3D simulation of CF as a moving heat source in Figure 62 (c), the temperature evolution at the investigated point ($x = W_{CF}$) on left DE are simulated at the depth of collector-base junction ($x = W_{CF}$, $y = 0$, $z = 0 \text{ } \mu\text{m}$), see Figure 63 (a). The maximum temperature at $x = W_{CF}$ was about 700°C that is nearly twice time greater than the simulated T_{CF} of $\approx 367^\circ\text{C}$. The large difference in temperature is caused during CF standing for a short period on DE (t_{DE} = time between “1” – “3” that was illustrated with the inset of Figure 63 (a)). The temperature at the same point ($x = W_{CF}$) are also simulated at the device surface ($x = W_{CF}$, $y = 0$, $z = 5 \text{ } \mu\text{m}$), see Figure 63 (b). The surface temperature is much lower than the temperature at depth junction because of the delay in heat transport.

The thermal simulation results are evaluated at the position where coincides with the back-wall of CF while it has been standing on DE, therefore the temperature reaches the maximum value at “3” and then decreases after CF departs this point. The transient voltage at moments “2” and “3” correspond to V_H at t_4 and t_5 in Figure 55 (b), respectively. When CF returns back to the preheated DE at the return time ($t_{TURN} = 840 \text{ ns}$), the simulated temperature shows the lasting temperature at junction depth is around 52°C . In which the background temperature on DE at “5” have influence to CF behavior.

3.2.8 CF as a probe of access resistance in different device shapes

The holding voltage change in $V(t)$ of vertical NPN device has been previously studied in [87]. The change of V_H magnitude has been found that is relevant to the diluting of N^+ BL doping concentration; the more doping concentration in BL is diluted, the higher V_H will be observed [26].

In addition, the voltage change such as V_{PEAK} is a result of increasing temperature with lower impact ionization rate, when CF turns around on DE that was formerly discussed in [3]. Various shapes of devices in Table 5 were performed the IV measurement and their transient voltages exhibit the alteration in V_H amplitude. Without the optical TIM methods, it was not possible to elucidate the CF behaviors in respect to the V_H change ($\pm \Delta V$).

The existing position of moving CF in 2D phase image will be identified in respect to the amplitude of V_H at time t_{IMAGE} . The meander and oval structures of ESD NPN devices will be discussed. We will show that steps in voltage waveform can directly identify the actual position of CF in the structure.

3.2.8.1 Moving CF in Meander structure

The meander structures of NPN devices with two finger and three fingers (NPN_Meander2 and NPN_Meander3) are presented by the layouts of Figure 64 (a) and (b) respectively. The P^+ Diffusion area is situated as the innermost region and its boundary is parallel with the N^+ Diffusion region. These parallel regions serving as the emitter-base junction are shorted to ground. The N^+ Sink region acting as the collector contact is not collinear with the emitter edge for the entire CF passage. To complete one roundtrip of CF in two and three fingers devices, CF has to spend time $t \approx 1000$ and 1500 ns on traveling through distance $\approx 500 \text{ } \mu\text{m}$ and $750 \text{ } \mu\text{m}$ at $V_{CF} = 0.5 \text{ } \mu\text{m/ns}$, respectively.

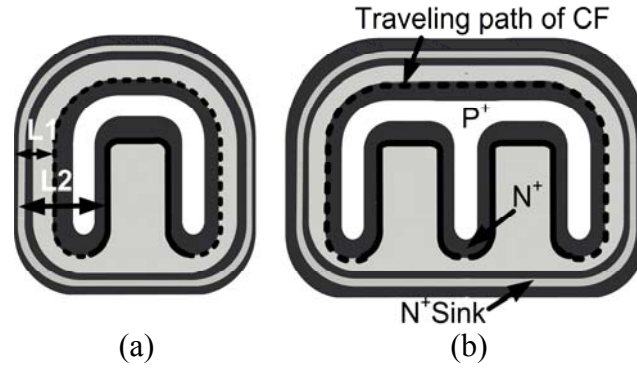


Figure 64 The schematic of meander NPN devices (a) two fingers device (NPN_Meander2) (b) three fingers device (NPN_Meander3); Moving CF was found on the emitter edge marked with the dotted and solid lines.

To compare the cross sectional view of meander device with linear (or round) device, the difference is that the N^+ Emitter edge and N^+ Sink edge of meander structure do not collimate in the direction of current flow along the entire CF path, see Figure 66 (b). During CF moves along the finger, the emitter current flows through the inconstant N^+ BL region toward the collector contact (N^+ Sink). The distance between N^+ Emitter edge and N^+ Sink edge, determining the Ohmic length (L), alters between $L1$ and $L2$, which are represented with the dotted line and solid lines in Figure 65 (b). The direction of current flow in meander finger is presented with the electrical schematic in the cross sectional layout in Figure 65 (a). When CF moves close to N^+ Sink edge (on the dotted line: $L1$), the access resistance (R_{A1}) plays a role on the voltage drop across the junction. Once it travels on the far edge from N^+ Sink (on the solid line: $L2$), the access resistance increases to R_{A2} that is equivalent to $R_{A1} + \Delta R_A$. The change of R_A (ΔR_A) leads to the voltage change when the meander device is stressed with a long duration pulse at constant I_S .

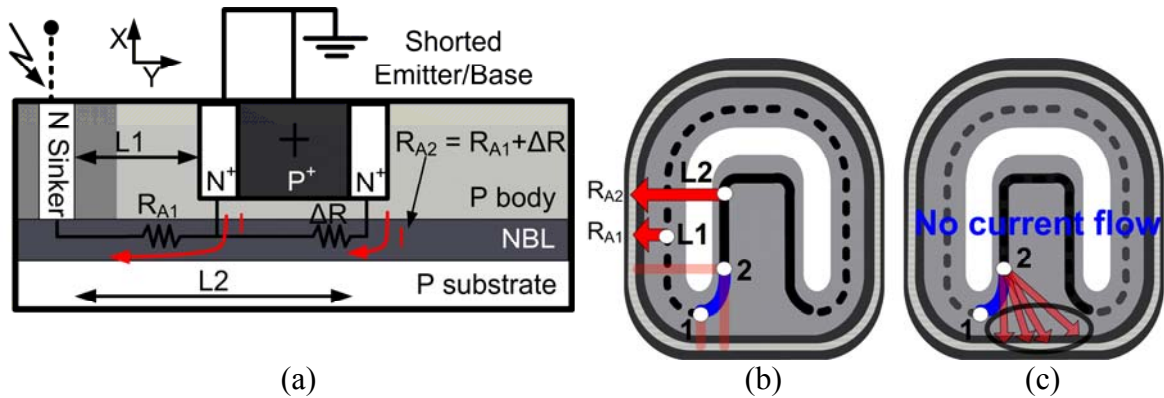


Figure 65 (a) The cross section of NPN_Meander2 shows distances $L1$ and $L2$ between N^+ Emitter and N^+ sinker. The electrical schematic presents the access resistance (R_A) in N^+ Buried layer (b) The current flows laterally through distances of $L1$ and $L2$, when CF travels on the dotted and solid path. Between position 1 and 2 the resistance continuously changes over from R_{A1} to R_{A2} (c) At position 2, the current prefers not to flow to the far N^+ Sink (collector).

From pulse to pulse the measured $V(t)$ waveforms of meander device in Figure 66 (a) are selected to represent three cases mainly found; Case 1: constant V_H , Case 2: voltage decrease by $\Delta V \approx 0.7$ V to V_H , and case 3: voltage increase from V_H to $V_H + \Delta V$. The 2D phase images at one time instant make the relationship between CF in meander device and V_H understood. The phase images of NPN_Meander2 device and NPN_Meander3 device in Figure 67 were captured at different t_{IMAGE} when devices were stressed with long pulses at $I_S = 0.5$ A generated from DMOS pulser. The moving direction, the initial CF position and the existing CF position at t_{IMAGE} are identified from the different degree of $\Delta\phi(x,y,t)$ in the heated area; the arrow indicates the moving direction.

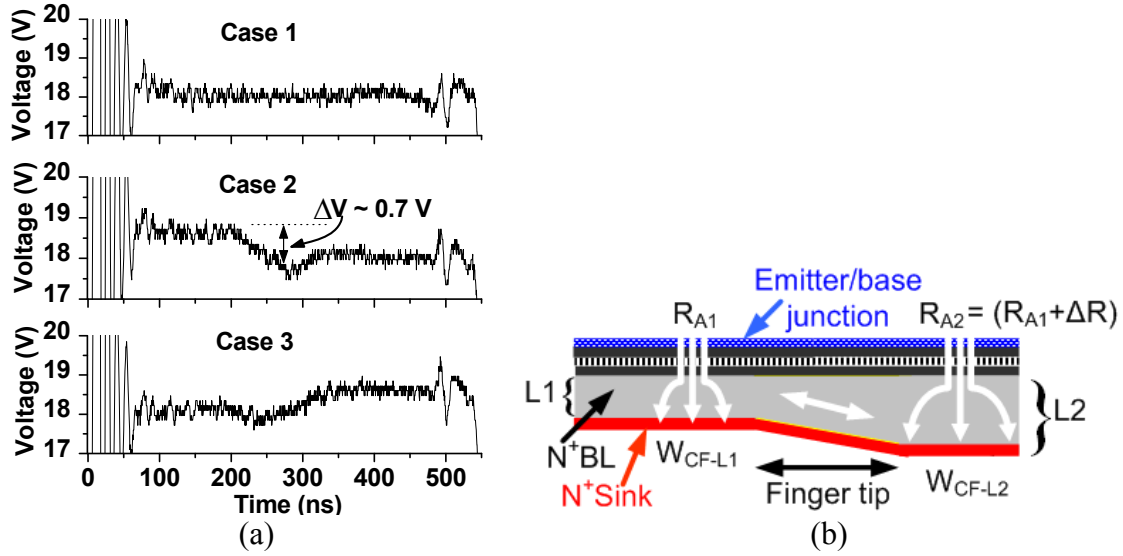


Figure 66 (a) Three $V(t)$ waveforms were mainly observed in the NPN_Meander2. (b) The schematic displays the current laterally spreads through N⁺BL regions with distances of L1 and L2 where have different R_A . (The voltage transition occurred when CF is moving on the finger tip.)

The heated area is located randomly and had a different length due to the different t_{IMAGE} . At constant $I_S = 0.5$ A the voltage amplitude within the long stress duration altered between V_H and $V_H + \Delta V$. Voltages of Case 1-3 in Figure 66 (a) are interpreted with three filamentary modes in 2D phase images in Figure 67. The voltage amplitude was observed that it has a relation with the CF location in meander path. The voltage change is consequence of the altered access resistance R_{A1} and R_{A2} ($R_{A2} = R_{A1} + \Delta R$) that are summarized with schematics in Figure 67 (g)-(i) and discussed as three following cases;

Case 1: Near constant voltage (R_A constant)

The heated region in 2D phase images of Figure 67 (a) and (d) demonstrates the triggered CF traveled along the passage with constant R_A for all the stressing time. Figure 67 (g) indicates the moving CF passage with respect to the constant $V(t)$ of Case 1 ($V(t) = V_H = \text{constant}$).

Case 2: Voltage decrease ($R_{A2} \rightarrow R_{A1}$)

From the pulse onset, the $V(t)$ has the higher amplitude than the $V(t)$ in Case 1 by $\Delta V \approx 0.7$ V. The voltage in Case 2 of Figure 66 (a) decreased to the $V(t)$ in Case 1 from $t > 200$ ns until the pulse end. The different degree of $\Delta\phi(x,y,t)$ in Figure 67 (b) and (e) indicates CF

moved from the region with high R_{A2} (L2) and entered the region with low R_{A1} (L1), see the summarized schematic in Figure 67 (h).

Case 3: Voltage increase ($R_{A1} \rightarrow R_{A2}$)

On the contrary of Case 2, the $V(t)$ amplitude of Figure 66 (a) began increasing the amplitude to $V(t) + \Delta V$ from $t > 230$ ns. The 2D phases images of Figure 67 (c) and (f) present CF traveled from the meander path with low R_{A1} (L1) to enter the region with high R_{A2} (L2) as illustrated with Figure 67 (i).

The moving CF in two regions of meander path leads to the $V(t)$ change that is expressed by the relations;

$$\begin{aligned} V_{L1} &= R_{A1} \cdot I + V_{PN} \\ V_{L2} &= R_{A2} \cdot I + V_{PN} \end{aligned}$$

The difference in access resistance (ΔR_A) was estimated from;

At $I_S = 0.5$ A,

$$\begin{aligned} \Delta V &\approx 0.7 \text{ V} = I_S(R_{A2} - R_{A1}) \\ \Delta R_A &= R_{A2} - R_{A1} \approx 1.4 \Omega \end{aligned}$$

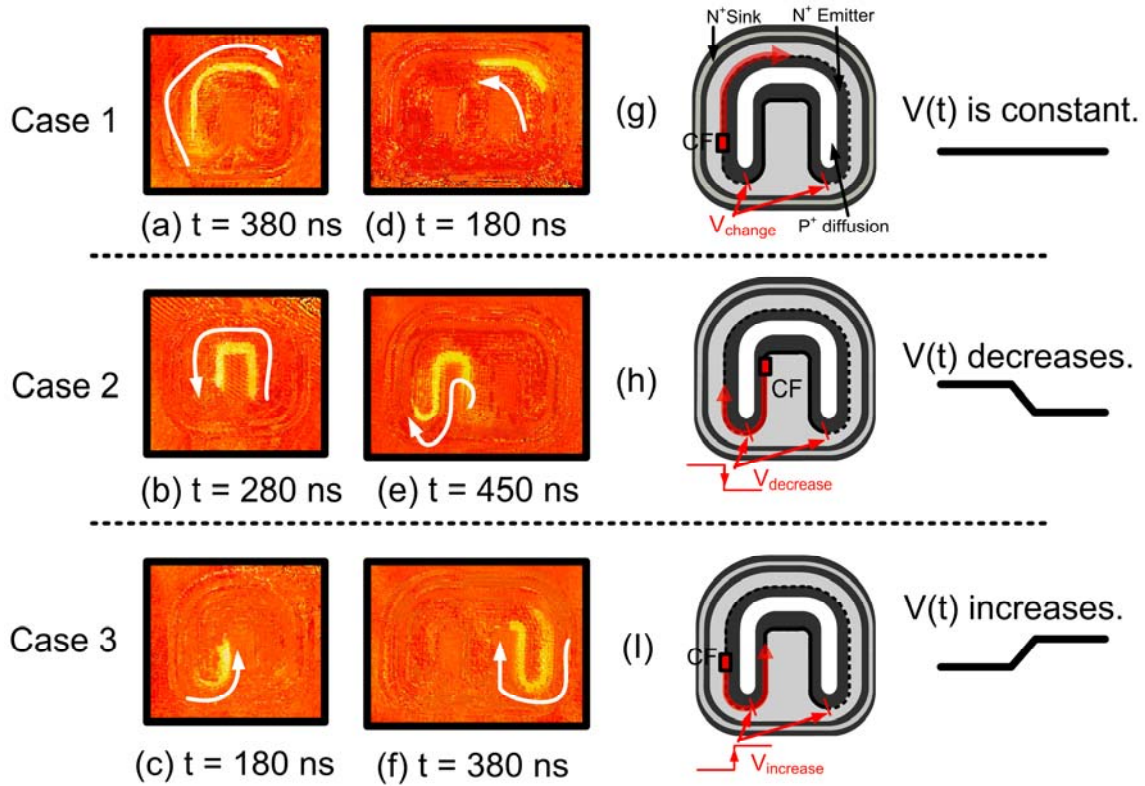


Figure 67 (a)-(c) 2D phase images of NPN_Meander2 (length of CF path $\approx 497 \mu\text{m}$). (d)-(f) 2D images of NPN_Meander3 (length of CF path $\approx 757 \mu\text{m}$). Devices were stressed at $I_S = 0.5$ A. Three cases were primarily observed in relevant to $V(t)$ waveforms and summarized with the moving CF schematics (g)-(i).

The current distributing in N^+ BL of the NPN_Meander2 and NPN_Meander3 flowed to the collector (N^+ Sink) in the tangential direction to the CF location as marked with the arrows in Figure 65 (b) and it preferred not to flow to far BL as indicated by arrows in Figure 65 (c). Between point 1 and 2 of device finger in Figure 65 (b) has the access resistance change between R_{A1} and R_{A2} having the effect on the current distribution in N^+ BL as presented by Figure 66 (b). The lateral spreading of current in this Ohmic layer is related to W_{CF} at a constant I_S , in which the W_{CF} in the passage through layer R_{A2} has a likelihood to be larger [80] than the W_{CF} in the passage with lower R_{A1} ($W_{CF-L2} > W_{CF1-L1}$). However, the W_{CF} in meander devices has never been experimentally measured.

In conclusion, the inspection of these results indicates that the CF behaves as “a resistance probe” along the meander passage with the change of Ohmic length L of buried layer. The voltage drop across the collector/base junction responses to the change of R_A in the passive Ohmic layer (N^+ BL).

3.2.8.2 Moving CF in Oval structure

The layout of NPN_Oval device has the P^+ Diffusion as innermost region coupled with the N^+ Emitter region forming the oval shape of emitter-base junction see the schematic in Figure 68 (f). The stripe shape of N^+ Sink locates along one-sided of the oval N^+ Emitter. One of parallel sides of oval device ($S1$) is closer to N^+ Sink than another side ($S2$). The Ohmic length L between edges of N^+ Sink and N^+ Emitter is not constant throughout the oval CF passage; therefore, the R_A in the N^+ BL layer where current laterally spreads is changed likewise as observed in the Meander device.

The $V(t)$ of oval device changed in the same fashion with the $V(t)$ of meander devices, see the waveform in Figure 68. The 2D images in Figure 68 (a)-(e) are selected at five time instants for correlate with the voltage amplitude at t_{IMAGE} .

Image (a) and (e): CF was moving along the straight section close to the N^+ Sink edge ($S1$) and the $V(t_{IMAGE})$ was approximate to ≈ 18.6 V.

Image (c): CF was moving along the straight section far from the N^+ Sink edge ($S2$) and the $V(t_{IMAGE})$ had increased to ≈ 20 V.

The 2D phase images of oval device present the consistent result with the meander device that moving CF responses to the change of R_A . The different access resistance (ΔR_A) between two parallel sections ($S1$ and $S2$) could be calculated from;

$$\begin{aligned} \text{At } I_S = 0.45 \text{ A,} \quad \Delta V &\approx 20 - 18.6 \text{ V} = I_S(R_{A2} - R_{A1}) \\ \Delta R_A &= R_{A2} - R_{A1} \approx 3.1 \text{ } \Omega \end{aligned}$$

Two curvatures of oval device have more complex device characteristic due to the transition of Ohmic length L ($L_{S1} \leftrightarrow L_{S2}$). The 2D images (b) and (d) indicate CF was traveling on the curvature of oval structure and $V(t)$ alternated between ≈ 18 and 20 V (and vice versa). Even the Ohmic length L at two midpoints of curvature ($L_{P1(2)}$) is shorter than L_{S2} , the maximum voltage (V_{MAX}) of about 21 V was observed during CF visiting these midpoints $P1$ and $P2$, see the layout in Figure 68 (f). The V_{MAX} relates to the effect of highest base resistance (R_B) in the smallest junction of emitter-base at these midpoints. The R_B could be estimated to;

At $I_S = 0.45$ A,

$$\Delta V \approx 21 - 18.6 \text{ V} = I_S(R_{A2} - R_{A1} + \Delta R_B)$$

$$\Delta R_B \approx 2.2 \text{ } \Omega$$

Not only CF responds to the access resistance change, but CF also senses the base resistance change. Furthermore the effect of R_B change could play a more active role on the device voltage than the R_A change.

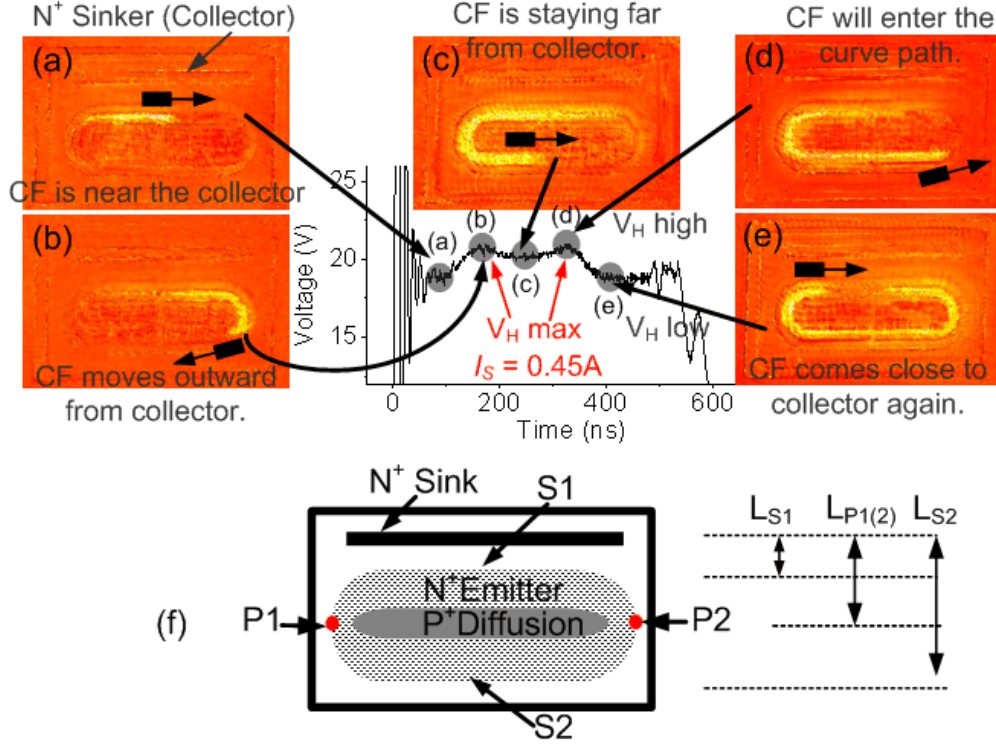


Figure 68 The 2D phase images (a)-(e) show the moving CF at various positions on the N⁺ Emitter edge of NPN_Oval device at $I_S = 0.45$ A. (f) The layout of oval device have the different Ohmic lengths (L_{S1} , $L_{P1(2)}$, and L_{S2}). The holding voltage changes in relevant to CF location; V_H low means that CF is staying close to the N⁺ Sink. The maximum of V_H indicates that CF moves past either points P1 or P2. [84]

3.2.9 Effect of buried layer resistance change during CF passage on the change in filament speed

The voltage peak (V_{PEAK}) changes according to the induced temperature change during CF turnabout DE. The voltage change observed in meander or oval devices has been found due to the electrical characteristic in each device structure. This topic focuses on the effect of resistance change (R_A and R_B) to the CF behavior.

Two $V(t)$ waveforms of NPN_Oval device are compared in Figure 69 (c), and two CF motions interpreted from the voltage change are illustrated with Figure 69 (a) and (b). CF in Mode A started within the passage of low R_A , and CF in Mode B started within the passage of high R_A .

The times of full width at half maximum of Mode A and B (t_A and t_B) are not equal. CF spent time t_A on distance between $P1$ and $P2$ by passing through passage $S2$; nevertheless, it spent a shorter time t_B on the same distance (half of the oval passage) by passing through passage $S1$, see the time description in Figure 69 (b).

$$t_A = t_3 + t_4 + t_5$$

$$t_B = t_6 + t_1 + t_2$$

The time t_A is about 70 ns longer than the time t_B ($t_A > t_B$). Therefore CF moved at a slower V_{CF} when it had entered the high resistive passage $S2$ and moved at a faster V_{CF} in the passage $S1$.

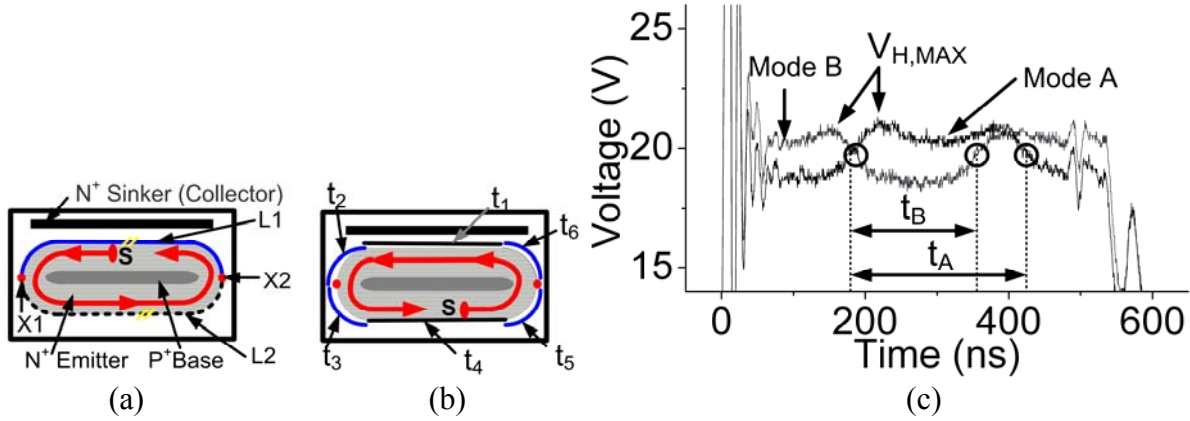


Figure 69 (a) The layout of NPN_Oval device shows CF starts the journey from $S1$ with low R_A (Mode A) (b) Schematic of CF moving from $S2$ with high R_A (Mode B) marked with time consumptions along various sections t_1 - t_6 (c) Waveforms of Mode A and B were compared to present the change of CF speed at the constant pulse at $I_S = 0.45$ A. [84]

3.2.10 Effect of preheated region induced by moving Current Filament

ESD stressing with long pulse duration forces CF to travel a distance longer than one roundtrip ($\tau > t_{TURN}$). Once CF returns to its initial position or overlaps the previous passage, the induced temperature lasts on the passage to superimpose the CF temperature (T_{CF}) at the t_{TURN} . This background temperature has the influence to CF behavior that will be discussed through the experiments as followed;

3.2.10.1 Effect of preheated region on the device voltage

The $V(t)$ waveform with long duration of about 700 ns was measured from the 100 μm linear device (NPN_Std) at $I_S = 0.34$ A, see Figure 70 (a). Three peaks (P1, P2, and P3) indicate that CF turnabout DE three times, and the 3rd V_{PEAK} related to CF turnabout the

same DE of the 1st V_{PEAK} . The CF traveled about three passages between two DEs and its motion is illustrated with the Figure 70 (b).

The $V(t)$ amplitude increased slightly from the previous passage to the next passage. The increase of holding voltage (ΔV) indicates the temperature effect that was induced by CF from the previous passage. This inhomogeneous background temperature has accumulated on the passage so long as the moving CF induced the temperature change.

In addition the $V(t)$ waveform of circular device (NPN_Round2) has continuously increased as like as the staircase, see Figure 70 (c). The circular NPN device has the circular CF passage permitting CF to travel forward without changing the direction (see Figure 70 (d)); therefore, the V_{PEAK} has not been observed. Each voltage step ($\Delta V \approx 0.35$ V) appears at time of CF complete one rotation according to CF enters the higher temperature of round passage.

The slightly increase voltage in waveform of linear and oval devices is the consequence of CF traveling through the increased temperature area induced by CF from the previous passage, but it does not relate to the effect of resistance change ($R_A + R_B$) as observed in the meander structure or oval structure.

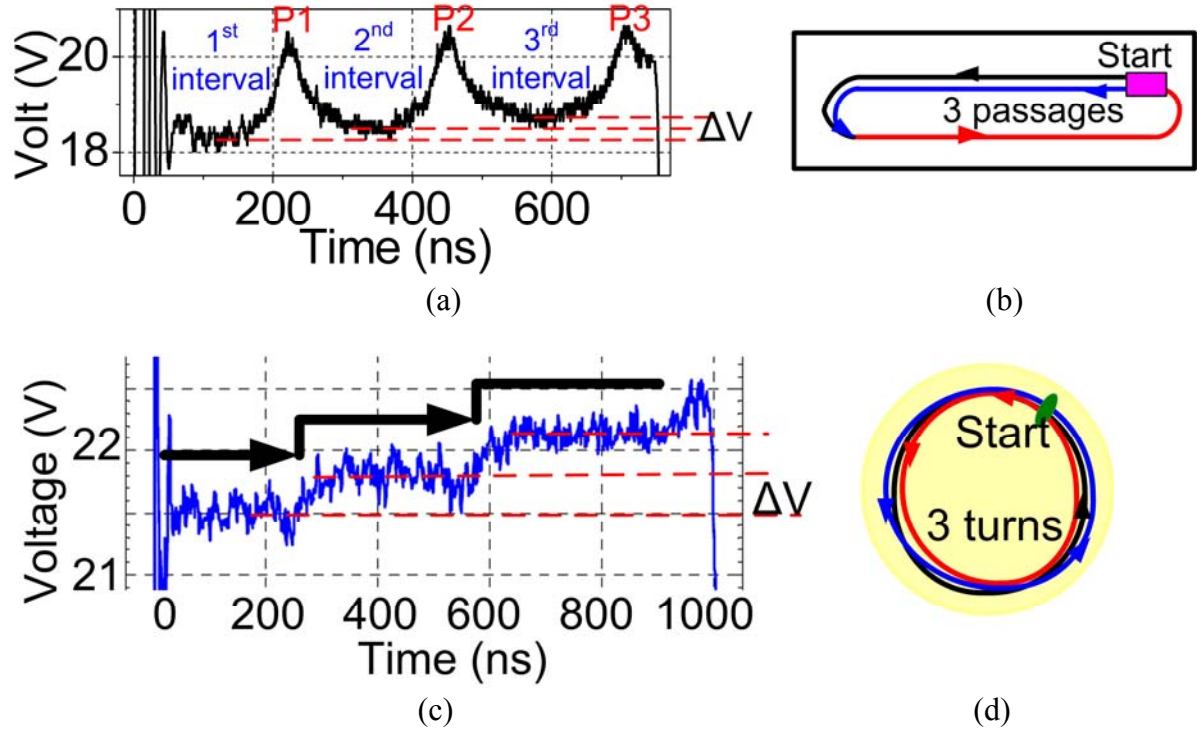


Figure 70 (a) The holding voltage of linear NPN_Std device at $I_S = 0.34$ A increases stepwise with the number of moving passages, illustrated by (b). (c) Voltage of circular NPN_Round2 device increases as the staircase. [88] Each step appears when CF completes one rotation, illustrated by (d).

3.2.10.2 Effect of preheated region on filament speed

When CF moves through the higher temperature passage, not only the small voltage change was found but the change of filament speed (V_{CF}) was also observed. The NPN_Std devices with four device widths (W_D) including 100, 200, 300, and 400 μm had been

stressed with the extended pulse durations ($\tau \approx 700 - 2100$ ns) at $I_S = 0.4$ A. Three V_{PEAK} in waveforms of Figure 71 (a) present CF traveled distance of about $2W_D$ as illustrated by Figure 71 (b).

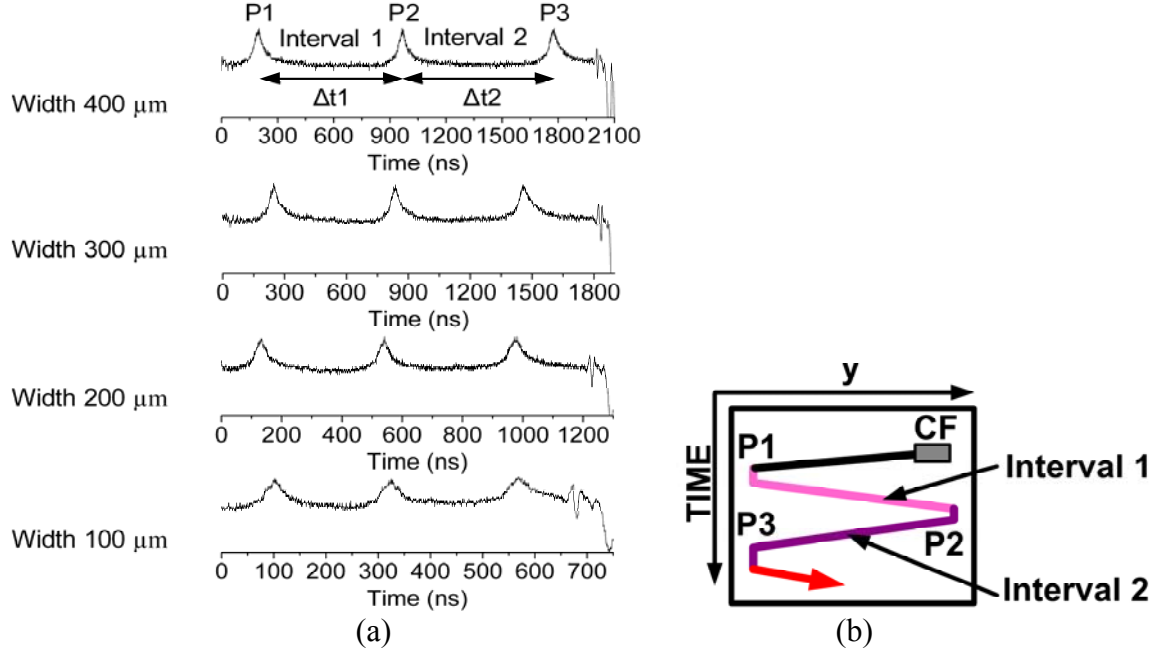


Figure 71 (a) The voltage waveforms were observed at $I_S = 0.4$ A in the varied widths of NPN Std device; CF spent the time $\Delta t1$ on the 1st passage and the longer time $\Delta t2$ on the 2nd passage (the preheated path). (b) Moving CF schematic of waveforms in (a).

Device Width (μm)	Interval 1 ($\Delta t1$) (ns)	Interval 2 ($\Delta t2$) (ns)	$V_{CF1} = \frac{W_D}{\Delta t1 - t_{DE}}$ [$\mu\text{m/ns}$]	$V_{CF2} = \frac{W_D}{\Delta t2 - t_{DE}}$ [$\mu\text{m/ns}$]
400	769	812	0.54	0.51
300	592	626	0.53	0.50
200	407	434	0.53	0.49
100	223	244	0.52	0.46

Table 7 CF speeds in NPN Std devices with different widths were measured at the fixed $I_S = 0.4$ A. The speeds of CF moving through the preheated passage (Interval 2) were always less than the speed through non-heated passage (Interval 1).

Two time intervals between two maximum peaks ($\Delta t1$ and $\Delta t2$) in waveforms of all device widths at $I_S = 0.4$ A are summarized in Table 7. CF always spent a longer time on traveling through the preheated passage ($\Delta t1 < \Delta t2$). The filament speed in the 1st passage (V_{CF1}) was higher than speed in the preheated passage ($V_{CF1} > V_{CF2}$).

Therefore the V_{CF} decreases inversely proportional to the increase of background temperature in the CF passage during the long pulse duration.

The amplitude 1st V_{PEAK} and 2nd V_{PEAK} (3rd V_{PEAK}) are compared in Figure 72 (a) (Figure 72 (b)), the amplitude and width of the latter peak was larger than the former peak, see the inset. The reason of larger V_{PEAK} has not been elucidated, and to establish the answer

the Dual Beams Interferometry technique is suitable for investigating CF at DE. Consequently, the CF speeds in Table 6 were only related to the induced temperature in preheated path. The t_{DE} and time between the pulse onset ($t = 0$) to middle peak P1 have been neglected for simplified calculation.

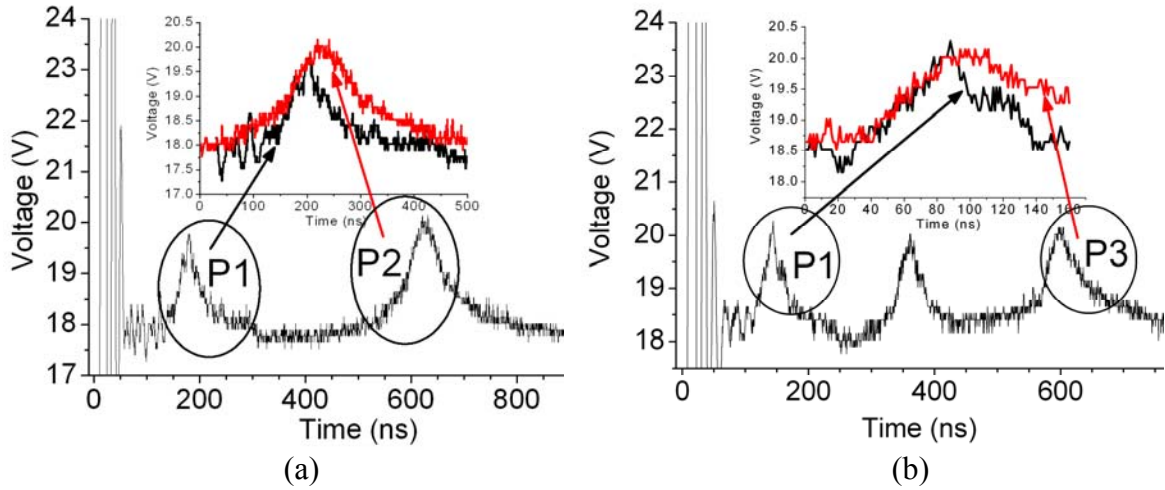


Figure 72 (a) Voltage waveform of 200 μm NPN_Std device at $I_S = 0.4$ A ; the 1st and 2nd peaks are compared in the inset. (b) Voltage waveform of 100 μm NPN_Std device at $I_S = 0.265$ A; the 1st and 3rd peaks are compared in the inset.

3.3 Multiple Current Filaments

The situation of multiple CFs becomes more complicate according to their thermal effect. The interaction of two CFs leads the different way to induce heat in the ESD device to the thermal breakdown temperature. Therefore the multiple CFs characteristics are necessary to understand and will be benefit to the chip designers.

At high I_S the size of multiple CFs (W_{CF}), CFs number (N), two CFs activities in DUT are examined from the induced phase change by the TIM techniques and the Dual Beams Michelson Interferometer method.

3.3.1 The dependence of filament numbers on stress current

The current instability within the Negative Differential Resistance regime can lead to the formation of multiple CFs. [89]-[90] 2D phase images of Figure 73 were taken at early time ($t_{IMAGE} \approx 30$ ns) in order to observe the amount of standing CFs at their triggering positions. The CFs number (N) varied from pulse to pulse depending on the current density in device; for instance, one could observe alternately both one CF and two CFs modes at a constant I_S . More CFs appeared when the NPN_Std device was applied with short pulse at higher currents; (a)-(b) $I_S = 0.9$ A, $N = 1$ and 2, (c)-(d) $I_S = 1.4$ A, $N = 2$ and 3, and (e)-(f) I_S

$= 2 \text{ A}$, $N = 3$ and 4 . In conclusion, the averaged N has the increase tendency with respect to the increase I_S . [80]

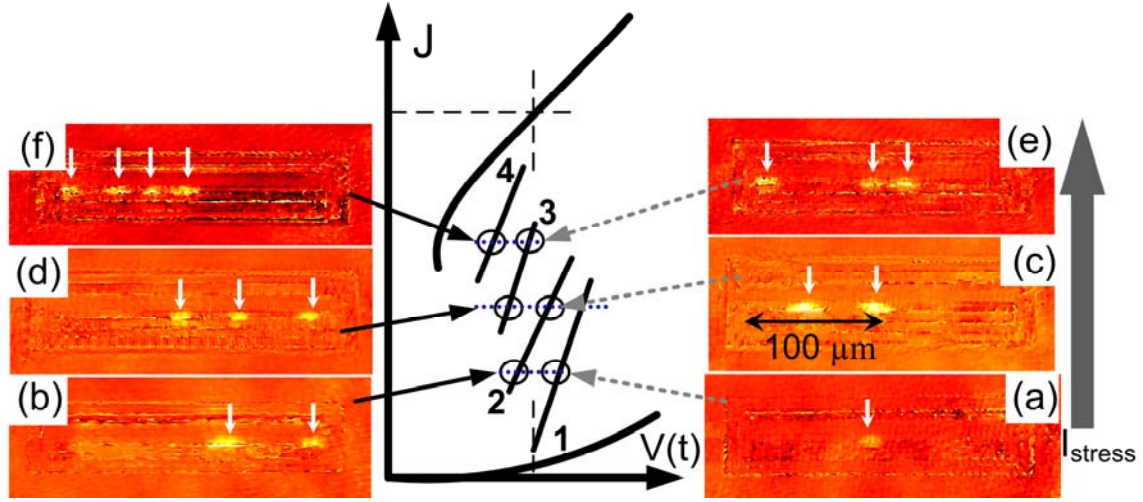


Figure 73 2D phase images at $t_{IMAGE} = 30 \text{ ns}$ present the averaged numbers of CF depend on stress current; (a)-(b) $I_S = 0.9 \text{ A}$, (c)-(d) $I_S = 1.4 \text{ A}$, and (e)-(f) $I_S = 2 \text{ A}$. [80]

3.3.2 Multiple current branches in IV characteristic

The IV characteristic of NPN_Std device in Figure 74 (a) consists of two CF branches. The 1st branch after the device triggering determined the holding voltage of one CF mode. Along the 2nd branch appearing from $I_S \geq 0.45 \text{ A}$ the holding voltage drops about $\Delta V \approx 1 \text{ V}$ and two CFs can be observed. The significant voltage drop of the leftmost current branches from $I_S \geq 0.55 \text{ A}$ determines the thermal breakdown voltage that will be discussed in the further chapter.

The simplified circuits of one CF and two CFs in Figure 74 (b) demonstrate the additional R_A in case of two CFs is connected in parallel with the circuit of one CF.

At constant I_S , the equally shared current ($I/2$) flows through both filament channels. Then the voltage drop across R_A in the resistive layer in two CFs mode can be expressed by the relations;

$$V(t) = V_{PN} + \frac{IR}{2} \quad [\text{eq-17}]$$

where V_{PN} is the voltage at the avalanche junction. The voltage difference (ΔV) of two CFs mode from one CF mode is stated by;

$$\Delta V = IR - \frac{IR}{2}$$

If the filaments number (N) varies, N parallel resistances R_A are considered for the system at a fixed I_S . The current (I/N) flows through each filament channel that leads more voltage

drop across resistance in N^+ BL as demonstrated by Figure 74 (c). In the N filaments mode, the device voltage drops from $V(t)$ of one CF mode by; [80]

$$\Delta V = IR - \frac{IR}{N} \quad [\text{eq-19}]$$

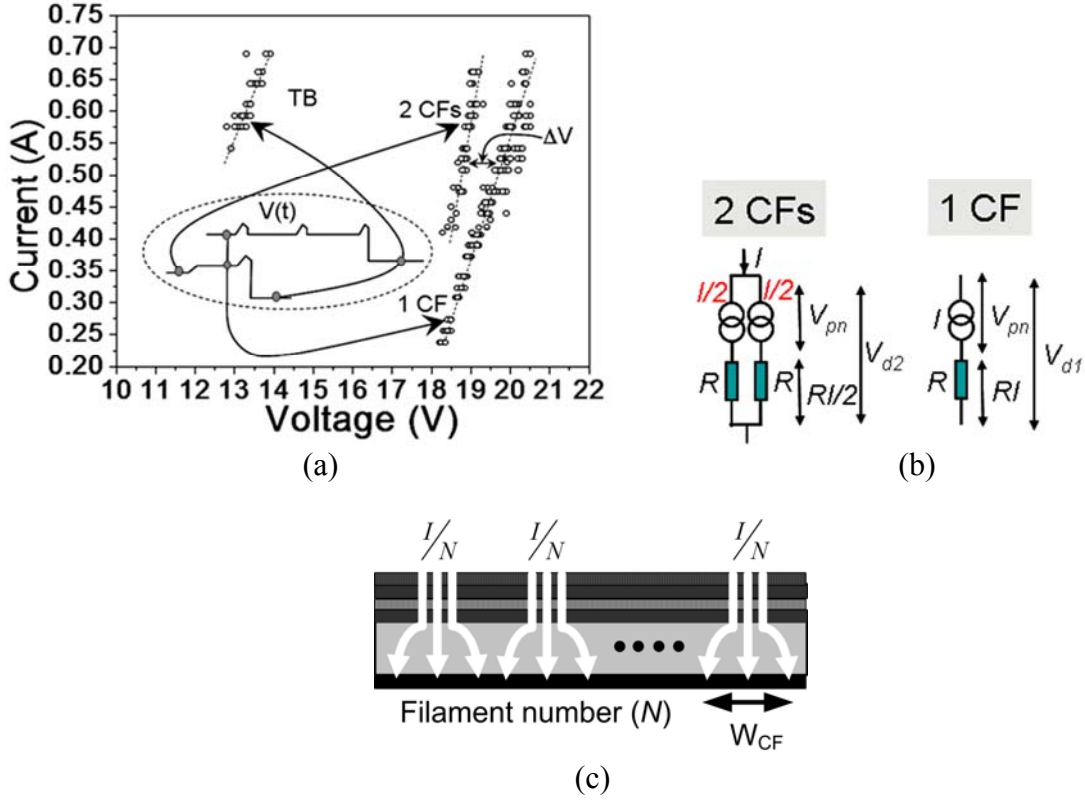


Figure 74 (a) IV characteristic of NPN_Std device consists of one CF and two CFs branches, and the thermal breakdown (TB) branch at high I_S . (b) The circuit schematics of one CF and two CFs modes. (c) The schematic of current sharing among multiple CFs (N is number of CFs). [80]

3.3.3 Size of Multiple Current Filaments

The size of multiple CFs (W_{CF}) was estimated from the hot spot sizes of 2D phase images induced by standing CFs. Figure 75 (a)-(e) were captured at the same $t_{IMAGE} = 30$ ns, after the NPN_Std device has been stressed with short pulse at high I_S . The W_{CF} sizes were calculated by taking the ratio between numbers of pixels and the actual dimension in μm -range as summarized in Table 8.

The size of filaments depends on the current I_S and the filament number (N). When I_S was increased, the averaged W_{CF} has been found to increase. At a fixed I_S , the averaged W_{CF} was observed to decrease in case of increasing CFs number (N). And the maximally observed size of W_{CF} is consistent with the distance L between N^+ Emitter edge and N^+ Sink edge ($L \approx 20 \mu\text{m}$).

I_S (A)	W_{CF}		
	$N = 2$	$N = 3$	$N = 4$
1.4	15-16.6 μm	12.7-13.4 μm	-
2	22-23 μm	16.9-18.6 μm	13.6-15.2 μm

Table 8 The overall size of multiple CFs increased with the increase I_S , but at the fixed currents the size W_{CF} decreased in more number of CFs mode.

The current density $\langle J \rangle$ depends on the filament number (N) and can vary from pulse to pulse at constant I_S as expressed by;

$$\langle J \rangle = \frac{I}{W_{CF1} + W_{CF2} + \dots + W_{CFN}} \approx \frac{I}{W_{CF} \times N} \quad [\text{eq-20}]$$

where W_{CF1} , W_{CF2} , and W_{CFN} are the width of each CF that are approximate likeness for the same CF mode. (The measured widths W_{CF} in each mode have insignificant difference.) Two hot spots in Figure 75 (c) appeared the highest temperature change ($\Delta\phi_{\text{MAX}}(x,y,t_{\text{IMAGE}})$) due to the maximum $\langle J \rangle$ in two CFs compared to three or four CFs at constant $I_S = 2$ A.

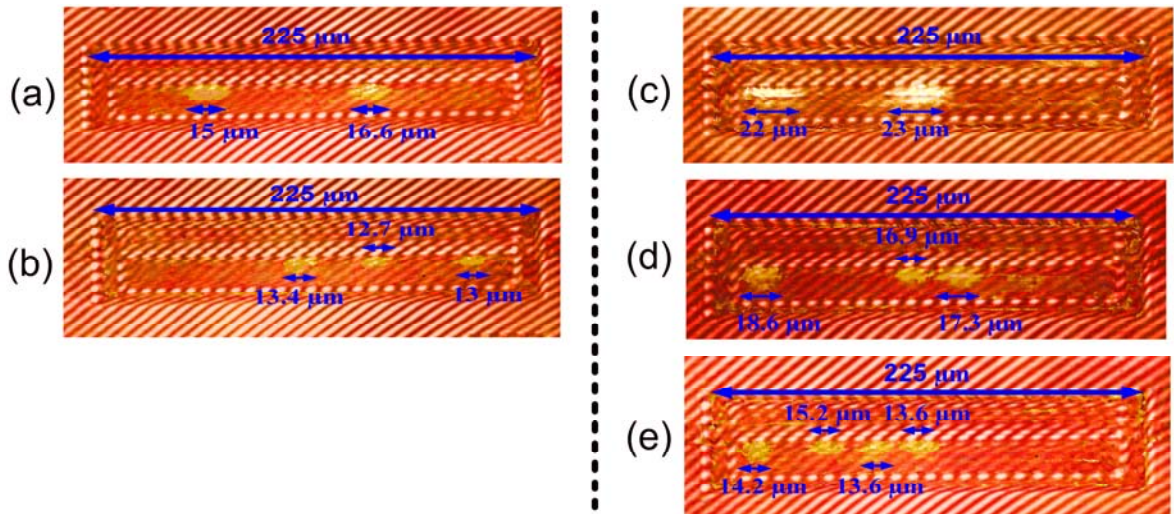


Figure 75 2D phase images of NPN_Std device observed at $t_{\text{IMAGE}} = 30$ ns present the size of multiple CFs at (a)-(b) $I_S = 1.4$ A and (c)-(e) $I_S = 2$ A.

3.3.4 Nondestructive interaction between two filaments

3.3.4.1 Meeting of two filaments by 2D TIM

Multiple CFs inevitably appeared in the investigated NPN devices; afterwards two CFs has to interact each other in the long pulse duration. The randomly generated CFs are expected to encounter each other. The 2D TIM at two time instants measurement was exploited to capture the 1st image of generated CFs and and the 2nd image of meeting CFs in linear and circular devices.

1) Two CFs meeting observed in the linear NPN_Std device:

The 2D phase image at the 1st imaging instant (Figure 76 (a) observed at $t_{IMAGE} = 360$ ns) and the phase evolution along the cross sectional line demonstrate two CFs heading toward one another. The phase evolution along the line within heated area at the 2nd imaging instant (Figure 76 (b) observed at $t_{IMAGE} = 420$ ns) shows the front walls of both CFs locate closely together, and the induced temperature remained highly in the entire passage.

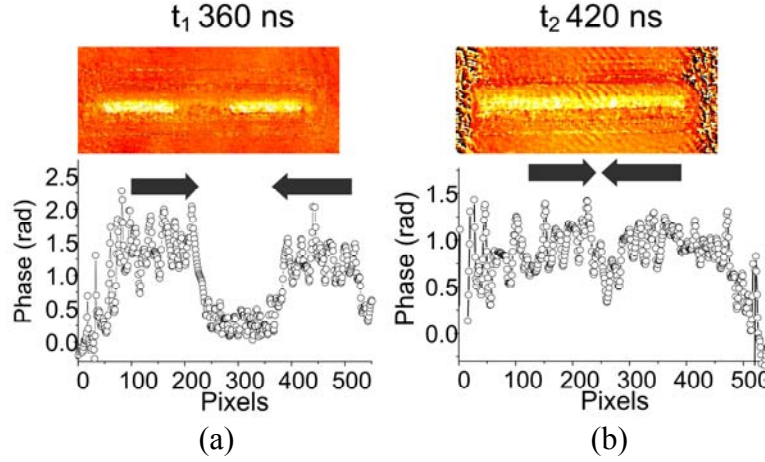


Figure 76 Extracted 2D phase images at the two time instants are captured at; (a) $t_{IMAGE} = 360$ ns (b) $t_{IMAGE} = 420$ ns.

2) Two CFs meeting observed in the circular NPN_Round2 device:

The circular device exhibited multiple CFs likewise as observed in the other structures, see Figure 77 (a) and (b). The 2D image (a) at the 1st imaging time ($t_{IMAGE} = 30$ ns) presents two CFs were standing at their initial positions, marked with S (circles). The 2D image (b) at the 2nd imaging time ($t_{IMAGE} \approx 60$ ns) presents the temperature change after two CFs had already interacted.

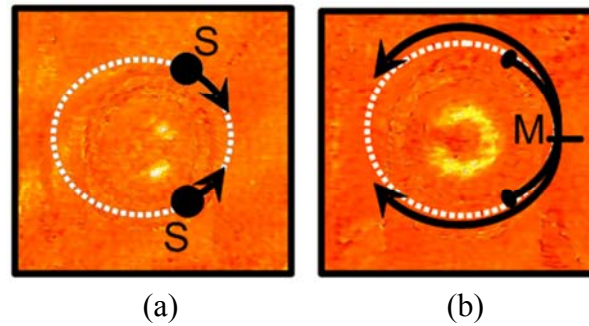


Figure 77 2D phase images at 2 time instants measurement was done at $I_s = 1.2$ A for observing the meeting of two filaments. (a) Two standing CFs at $t_{IMAGE} = 30$ ns (b) The meeting activity happened before the 2nd $t_{IMAGE} = 60$ ns; two circles indicate the starting CF positions and the arrows describe the moving direction.

The expansion of heated region indicates the meeting location was approximately at M. (The 2nd image was taken after CFs meeting.) Both ends of heated region correspond to

the existing CF locations at the 2nd imaging instant. Two arrows describe the motion of two filaments from the beginning until the 2nd imaging time.

3.3.4.2 Meeting of two filaments by Heterodyne Scanning TIM

The 2D phase images are insufficient for establishing the temperature distribution at the moment of CFs meeting. Therefore, the heterodyne scanning TIM technique was a suitable technique to investigate the temperature change at the encounter moment.

Few NPN_Meander devices stand a chance to exhibit the repetitive filamentary mode. Two CFs were always triggered from the same symmetrical locations at high I_S . The Heterodyne scanning TIM measurement was performed along the filament path along S1, S2,..., S6, S1.

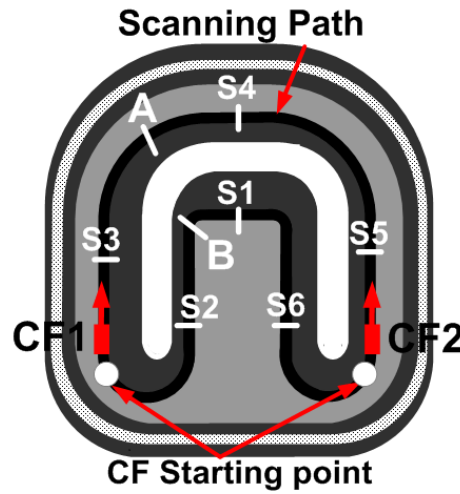


Figure 78 The NPN_Meander2 layout shows the TIM scanning movement starting from S1, S2,..., S6, until S1 along the emitter edge. Two circles indicate the repetitive starting positions of two CFs mode.

The scattered data of temperature distribution ($\Delta\phi(x,y,t)$) and phase derivative (P_{2D}) were plotted at the selected times t_0 - t_9 within stress duration of 500 ns, see Figure 79. Two symmetric envelopes happening at once indicates two CFs (CF1 and CF2) generated from the locations, marked in Figure 78. CF1 and CF2 were standing at initial position at time t_0 of 30 ns, and began localizing toward each other during time interval t_1 - t_2 . The P_{2D} at time interval t_3 - t_5 presented two CFs spending a short meeting time (t_{MEET}). From time interval t_6 - t_9 two joining CFs prefer to separate and travel individually further, but not to combine into one large CF. Motion of two CFs are illustrated with two dotted lines in the time evolution. The induced temperature before meeting ($t < t_3$) has remained on the meander passage to associate with the CF temperature (T_{CF}) after their meeting from $t > t_5$. The maximum induced phase ($\Delta\phi_{MAX}$) happened at the time t_6 that delayed from the meeting moment of P_{2D} envelopes at t_3 . This was probably influenced by the thermal inertia of heat capacity in the device bulk.

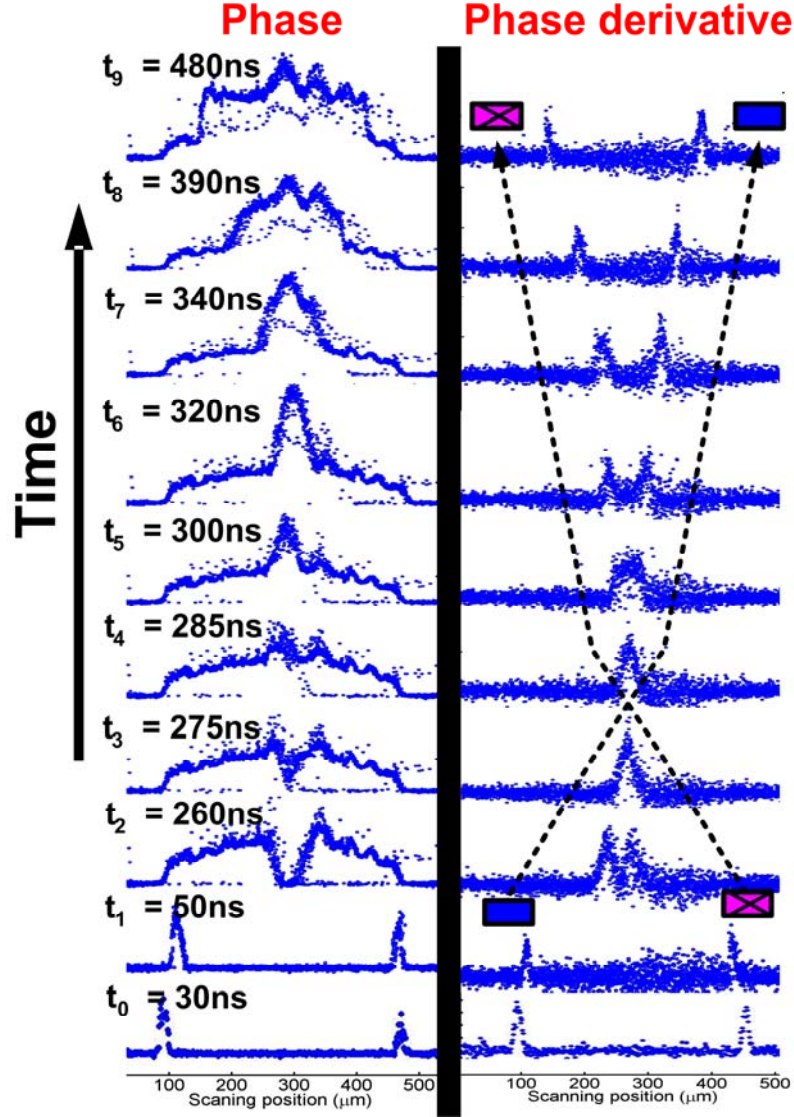


Figure 79 Phase distribution and phase derivative of NPN_Meander2 device were measured by the Heterodyne Scanning TIM technique at $I_S = 0.8 \text{ A}$ for 500 ns duration and plotted at various instants to demonstrate the meeting/passing of two CFs; t_0 : CFs are standing, t_1 - t_2 : CFs start traveling to each other, t_3 - t_5 : CFs are overlapping, and t_6 - t_9 : CFs travel separately again.

The phase evolutions of repetitive mode were observed at two positions; one was at the scanning point A and another was at the meeting point $S4$, see points A and $S4$ in Figure 78 and phases in Figure 80 (a). The phase at meeting point $S4$ increased once at time 275 ns ($\approx t_3$) and the V_{PEAK} appeared simultaneously. The overlapping of CF temperature ($2T_{CF}$) during meeting led to the locally high temperature at meeting positions at the same moment of V_{PEAK} occurrence. Each CF spent time t_A to travel on distance between positions A and $S4$. Time t_B was the time to travel the same distance between two positions including the meeting time (t_{MEET}) that could be estimated by;

$$t_{MEET} = t_B - t_A \approx 30 \text{ ns}$$

Maximum phase amplitude ($\Delta\phi_{MAX} \approx 5$ Rad) relating to the superimposing temperature of two joining CFs ($2T_{CF}$) had about double magnitude of induced phase ($\Delta\phi \approx 2$ Rad) by individual CF (T_{CF}). Meander allowed CF to travel without turning around DE, so the occurrence of V_{PEAK} was a result of two CFs encountered during moving.

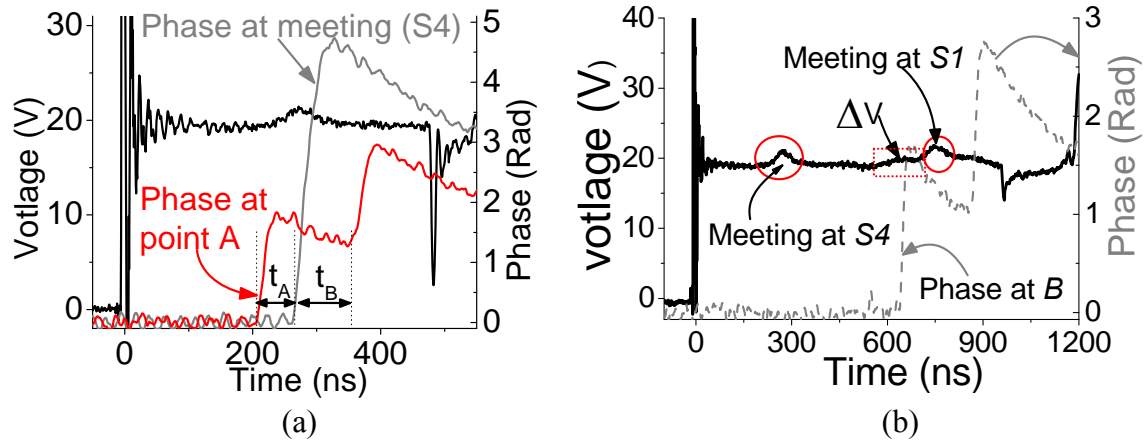


Figure 80 (a) The voltage and phases were plotted together to demonstrate the induced temperature by two meeting filaments at point A and S4 (referred to Figure 78) at $I_S = 0.8$ A (b) The second V_{PEAK} of longer pulse was observed in the waveform of long stress pulse due to the second meeting at position S1.

Once the pulse duration was extended from 500 ns to 1 μ s, the voltage waveform of Figure 80 (b) was plotted with the phase evolution of position B in Figure 78. The second V_{PEAK} (at $t \approx 715$ ns) and the rising phase of position B presented the 2nd meeting time that approximately happened at position S1. The small voltage increase (ΔV) had been affected by CF moving through the region of higher access resistance R_A .

Here should be summarized that the voltage peak (V_{PEAK}) signals the current redistribution during meeting of two CFs in all device structures; nevertheless, it indicates a single CF turnabout DE of linear structure.

3.3.4.3 Splitting of two filaments by 2D TIM

The repetitive behavior of two CFs found in the NPN_Meander device was captured by the 2D TIM techniques at interesting instants t_1 - t_4 , see Figure 81. CF with the high current density at $I_S = 0.8$ A had tendency to split into two CFs before moving. Two CFs sharing equal power moved along the meander fingers to meet each other at the device middle as presented by the last image (at t_4). (Remark: the repetitive initial CFs positions in meander structure could be observed at different locations from device to device.)

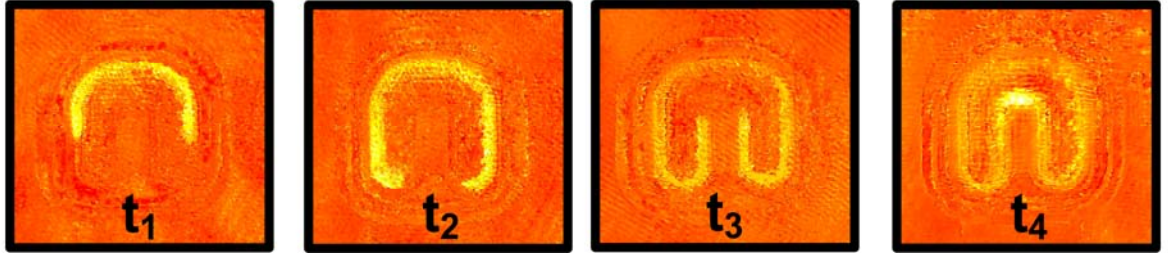


Figure 81 2D Phase images of meander device at four time instants ($t_1 - t_4$) demonstrate splitting of CF filaments at the beginning of pulse at $I_S = 0.8$ A. Two CFs moved symmetrically along the meander fingers until joining.

3.3.4.4 Splitting of two filaments observed by Dual Beam Michelson Interferometry

The Dual beam Michelson Interferometer was exploited to investigate the CFs activity after meeting by sensing the temperature change at two separated positions. Dual beams were separately focused on the linear passage with spacing distance of $55\ \mu\text{m}$, see the infrared image of Figure 82 (a). Two CFs were generated at $I_S = 0.5$ A, and the phase evolution and voltage change in Figure 82 (c) determine the motions of two CFs as illustrated by Figure 82 (b).

The 1st rising of both transient appeared when CFs leaving from both DE passed by two focusing beam. The apparent V_{PEAK} was evidence of two filaments meeting at a position (M) locating between two focusing beams. The 2nd rising phases of both signals prove two split CFs passing by after meeting.

This measurement presents that not only indicated the voltage peak (V_{PEAK}) CF turnabout DE of linear device, but it also could signal the meeting of two moving CFs for $I_S \geq 0.45$ A.

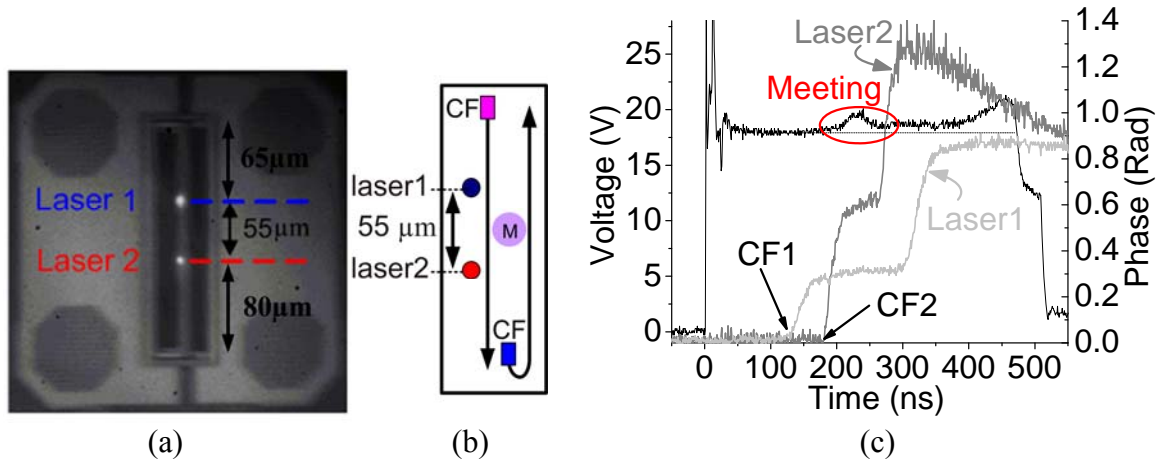


Figure 82 (a) Infrared image of NPN_Std device (b) The moving schematic of two meeting (M) CFs at the device center (c) A small voltage peak occurred when two CFs met at the device center, not relates to CF turnabout DE.

3.3.4.5 Modified TLP setup for observing the splitting of CF

The investigation of splitting CF in the next sub-chapter exploited the modified TLP setup for generating the step-up current pulse as in Figure 83 (b). The current change within one duration could be achieved by modifying the standard TLP system (Figure 31) by adding an extra transmission cable. From the standard TLP setup, the attenuator was connected to one opened-terminal of the transmission cable for avoiding the undesired reflection voltage, see Figure 83 (a). An additional transmission cable (the right cable of drawing) was required for generating the delay time in the reflected pulse (τ_{delay}).

From the reference [59], the stress pulse duration (τ) is equal to the time of wave propagation in forward and backward through a transmission cable. The pulse duration (τ) is determined from the length of transmission cable mentioned in the equation [eq-2]. The delay time (τ_{delay}) in voltage schematic of Figure 83 (b) is likewise defined from the length of additional cable, in which 1 meter length of delayed cable provides 5 ns of the delay time. The $V(t)$ pulse begins with low voltage V_1 controlled by the resistance R_1 ($V_1 = IR_1$), and then the amplitude increases to higher voltage V_2 determined from the relation of $V_2 = \frac{R_1}{R_2} V_1$. For instance, the $I(t)$ waveform of Figure 84 (b) was generated by two dedicated resistances with the relation of $R_1 = 3R_2$.

After the end of duration ($t > \tau$), the unwanted voltage with amplitude of $V_2 - V_1$ appeared for the period of τ_{delay} because the voltage reflection still existed in the delay cable. If the τ_{delay} was long, this unnecessary stressing would possibly degrade the investigated device. Therefore, the resistances and transmission cable length should be selected carefully.

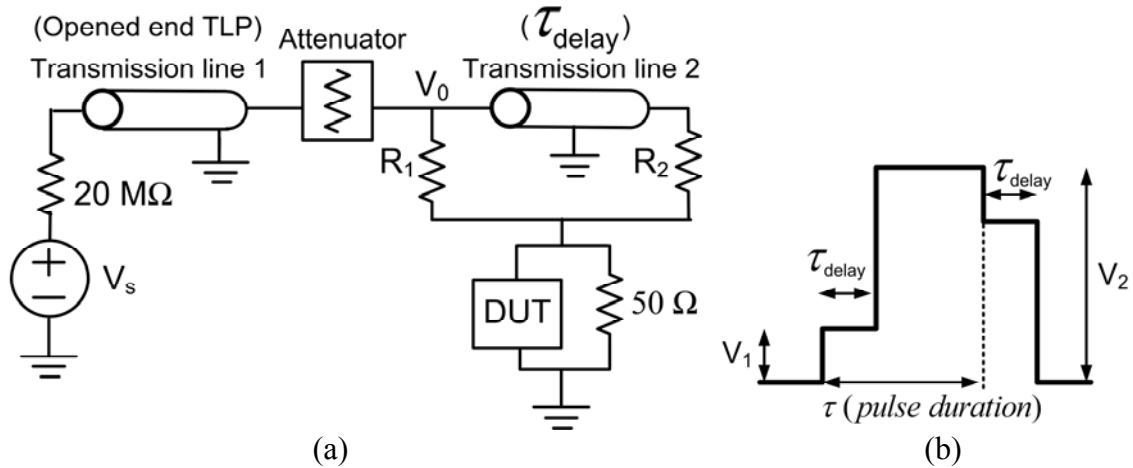


Figure 83 (a) The modified schematic of TLP pulser for the step-up voltage generation. The step-up in voltage was accomplished by adding another cable to the standard TLP. (b) The voltage magnitude could be determined from the resistance R_1 and R_2 and the stressing period was controlled by the length of transmission cable.

3.3.4.6 Controlled splitting of a CF

The splitting activity always happen after CFs meeting at high I_S that is relevant to the high $\langle J \rangle$ in W_{CF} . One could make an assumption that the stability of two narrow CFs was probably higher than one large CFs at a considered I_S . This study shows a moving CF was split into two CFs, when the current density inside CF was abruptly increased.

In order to generate the abruptly increased current pulse, the conventional TLP set-up was modified by adding a delayed transmission cable to the system (The circuit schematic of modified setup will be discussed further). And the 600 μm NPN_Dope device (see Figure 45) was stressed with the step-up current pulse that increased rapidly from low current ($I_1 \approx 0.5$ A) to high current ($I_2 = 1.5$ A) within one duration. Single CF was repetitiously triggered from the middle of device under stressing with the identical waveforms of Figure 84 (b).

The 2D phase image at t_1 (see Figure 84 (a)) has low $\Delta\phi$ induced by a small power of CF at I_1 , and the image at t_2 present a locally high $\Delta\phi$ at the leftmost area of heated area that corresponded to the increasing $\langle J \rangle$ from I_1 to I_2 . The high $\Delta\phi$ in 2D images at t_3 and t_4 expanded laterally toward both DE induced by two split CFs.

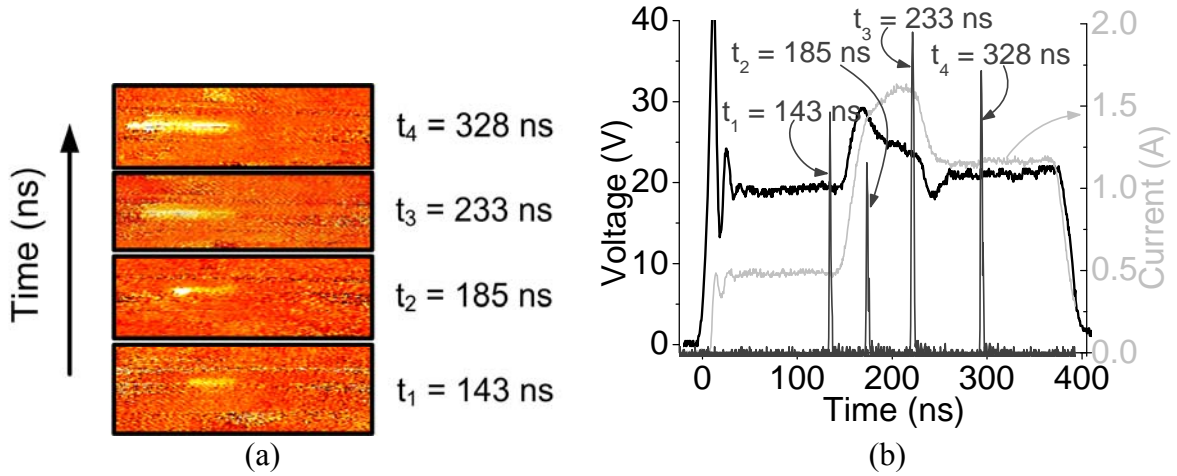


Figure 84 (a) The 2D phase images of 600 μm NPN_Dope device are captured at four time instants t_1 - t_4 . CF was triggered from the device center and traveled within the left half of W_D at current $I_1 = 0.5$ A and intended to split into two CFs after increasing current to $I_2 = 1.5$ A. (b) IV waveforms under stressing with the step-up pulser are marked with four imaging instants.

The CF power and the induced temperature along width (y-direction) associating with 2D phase images of Figure 84 (a) are illustrated by Figure 85 (a). The higher $\langle J \rangle$ in CF at t_2 suddenly increased three times larger than the $\langle J \rangle$ at t_1 . The asymmetrical phase envelope indicates the high temperature gradient between left and right walls of heated region. The power of split CF at t_3 ($I_S \approx 1.2$ A) was smaller than CF power at t_2 ($I_S \approx 1.5$ A) but was greater than CF power at t_1 ($I_S \approx 0.5$ A). The $\Delta\phi(x,y)$ profile at t_3 and t_4 presented the higher temperature at the right passage of splitting point, where was induced by CF with small power at $I_S = 0.5$ A.

2D image of Figure 85 (b) taken after splitting ($t_{\text{IMAGE}} > t_2$) presents the splitting CF activity appearing within the right half of W_D . The temperature evolution along the heated region presents CF1 and CF2 traveling a short distance. CF2 traveled backward through the preheated passage as the highly induced phase (the artifact) appeared.

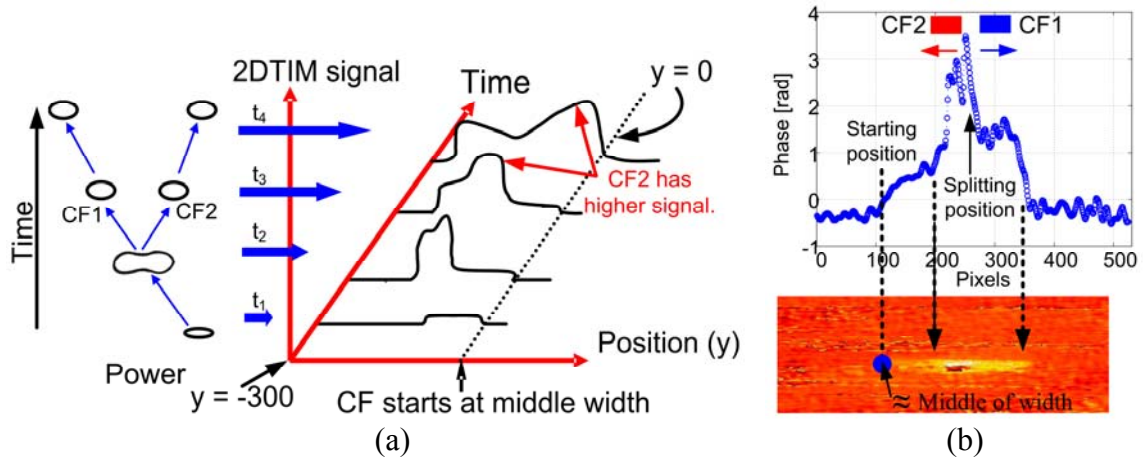


Figure 85 (a) The temperature evolutions and power densities of device under stressing with the step-up current pulse are illustrated in time evolution. (b) The temperature profile confirms two split CFs departing their splitting position at $t_{\text{IMAGE}} \approx 230$ ns.

3.3.5 Comparison of single CF with two CFs

Single CF and two CFs modes were alternately observed from the linear NPN devices from pulse to pulse at constant I_S . Two slanted filamentary branches in IV characteristic of Figure 74 (a) have different holding voltages from $I_S \geq \approx 0.45$ A. The device exhibited one CF mode for about 13 percent of total stressing pulses and two CFs mode for the rest of percentage. [80]

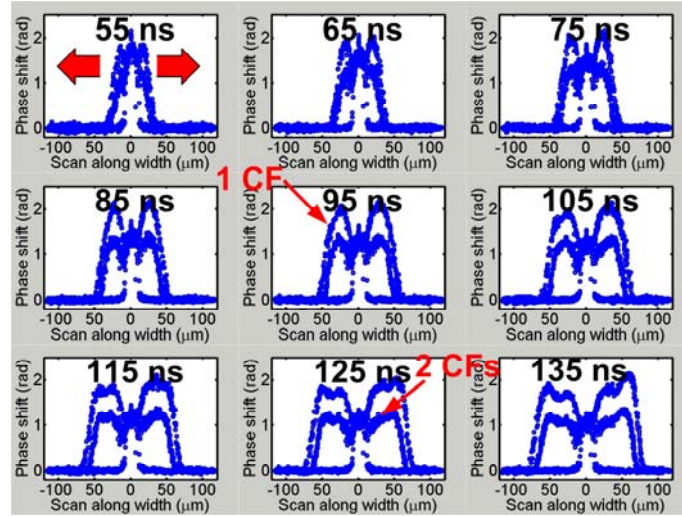


Figure 86 The phase distributions by the Heterodyne scanning TIM method of NPN_Dope device were alternately induced by one CF and two CFs from pulse to pulse at $I_S = 0.6$ A. Each scanning point the device was stressed with 10 pulses.

The comparison between two filamentary modes in the NPN_Dope device (see Figure 45) had been investigated at $I_S = 0.6$ A by the Heterodyne scanning TIM method.

One CF or two CFs were always triggered from the middle W_D ($y = 0 \mu\text{m}$) where has locally low base resistance (R_B). The scattered plot of phase distribution ($\Delta\phi$) along W_D of $200 \mu\text{m}$ during time interval of $55 \text{ ns} \leq t \leq 135 \text{ ns}$ have two magnitude levels. The low $\Delta\phi$ was induced by two CFs sharing the same power, and the high $\Delta\phi$ related to the temperature induced by single CF mode. ($\Delta\phi$ magnitude of 1CF mode was approximately double of two CFs mode) Two CFs mode has more density of scattered data plots than one CF according to two generated CFs traveled simultaneously toward both DEs, but one CF existed at once.

Voltage waveforms of 1CF and 2CFs modes corresponding to the result of scanning TIM measurement in Figure 86 are compared in Figure 87 (a). The voltage difference ($\Delta V \approx 1\text{V}$) allows us to distinguish between $V(t)$ waveforms of 1CF and 2CFs ($V_{H1CF} > V_{H2CF}$). The compared phase derivatives (P_{2D}) of two filamentary modes in Figure 87 (b) had the equivalent temperature gradient at front wall (T_{FRONT}). This determined that either 1CF or 2CFs approximately move at the nearly same speed V_{CF} , even though each of 2CFs had about half a power.

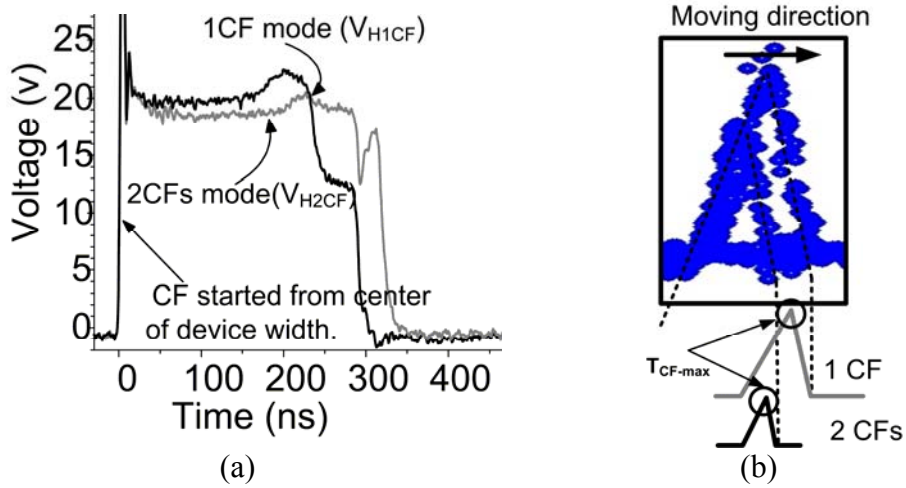


Figure 87 (a) Two $V(t)$ waveforms of 1CF and 2CFs mode are compared at $I_S = 0.6 \text{ A}$ showing the voltage difference ($\Delta V \approx 1\text{V}$). (b) The powers of two filamentary modes are compared indicating the same temperature gradient of both modes.

3.4 Thermal breakdown

The thermal breakdown (TB) or the second breakdown is a thermally activated mechanism that was observed in all listed devices of Table 5. The TB event notifies from a significant voltage drop in IV characteristic. In Figure 88 (a), IV characteristics of NPN_Std device were averaged over voltages in two time intervals of 10 ns within pulse duration (τ) of 500 ns; the former interval was at the early period of pulse (see solid squares) and the latter interval was close to the end of pulse (see opened circles).

The TB event would not be observed (in IV characteristic that averaged over early interval of 100-110 ns), if the device was stress with a short pulse ($\tau \leq 100 \text{ ns}$) at the room temperature. And the device would only exhibit the TB since $I_S \geq 0.5 \text{ A}$. Therefore τ and I_S are important parameters leading device to exhibit the TB. In all experiments, the leakage

current (I_{LEAK}) was always checked after each stress current to determine its functioning (see the cross signs).

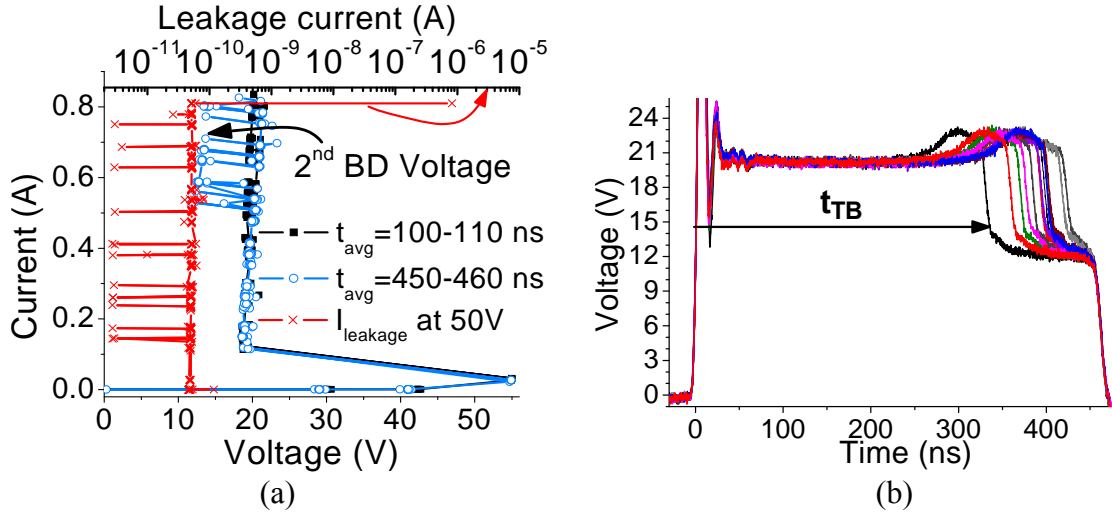


Figure 88 (a) IV characteristics of NPN_Std device under stressing with 500 ns TLP pulses were averaged over two selected time intervals; TB presented at the interval of 450-460 ns and the device failed at $I_{FAIL} = 0.8$ A. (b) $V(t)$ waveforms observed at $I_S = 0.54$ A have different times to BD (t_{TB}) due to the difference in traveling time from the random triggering CF position to the 1st DE.

The steep TB branch in IV characteristic of Figure 74 (a) appeared from $I_S \geq 0.54$ A, while 1CF and 2CFs branches have appeared early from lower I_S . The heat induced by one or two filaments had different temperature degree from pulse to pulse causing the device to exhibit the second thermal breakdown at different time instants that will be elucidated in following topics.

3.4.1 Thermal breakdown of Single Current Filament mode

The device will exhibit TB, when the device temperature reaches the critical value (T_{CRIT}). The voltage waveforms of linear NPN_Std device in Figure 88 (b) at $I_S = 0.54$ A show the different times to TB (t_{TB}) from pulse to pulse. The times t_{TB} are defined by the traveling time from the random triggering position to the first arrival at DE. Several parameters including I_S , τ , W_D , and the initial CF position determine the different t_{TB} . Another important factor leading to TB is the temperature change existing in CF passage during stressing.

3.4.1.1 Effect of preheated passage on the thermal breakdown event

In the linear geometry devices, the device usually exhibits the TB at the moment of CF turnabout DE, where the temperature at DE reaches a critical temperature (T_{CRIT}). The 200 μ m NPN_Std device was stressed with long pulse at low current (i.e. $\tau \geq 400$ ns and I_S

≤ 0.3 A) and the temperature has not reached the T_{CRIT} at the first visiting time on DE. CF could continue traveling further through the preheated passage induced by CF of the previous passage.

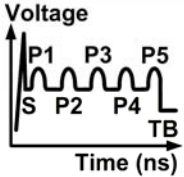
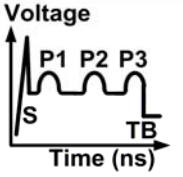
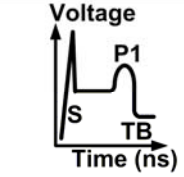
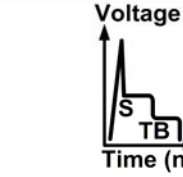
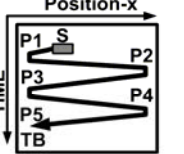
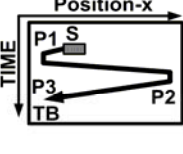
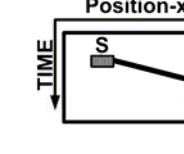
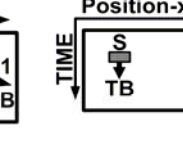
Motions of 1CF and voltage waveforms of four thermal breakdown modes were observed at varied τ and I_S , summarized in Table 9. All notations the 1st and 2nd rows are the same and are indicated in time; S = Starting CF position, P1, P2,...,P5 = Voltage peak related to CF passage at the device ends, TB = Thermal breakdown

Mode A: CF could leave twice from the same DE (P1 and P3), but TB occurred later when CF reached that DE at the third time (P5). The induced temperature at DE has accumulated from two previous visitings and would superimpose with T_{CF} during the 3rd visit.

Mode B: TB happened at the moment when CF reached the same DE at the 2nd time (P3). The temperature at DE induced by CF at the 1st visit has been lasting for the 2nd visit.

Mode C: TB occurred when CF arrived DE at the first time (P1). The temperature at DE reaches T_{CRIT} at the first arrival. And the t_{TB} is specified by the distance (y) between starting CF position to the closest DE and V_{CF} . ($t_{TB} = \frac{y(S) - y(P1)}{V_{CF}}$)

Mode D: TB occurred during the CF was standing at the initial position according to the temperature in the standing CF increased and reached T_{CRIT} before traveling.

Mode	Mode A	Mode B	Mode C	Mode D
$V(t)$				
Position vs Time				
I	< 0.3 A	0.3-0.5 A	> 0.5 A	$>> 0.53$ A
$<t_{TB}>$	$<t_{TB,C}> + 2 \times t_{turn}$	$<t_{TB,C}> + t_{turn}$	$<t_{TB,C}> \leq t_{turn} / 2$ $= W/v_F$	< 100 ns
Remark	Observed at room temperatures	Observed at room and elevated temperatures	Observed at room and elevated temperatures	Observed at elevated temperatures

Legend S – starting position of a current filament; P – voltage peak related to current filament passage at the device ends; TB - thermal breakdown. The same notation is indicated in time - position graphs in the second row;

Table 9 Summary of thermal breakdown modes in the 200 μ m NPN_Std device induced by single CF. The $V(t)$ waveforms and CF movement in space-time are illustrated with simplified schematics. (t_{TURN} is the time to complete a roundtrip.) [86]

The temperature change (ΔT) along the linear passage induced by CF was low at low I_S in *Mode A*; therefore, the temperature at DE induced by two previous visitings has been accumulated. The background temperature was laid over by the CF temperature (T_{CF}) that can be expressed by;

$$T_{DE} = \Delta T(I_S, t_{TB}) + T_{CF}(I_S) \quad [\text{eq-21}]$$

Higher power of CF raised more the temperature along passage. The temperature at DE could reach the T_{CRIT} at the earlier time. Therefore the t_{TB} of *Mode B* and *Mode C* were shorted by t_{TURN} and $2 \times t_{TURN}$ from t_{TB} of *Mode A*, respectively. In case of very high I_S and high ambient temperature (T_{AMB}), the temperature gradient inside CF superimposed with the high T_{AMB} reaching the T_{CRIT} when CF was standing at the initial position described by the relation;

$$T_{CF} + T_{AMB} \geq T_{CRIT}$$

3.4.1.2 Effect of different widths on the thermal breakdown in linear structure

The accumulated heat at DE gradually diffuses with respect to time. At the return moment of CF to preheated DE, the temperature at DE was lower in larger device widths due to heat can diffuse more for a longer return time, see the compared waveforms of Figure 89 (a). Four NPN_Std devices with different W_D were observed at the minimal TB currents (I_{BD}) that the $V(t)$ waveform of *Mode A* initially transformed to $V(t)$ waveform of *Mode B*, so called the transition current $I_{A \rightarrow B}$. The TB event in waveforms of larger W_D would be observed at the higher $I_{A \rightarrow B}$, see Figure 89 (b). The relation between $I_{A \rightarrow B}$ and four W_D (100, 200, 300, and 400 μm) were measured twice showing the consistent results for identical devices on the same chip.

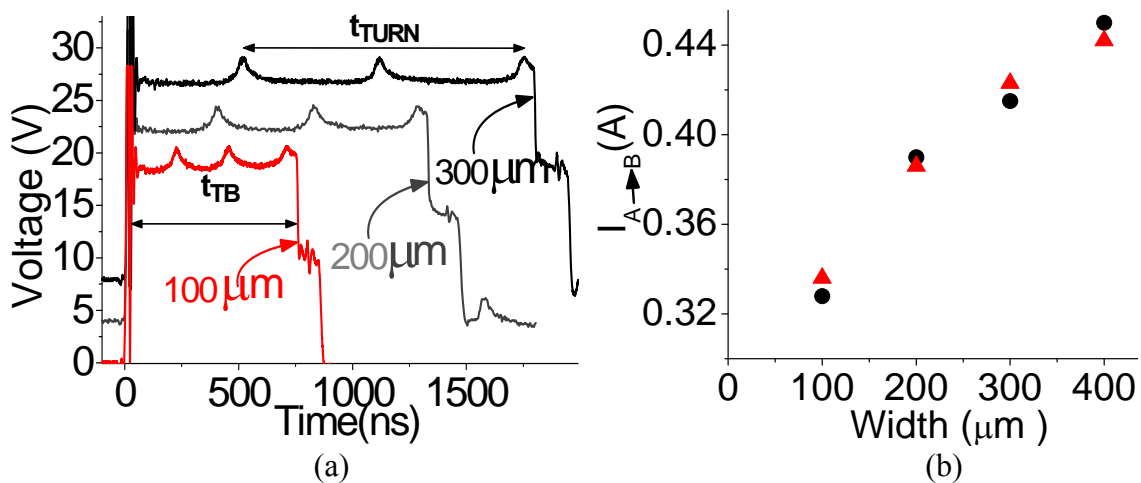


Figure 89 (a) The overflow plots of $V(t)$ waveforms of *Mode B* presents the longer times t_{TB} in the larger device. (b) The transition current from *Mode A* to *Mode B* of Table 9 increases in the larger device widths. Two NPN_Std devices were repeatedly observed showing the consistent results. [86]

3.4.2 Thermal breakdown of Two Current Filaments mode

Multiple CFs are inevitably generated at a higher I_S and the TB induced by multiple CFs happens whenever the device temperature reaches T_{CRIT} . The time t_{BD} varied from pulse to pulse according to random initial positions of two CFs at $I_S = 0.63$ A, see Figure 90 (a). In comparison to single CF mode, an early t_{TB} could be observed from a lower current ($I_S \geq 0.47$ A). [80]

The temperature would reach the T_{CRIT} at the first visiting time of single CF on DE from $I_S \geq 0.53$ A (see *Mode C* in Table 9). Nevertheless, waveforms *I* and *II* of Figure 90 (b) are two primary filamentary modes observed at a lower $I_S = 0.47$ A.

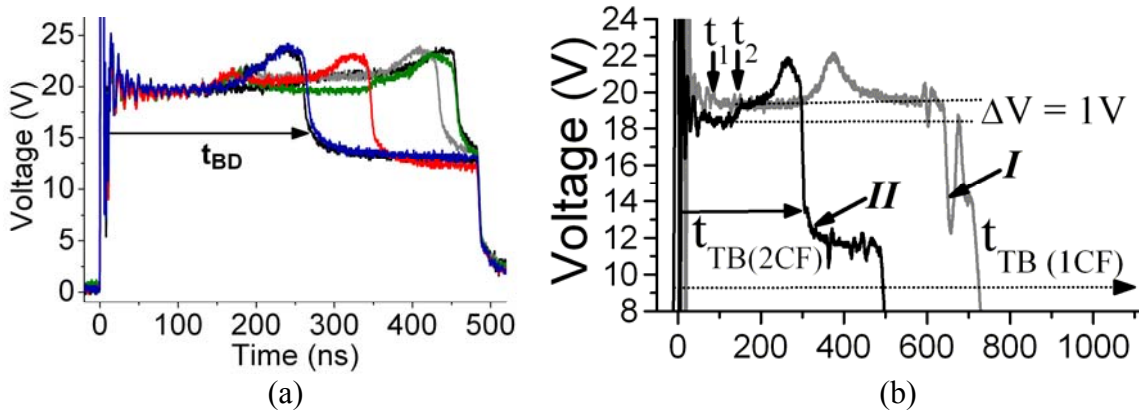


Figure 90 (a) $V(t)$ waveforms of two CFs mode in the NPN_Std device at $I_S = 0.63$ A have different times t_{BD} from pulse to pulse. (b) Waveforms of 2CFs and 1CF are compared; the early t_{TB} was observed only in two CFs mode at the same $I_S = 0.47$ A. [80]

Waveform *I* denoted that the TB did not happen at the 1st visiting of 1CF on DE; but the TB happened when CF visited at the 2nd time on the same DE at this I_S , as appeared in *Mode B* of Table 9. The expected t_{TB} of waveform *I* was longer than the stressing duration. But the shortened time t_{TB} in waveform *II* was observed at the same I_S from pulse to pulse. The voltage waveform *II* at t_1 dropped from voltage at t_2 by $\Delta V = 1$ V, which was equivalent to the voltage difference (ΔV) between IV branches in Figure 74 (a). The early t_{TB} of this mode has been investigated further by the 2D TIM and the Heterodyne scanning TIM techniques.

3.4.2.1 The early thermal breakdown of two CFs in linear device observed by 2D TIM technique

The NPN_Std device would not exhibit the thermal breakdown at the first arrival of 1CF on DE at $I_S = 0.5$ A (see *Mode C* in Table 9); however, the early TB was possibly observed in few waveforms at the same I_S as shown in Figure 91 (b). The voltage step ($\Delta V \approx$

1 V) is always accompanied with the shortened time to thermal breakdown ($t_{TB} = 300-325$ ns). The CFs activities concerning the voltage step were visualized by the 2D TIM images at two time instants, see Figure 91 (a) (1) and (2).

Two hot spots in the 1st 2D phase image ($t_{IMAGE} = 70$ ns) demonstrated CF1 and CF2 were taking the first step to move. The 2nd phase image was taken after t_{TB} ($t_{IMAGE} > t_{TB}$) and the maximum phase change ($\Delta\phi(x,y, t_{IMAGE} = 430$ ns)) appeared strongly on the left DE indicating the CF had been standing on DE after the thermal breakdown event. The gradually faded $\Delta\phi(x,y, t_{IMAGE})$ could be an evidence that CF1 probably disappeared from DE, see the schematic of CFs motion in Figure 91 (a) (3).

The Dual beams Michelson Interferometer was required to measure the induced temperature change along the CF passage in order to verify the CF vanishing from DE.

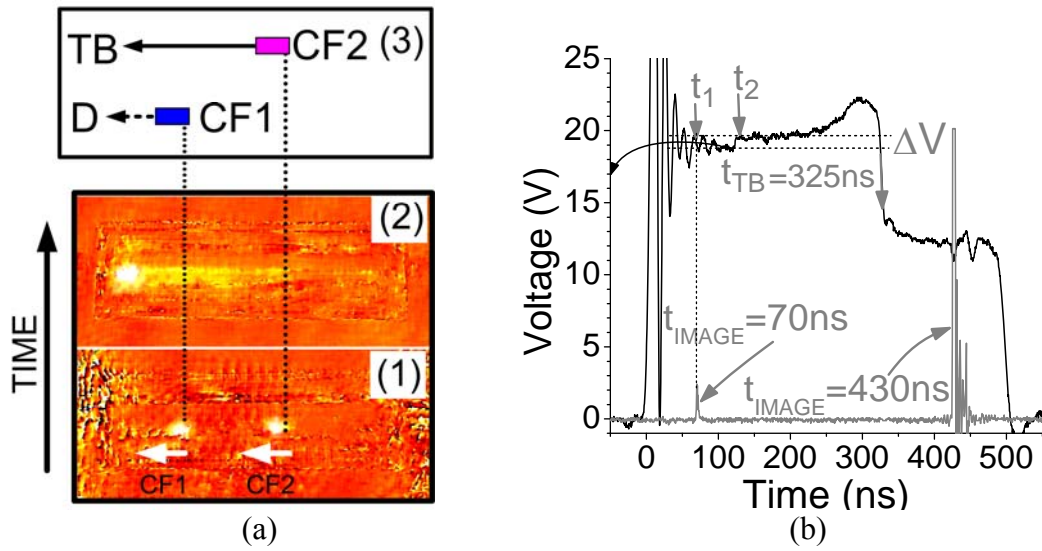


Figure 91 (a) 2D Phase images at two time instants were investigated in the 200 μ m NPN_Std device at $I_S = 0.5$ A; (1) $t_{IMAGE} = 70$ ns (2) $t_{IMAGE} = 430$ ns (3) Schematic demonstrated CF1 disappeared firstly from left DE and CF2 was following behind to travel toward the same DE. (b) The presence of early t_{BD} in $V(t)$ waveform always appeared in company with small voltage step (ΔV). [80]

3.4.2.2 The early thermal breakdown as a result of CF disappeared on DE observed by the Dual Beams Michelson Interferometer technique

The activities of two CFs concerning the early TB ($I_S \geq 0.45$ A) at shortened time t_{TB} cannot be elucidated with 2D TIM technique; therefore, the Dual Beams Michelson Interferometer was exploited to probe the temperature evolution induced by CFs.

The schematic (a) in Figure 92 shows *Beam2* and *Beam1* were focused at distances ≈ 20 μ m and ≈ 120 μ m far from the left DE of the 200 μ m NPN_Std device. The $V(t)$ waveform at $I_S = 0.5$ A presented the voltage step (ΔV) at time t_D (see Figure 92 (b)). Two focusing beams have the phase evolutions as followed;

Beam1: The normalized phase evolution in Figure 92 (c) presented that CF1 passed by Beam1 at time t_1 . CF2 traveling behind CF1 moved past Beam1 at later time t_2 . The 1st and 2nd rising phase amplitudes have the proximate value, which was a sign of sharing equal power among CF1 and CF2.

Beam2: The normalized phase evolution in Figure 92 (d) indicated that CF1 passed by Beam2 at time $t_1 + t_3$; in which, it spent time t_3 on distance between two beams. ($t_1 + t_3$ is unexpectedly equal to t_2) During the intervening times ($t_2 < t < t_2 + t_3$) two important aspects should be pointed out; one was the appearance of voltage step (ΔV) at time t_D and another was the signal disappearance from Beam2 that CF1 should induce at the return time $t_2 + 2 \times t_4$. (Factor 2 means the travel in forward and backward directions, and $2t_4$ includes the $t_{DE} \approx 30$ ns) This proved that CF1 definitely disappeared from the left DE, that corresponded to the device voltage changing from 2CFs mode to 1CF mode, see waveform in Figure ($V(t_1) \rightarrow V(t_2)$). The disappearance of CF1 yields the total I_S flows to the existing CF2 as the current sharing between two CFs collapsed into one CF.

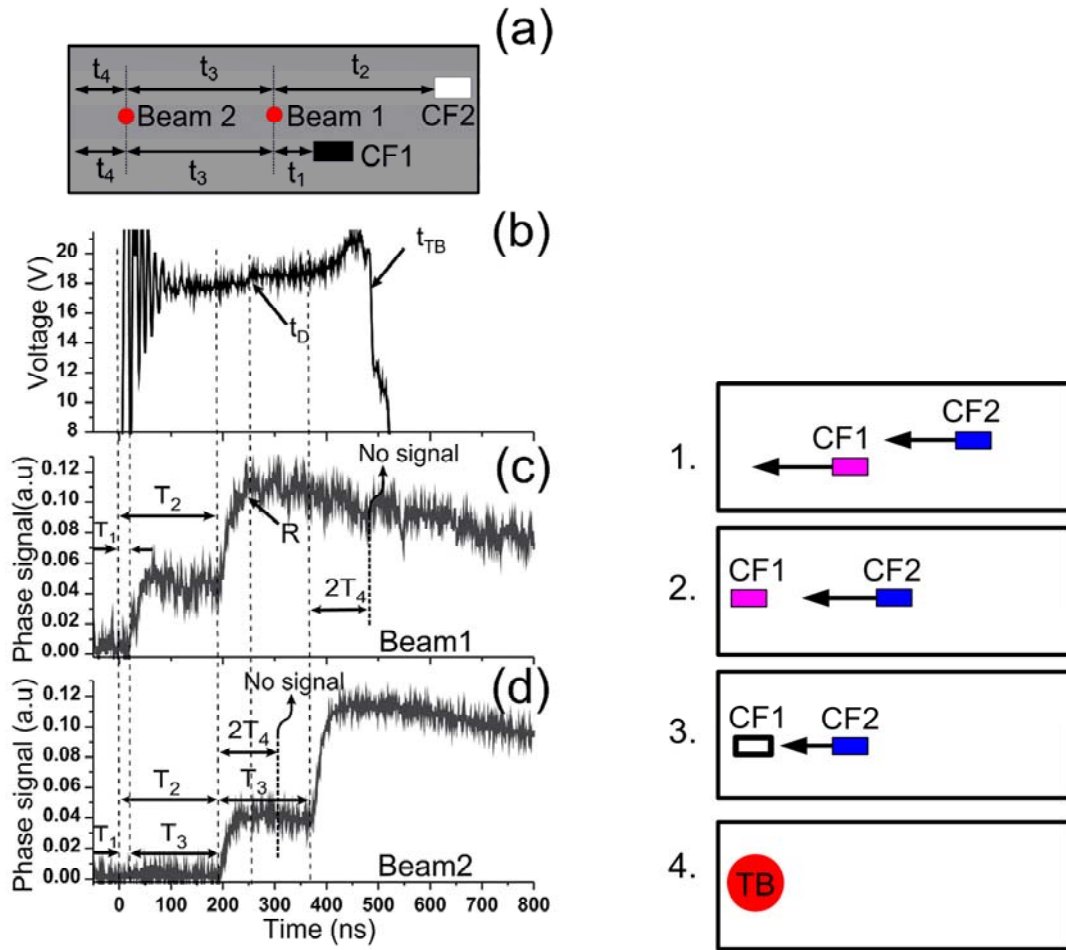


Figure 92 (a) The schematic shows the positions of Beam1, Beam2 and the initial positions of two filaments (CF1 and CF2); The distance between dual beams is $\approx 100 \mu\text{m}$ and the distance between left DE and Beam2 is $\approx 20 \mu\text{m}$. (b) $V(t)$ waveform having voltage step at t_D was measured at $I_S = 0.5$ A. (c) Phase evolution of Beam1. (d) Phase evolution of Beam2. Schematics 1-4 were interpreted from the phase evolutions (c), (d), and $V(t)$ waveform. [80]

The 2nd rising phase at $t_2 + t_3$ of *Beam2* was induced by CF2 that was traveling toward the same DE. The temperature on DE induced by the disappeared CF1 had been lasting until the arrival of CF2 at the later time. Eventually the device exhibited the TB at the arrival moment of CF2 on the preheated DE. The summary of CFs activities in this case was illustrated with the right schematics 1-4 in Figure 92.

The background temperature at DE had decreased incessantly from $t > t_D$ and would be superimposed with the temperature of CF2 that imparted the total current. The CFs activities raised the DE temperature to reach the T_{CRIT} at t_{TB} as the followed relation;

$$T_{CF2}(I_S) + T_{DE-CF1}(t, \frac{I_S}{2}) \geq T_{CRIT}$$

The early TB at low $I_S = 0.45$ A happened when one of CFs disappeared from DE and the survival CF2 traveled toward the same DE. The time t_{TB} could be shortened more, if both CFs are triggered and traveled toward the closest DE. The TB would not occur, if CF1 and CF2 travel into the opposite direction as presented by Figure 93 (a)-(c); (CF1 disappeared from the top DE, while CF2 turned around the opposite DE.)

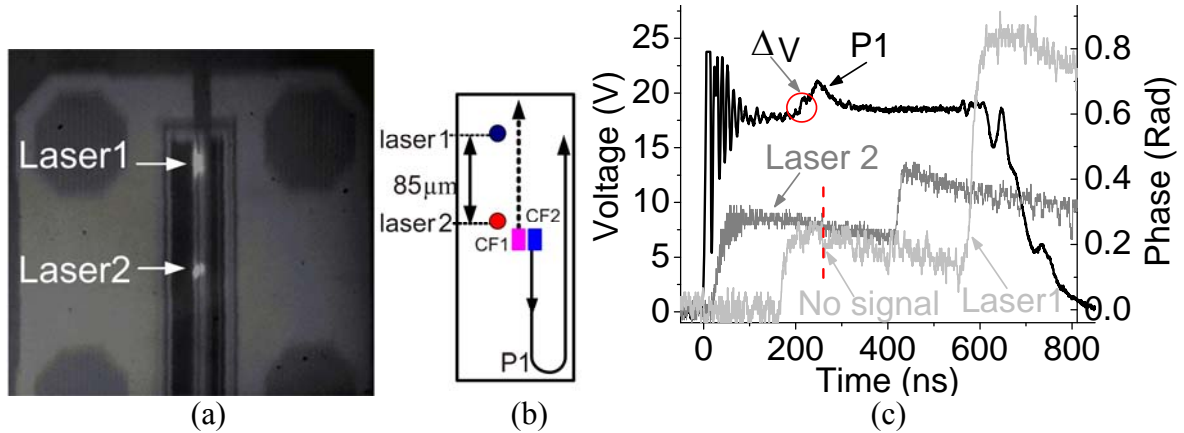


Figure 93 (a) Infrared image of NPN_Std device from backside. (b) The schematic of two moving filaments was presented with the locations of dual beams. (c) The voltage step (ΔV) was observed in $V(t)$ waveform at $I_S = 0.45$ A indicating one of CFs disappeared from the closest DE. In this case, two CFs moved toward the opposite DEs.

Here should be restated that the voltage step in waveform of linear or circular devices indicates the current redistributions during meeting of two CFs. Nevertheless, the voltage step of meander (see Figure 80 (b)) or oval devices signals the effect of resistance change (R_A or R_B) along CF passage, because these latter structures do not have the collinear edges of N⁺Emitter/ N⁺Sink and N⁺Emitter/P⁺Diffusion.

3.5 Temperature Effect on CF behavior

In a practical manner, the integrated circuits have to operate in unknown environments; therefore, the ESD PD devices inevitably face the consequences of temperature effect. The temperature induced by CF(s) itself not only affects the CF

behavior, but the homogeneous and inhomogeneous ambient temperatures (T_{AMB}) can additionally induce the thermally generated current (I_{TH}). Then these unavoidable situations are necessary to investigate how the temperature contributes any effects to CF characteristics by applying the external heat source to the ESD devices as followed;

3.5.1 Effect of Elevated Temperature

The ESD PD devices are subjected to operate in the harsh environment and the high ambient temperature; therefore, the effect of homogenous temperature to CF behaviors has been studied. The surface of NPN device was applied the homogeneously elevated temperature ($\Delta T_{ELEVATED}$) by installing the DUT on the thermal chuck.

The temperature in NPN_Std device was regulated to temperatures including 30 °C, 40 °C, 50 °C and 60 °C, afterwards the device was applied current pulses at constant $I_S = 0.34$ A, see the waveforms in Figure 94. The $V(t)$ waveform at ambient temperature (T_{AMB}) and four waveforms at the elevated temperatures were aligned their centers of the 1st V_{PEAK} . The 2nd V_{PEAK} at 30 °C and at T_{AMB} coincided, but the rest of V_{PEAK} at higher temperatures are slightly shifted further in time. The device under stressing with $I_S = 0.34$ A exhibited the TB from the temperature of 50 °C onward.

The small increment of voltage pertaining to the elevated temperatures responds to CF moving through the heated passage and CF standing on the heated DE. The broadened widths of 1st V_{PEAK} have not been clarified; therefore, for the future study the Dual Beam Michelson Interferometry technique will be required to sense the temperature on DE.

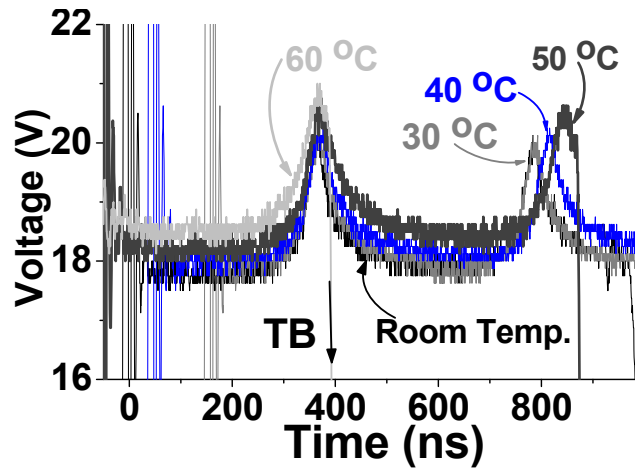


Figure 94 The compared $V(t)$ waveforms of NPN_Std device are measured at $I_S = 0.34$ A at room temperature and elevated temperatures. All the centers of 1st V_{PEAK} are aligned to demonstrate CF moving with different V_{CF} depending on the ambient temperature.

3.5.1.1 Decrease of Filament Speed at the elevated temperature

The V_{PEAK} in waveforms of Figure 94 shifted rightwards in time at the elevated temperatures ($\Delta T_{ELEVATED}$) that refers to CF spent longer times ($\frac{t_{TURN}}{2}$) on the same distance ($W_D = 200$ μ m). The study of CF speed (V_{CF}) was calculated from the time interval between

two first maximum peaks in $V(t)$ waveforms of the linear NPN_Std device. The V_{CF} is plotted as a function of I_S at the room temperature and at four elevated temperatures (30 °C, 40 °C, 50 °C, and 60 °C), see Figure 95. The V_{CF} had the increasing tendency with increasing I_S that agreed with the results of Figure 51. At constant I_S , the V_{CF} has decreased with respect to higher temperatures in the device.

The V_{CF} at two neighboring temperatures (see $\Delta T_{ELEVATED} = 30^\circ\text{C}$ and 40°C) had small variations; hence, the influence of $\Delta T_{ELEVATED}$ on V_{CF} would be noticed only when two compared temperatures of $\Delta T_{ELEVATED}$ have a significant difference. ($\Delta T \geq 20\text{-}30^\circ\text{C}$).

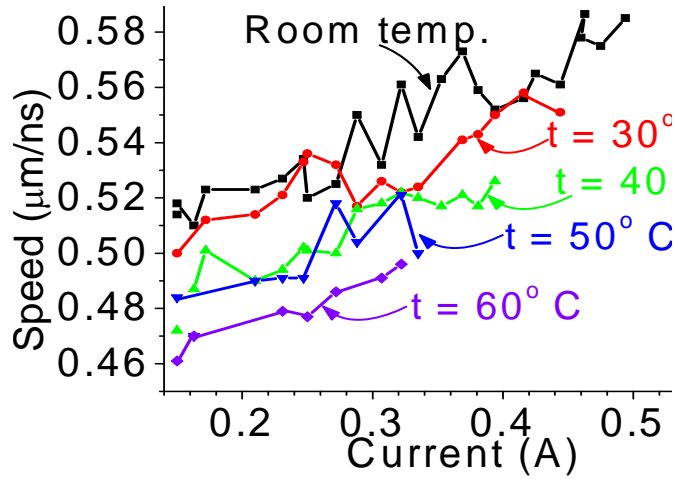


Figure 95 Speeds of moving CF in NPN_Std device were plotted as a function of I_S at the room temperature and four elevated temperatures; CF traveled with slower speeds at the higher elevated temperatures.

3.5.1.2 The shortened time to Thermal Breakdown at the elevated temperature

The elevated temperature ($\Delta T_{ELEVATED}$) not only influences the speed V_{CF} but also play an important role on the thermal breakdown. The $\Delta T_{ELEVATED}$ considered as the background temperature was uniformly added to the temperature on DE induced by a standing CF; as a result, the investigated device could exhibit the TB from a low I_S or at an earlier t_{TB} .

The voltage waveforms of Mode B and Mode C (referred to Table 9) are compared at the same I_S ; Voltage of Mode B was measured at the ambient temperature (T_{AMB}) and voltage of Mode C was recorded at the minimum temperature required to change from Mode B to C ($\Delta T_{ELEVATED} = T_{B \rightarrow C}$)

At T_{AMB} , the device reached the T_{CRIT} when CF arrived at the 2nd time on the same DE; see the top schematic of Figure 96. The temperature on DE can be expressed by;

$$T_{CF}(I_S) + \Delta T(t, I_S) \geq T_{CRIT}$$

At the $\Delta T_{ELEVATED} = T_{B \rightarrow C}$, the device temperature initially reached the T_{CRIT} when CF was the 1st time on DE that was heated with the minimum temperature.

$$T_{CF}(I_S) + 42^\circ\text{C} \geq T_{CRIT}$$

The t_{TB} of Mode C was shortened by $\frac{t_{TURN}}{2}$ at the $\Delta T_{ELEVATED} = 42^\circ\text{C}$, see the below schematic in Figure 96. This added temperature of 42°C from thermal chuck serves as the induced temperature at DE by CF from the previous passage, which leads to the early time to thermal breakdown at the same I_S .

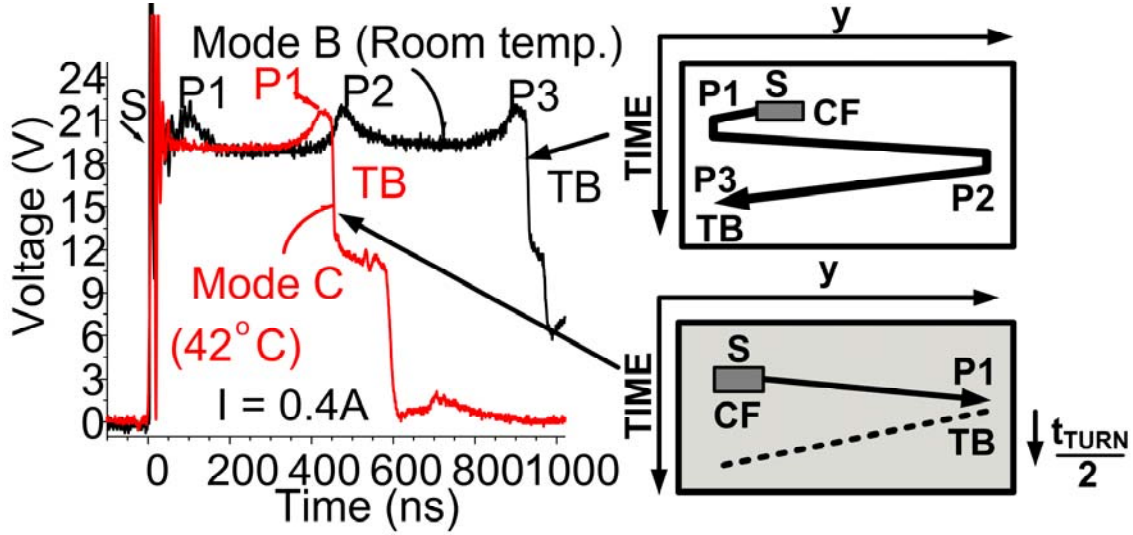


Figure 96 Two $V(t)$ waveforms of $200\ \mu\text{m}$ NPN_Std device at $I_S = 0.4\ \text{A}$ were measured at room temperature (Mode B) and 42°C (Mode C). The time to TB was shortened at the higher temperature. The right insets are the movement schematics of CF in time-space. [86]

According to the random distribution of initial CF position (see the experimental results of Figure 44) was narrowed down to around DE at high current $I_S > 0.4\ \text{A}$, the triggering positions at $I_S = 0.54\ \text{A}$ were mostly at about DE at the room temperature. Then the averaged time to thermal breakdown $\langle t_{TB} \rangle$ of Mode C was in range of 360-420 ns, see Figure 98 (a). The $\langle t_{TB} \rangle$ of Mode C under the effect of $\Delta T_{ELEVATED}$ was approximately consistent with the expression of $\langle t_{TB} \rangle \approx \frac{W_D}{V_{CF}} \approx \frac{t_{TURN}}{2}$. (Remark: The shorter time $t_{TB} \leq 300\ \text{ns}$ was rarely observed in the 1CF mode at the room temperature.)

3.5.1.3 The consistency of thermal breakdown temperature in all devices at the elevated temperature

The linear NPN device exhibited the TB only when CF was standing on DE regardless of the change of ambient temperature. The minimum temperature required to change Mode B to Mode C ($T_{B \rightarrow C}$, referred to Table 9) was plotted as a function of I_S , see Figure 97.

More experiments were repeated for investigating the other different widths of NPN_Std device including $100\ \mu\text{m}$, $200\ \mu\text{m}$, and $400\ \mu\text{m}$ as presented in Figure 97. The higher power of standing CF on DE induced more temperature change; therefore, the lesser

temperature was required to change from Mode B to Mode C corresponding to the $T_{B \rightarrow C}$ decreased so long as the I_S increased. The measured $T_{B \rightarrow C}$ from different devices had small variances at each I_S ; in other words, the TB event would happen whenever the temperature on DE reached the T_{CRIT} . The consistency in the thermal breakdown temperature has been found in all device widths.

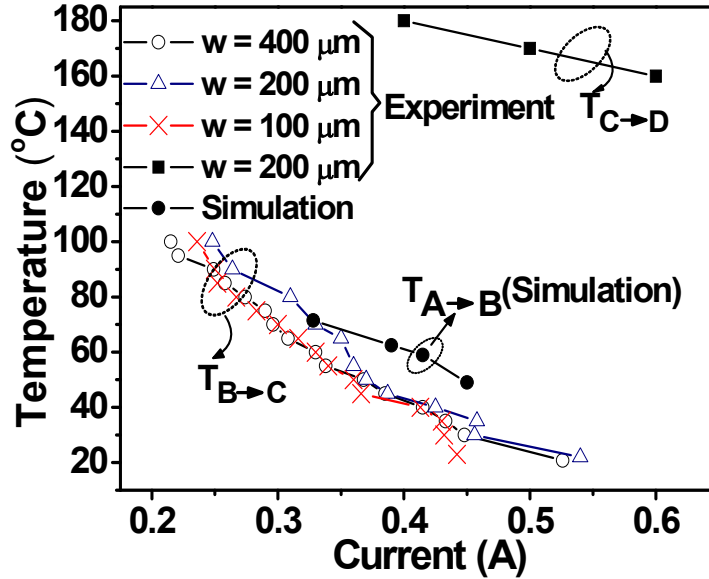


Figure 97 The minimum temperatures applied by the thermal chuck was required to change from Mode B to Mode C ($T_{B \rightarrow C}$) as a function of varied I_S for the 100, 200, and 400 μm of NPN_Std devices. And the minimum temperatures were required to change Mode C to Mode D ($T_{C \rightarrow D}$) that were around 100 $^{\circ}\text{C}$ higher than $T_{B \rightarrow C}$. The simulation of new temperature at DE due to two previous visits at the same DE as the waveforms changed from Mode A to Mode B ($T_{A \rightarrow B}$). [86]

Likewise the minimum temperature required to change Mode C to Mode D (referred to Table 9) were investigated in the 200 μm NPN_Std device. ($\Delta T_{ELEVATED} = T_{C \rightarrow D}$) The TB event of Mode D happened while CF was staying on its initial position at the $\Delta T_{ELEVATED} \approx 180$ $^{\circ}\text{C}$, see Figure 97. The $\langle t_{TB} \rangle$ of Mode D was then shortened to be ≤ 100 ns. The $T_{C \rightarrow D}$ was approximate 100 $^{\circ}\text{C}$ higher than the $T_{B \rightarrow C}$. The higher temperature of 100 $^{\circ}\text{C}$ probably associated with the temperature at DE that induced by standing CF in cumulative way until the temperature gradient on DE was sufficient to drive CF away from DE. Waveforms of Mode D in Figure 98 (b), measured at $\Delta T_{ELEVATED} = T_{C \rightarrow D} = 180$ $^{\circ}\text{C}$, did not have V_{PEAK} before the voltage drop at the TB event. This proved that TB happened outside DE. And the shortened t_{TB} of Mode D implied CF was probably standing around its initial position, while the device temperature reached the T_{CRIT} ;

$$T_{CF}(I_S) + \Delta T_{ELEVATED} (= T_{C \rightarrow D}) \geq T_{CRIT}$$

The reason of slightly shifted t_{TB} in waveforms of Figure 98 (b) was not clear, but there probably related to temperature fluctuations at various initial CF positions or probably caused from a small discrepancy in power of stress pulse from pulse to pulse. At room temperature, the TB of Mode D was not practically found at very high I_S , because multiple CFs would be rather generated instead of single CF.

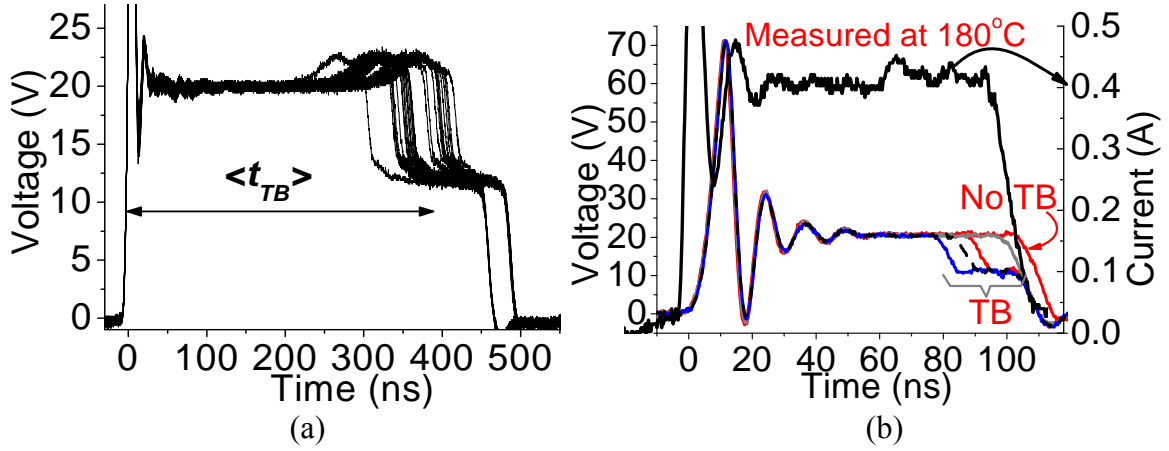


Figure 98 (a) Waveforms of Mode C shows the TB happened at the first time on DE when the 200 μm NPN_Std device was stressed with pulses at $I_S = 0.54 \text{ A}$ at room temperature (b) Waveforms of Mode D (Table 9) demonstrates TB happened at various initial CF positions when the device was stressed with pulses at $I_S = 0.4 \text{ A}$ at the elevated temperature of 180 °C. [86]

Even though the deviated t_{TB} was observed with one elevated temperature, the averaged $\langle t_{TB} \rangle$ was gradually shortened in regard to the increase of elevated temperature as observed in waveforms of Figure 99. The $\langle t_{TB} \rangle$ at very high ambient temperature was expected to be close to the time t_{STAND} .

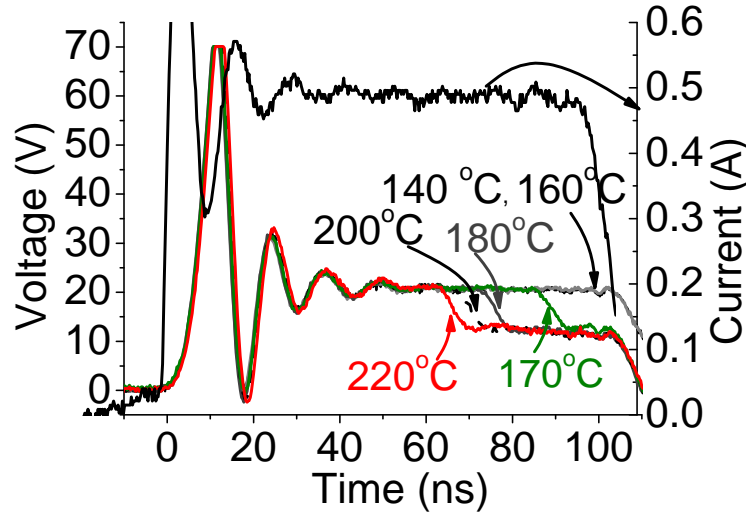


Figure 99 The $V(t)$ waveforms of NPN_Std device were measured at fixed $I_S = 0.5 \text{ A}$ at the homogeneously elevated temperatures of 140°C, 160 °C, 170 °C, 180 °C, 200 °C, and 220°C. The averaged t_{TB} decreases inversely with respect to the higher temperatures.

3.5.2 Effect of temperature gradient to filament behavior

For 2D TIM analysis, the flipped die was glued on PCB for the electrical stressing; see the image of chip backside in Figure 100 (a). Figure 100 (b) illustrates the chip under the adiabatic conditions, where the heat exchange between the device and the surrounding environment was neglected.

As the chip backside is opened, the heat accumulation in device could not be avoided during the normal operation; therefore the transient measurement was required for investigating the CF behavior under the effect of temperature gradient (T_{GRAD}).

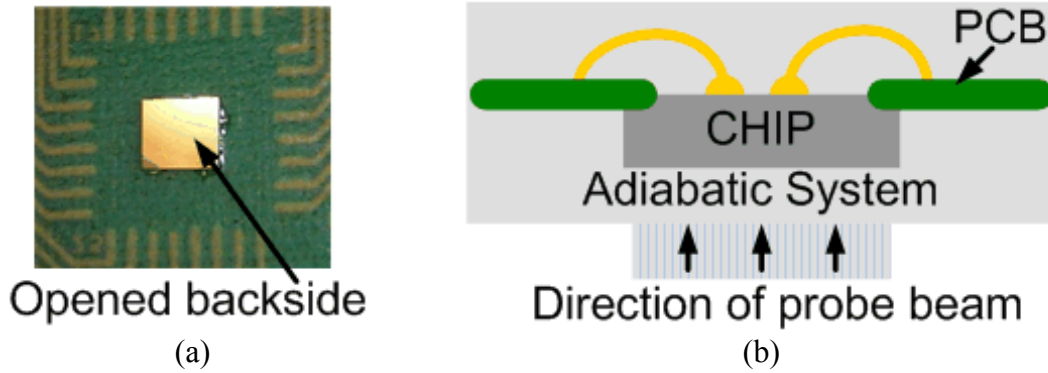


Figure 100 (a) The image was taken from the chip backside glued on PCB. (b) The schematic shows the wire-bonded chip is investigated in the adiabatic system.

The temperature gradient could be introduced to the investigated device by fabricating the resistive heater ($\approx 28 \Omega$) in the deep layer of N^+BL at distance of $40 \mu m$ (Y-axis) away from one DE of linear NPN device; see the illustration of NPN_Heater in Figure 101 (d). The gradient temperature in the CF passage was generated due to the effect of thermal resistance by applying the long DC pulse to the resistive heater before the NPN device was stressed with the ESD pulse. The heat diffused laterally from the nearby heater through the right DE introducing the temperature gradient along the device width (W_D).

The heater was firstly applied with the DC pulse with duration (τ_{HEATER}) of 150-400 μs . At the end of τ_{HEATER} , the CF behavior under the effect of T_{GRAD} was subsequently investigated by the 2D TIM technique. The schematics (a)-(c) of Figure 101 are sequentially presented in the timeline of heater stressing, ESD stressing, and laser imaging.

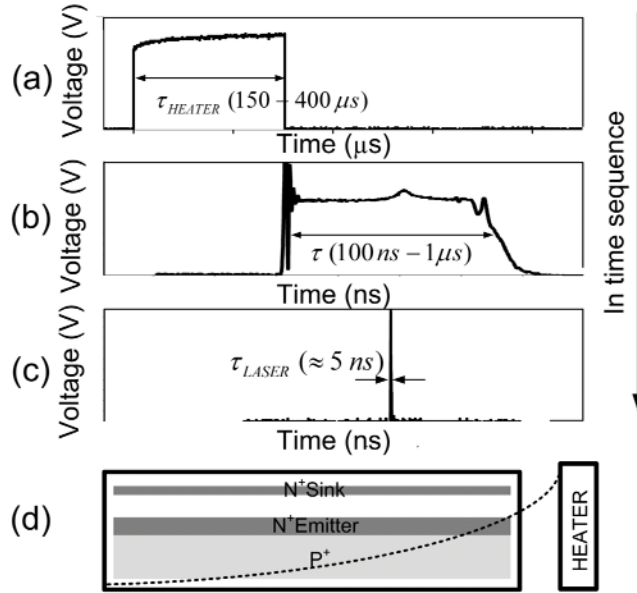


Figure 101 (a) The side heater was firstly applied the DC pulse with τ_{HEATER} of 150-400 μs . (b) The NPN_Std device was secondly stressed after the end of τ_{HEATER} . (c) The laser imaging instant of 2D TIM setup was taken within the ESD stressing period. (d) The layout of NPN_Heat device shows the side resistive heater was fabricated at 40 μm away from the right DE and the dotted line demonstrates the temperature gradient along W_D in xy-plane.

3.5.2.1 The random distribution of triggering CF positions influenced by the temperature gradient

The investigation of CF behavior in the linear NPN device under the effect of temperature gradient was observed with the 2D TIM technique. Two temperature gradients (T_{GRAD}) were applied along CF passage, and the random distribution of initial CF position would be observed under the effect of different T_{GRAD} .

The low and high T_{GRAD} were generated by applying the DC pulses to the side heater of 10 V for τ_{HEATER} of 150 μs and 15 V for τ_{HEATER} of 190 μs , respectively.

Once the T_{GRAD} had introduced along the CF passage, the initial CF position distributed within the left half of W_D in case of low power on heater and it was narrowed to DE in case of high power on heater, see Figure 102 (a) ($t_{IMAGE} \approx 95$ ns) and (b) ($t_{IMAGE} \approx 65$ ns). The leftmost DE was the preferably triggering position due to the low temperature with high impact ionization rate in that DE.

After the heater was switched off, the triggering CF position was possibly found close to right DE as typically observed at the room temperature, see Figure 102 (c) ($t_{IMAGE} \approx 65$ ns).

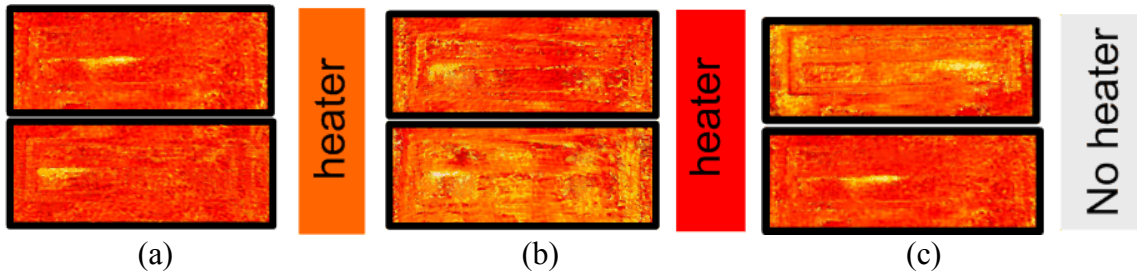


Figure 102 The phase images present the randomness of starting CF at the constant $I_S = 0.67$ A under the effect of temperature gradient controlled by different powers on heater. (a) Heater was turned on with DC pulse of 10 V 150 μ s. (b) Heater was turned on with pulse at 15 V 190 μ s. (c) Heater was turned off, the initial CF position was observed from the right DE again.

Two inhomogeneous temperature distributions along the device width were simulated with the COMSOL software. For the low power of heater in Figure 103 (a), the simulated temperature profile has 88 °C on the right DE and gradually descended to 21-23 °C around the left DE. In case of the higher power in Figure 103 (b), the temperature at the right DE was increased to 151 °C and declined to 23-25 °C on the left DE. The simulated temperature gradients along CF passage were nearly flat resembling to the elevated temperature by the thermal chuck. The possible initial CF positions, observed from the experiments of 2D TIM investigation, are marked with the solid circles. Only small temperature fluctuation could influence on the random distribution of triggering CF position.

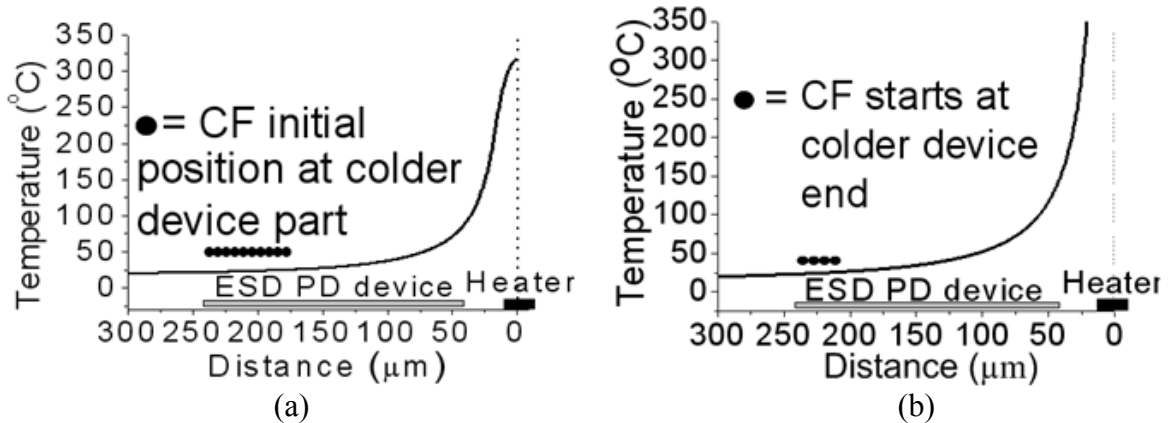


Figure 103 (a) and (b) The simulated temperature gradients with respect to the DC powers on the heater of the experimental results of Figure 102 (a) and (b), respectively. The small difference of T_{GRAD} played an important role on the random distribution of CF position as demonstrated with circles.

3.5.2.2 The shortened time to Thermal Breakdown under the temperature gradient

Once the random distribution of starting CF was constricted by the temperature distribution, the TB event was unavoidably affected. Two voltage waveforms of NPN_Std

device under stressing with constant $I_S = 0.26$ A were measured at two inhomogeneous temperature distributions generated by the side heater, see Figure 104. Waveform of Mode E was observed for the low power on right heater of 13.5 V for pulse duration (τ_{HEATER}) of 400 μ s, and waveform of Mode C (referred to Table 9) was measured at the high power on right heater of 15 V for the same duration.

Motions of CF under the two inhomogeneous temperature distributions along the device width were illustrated by the right insets of Figure 104. CF was triggered around the left DE for both filamentary modes. The TB event always happened when CF reached the right DE where has the maximum temperature diffused from the side heater. The temperature on DE of Mode E can be expressed by;

$$T_{CF}(I_S) + \frac{\partial T}{\partial y}(V, \tau_{HEATER}) + \Delta T(I_S, t) \geq T_{CRIT}$$

where $\Delta T(I_S, t)$ is the accumulated temperature on the right DE induced by CF from the previous passage (P2). $\frac{\partial T}{\partial y}(V, \tau_{HEATER})$ is the inhomogeneous temperature distribution along

the device with depending on the power of heater. Mode E had the t_{TB} of about $\frac{3t_{TURN}}{2}$, and then the t_{TB} of Mode C was shortened by t_{TURN} due to the small increase of temperature distribution. (Remark Mode E was never commonly observed at the room temperature)

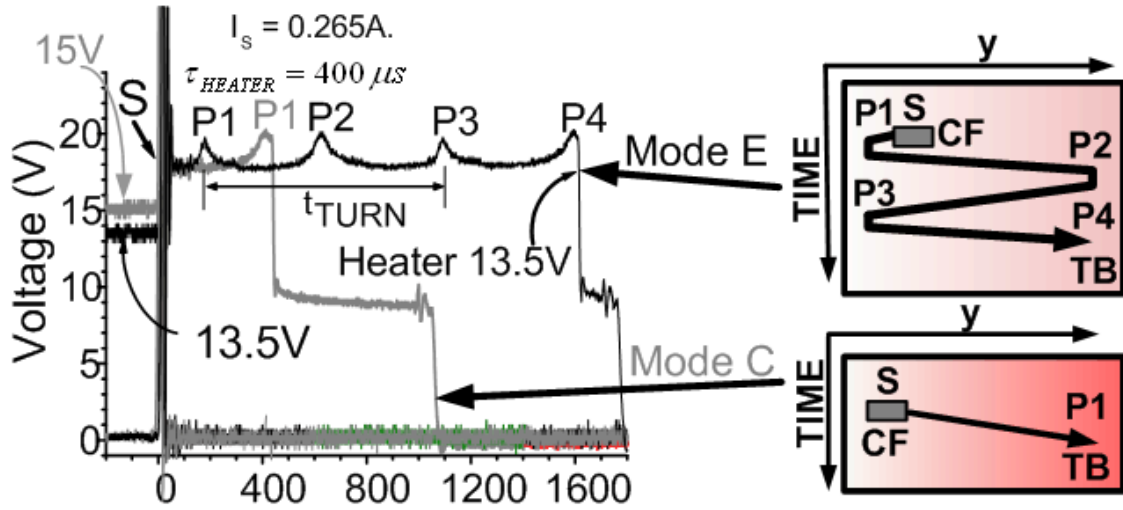


Figure 104 Voltages waveforms of NPN Std device were observed under two different T_{GRAD} at the same $I_S = 0.265$ A present the shortened t_{TB} from Mode E (high power on heater) to Mode C (low power on heater) and the insets demonstrate the CF motions.

3.5.2.3 The controlled time to Thermal Breakdown under temperature gradient

The ESD device operates commonly at the room temperature or at the inhomogeneous temperature change. Then the t_{TB} at the room temperature was compared with at the inhomogeneous temperature distribution. In practical, 1CF and 2CFs modes alternately happened from pulse to pulse at $I_S = 0.54$ A; therefore in these study waveforms of two filamentary modes were collected and presented together.

At the room temperature, CF(s) was triggered more random yielding more scattering of t_{TB} in range of 290-420 ns (see Figure 105 (a)). At an inhomogeneous temperature distribution, the averaged time to TB $\langle t_{TB} \rangle$ was determined from the traveling time across device width of $200\text{ }\mu\text{m}$ ($\approx \frac{t_{TURN}}{2}$), see Figure 105 (b).

With the introduction of temperature distribution, CF was restricted to be triggered from the opposite DE of the heater. If the device width is prolonged, the longer $\langle t_{TB} \rangle$ can be expected offering more robustness. In addition, the time interval of CF turning around DE $\langle t_{DE} \rangle$ (marked in Figure 105 (b)) was shortened by about 20 ns (By comparing the profiles of voltage peaks between waveforms in Figure 105 (a) and (b)).

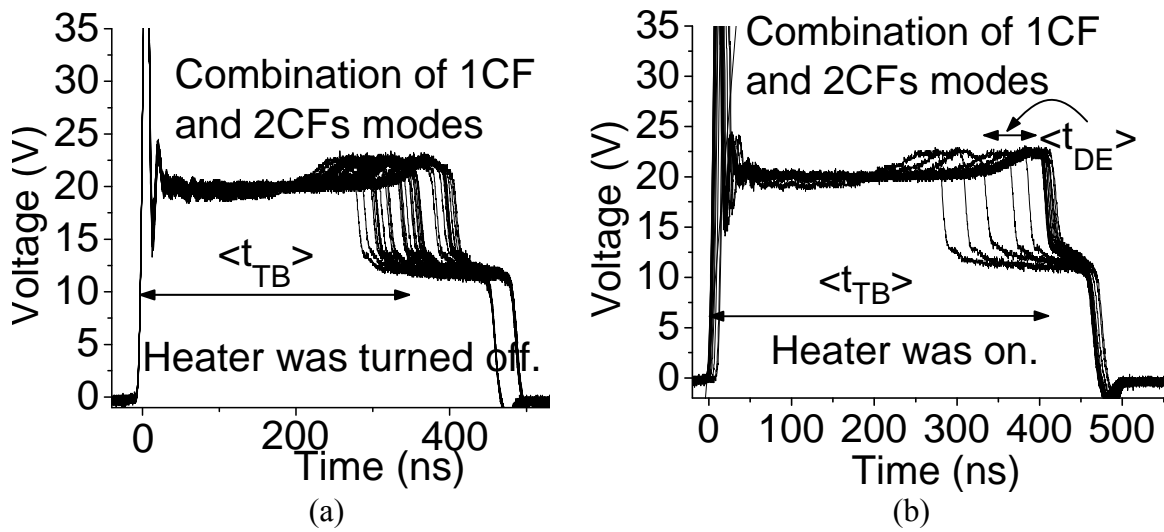
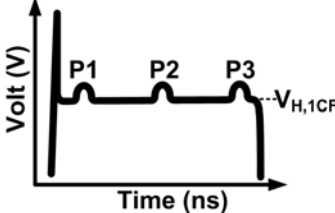
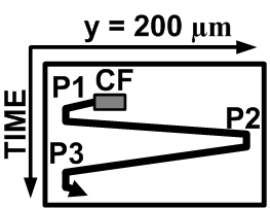
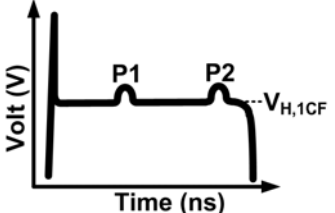
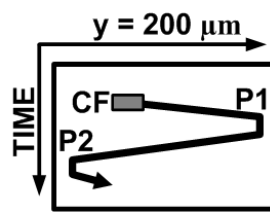
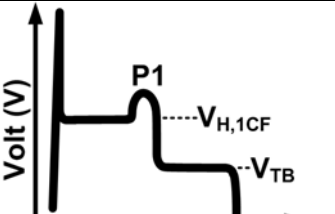
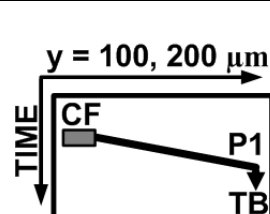
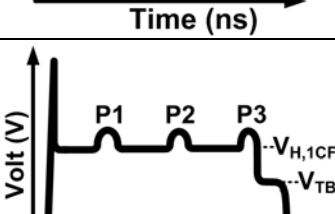
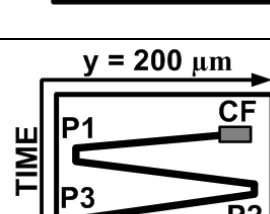
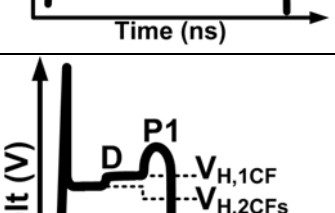
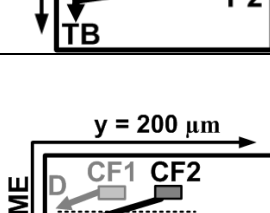
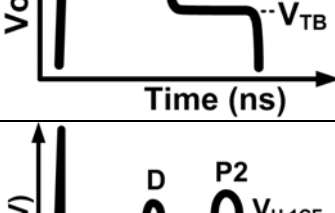
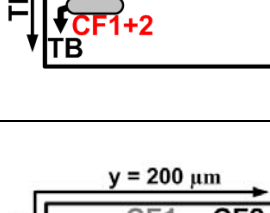


Figure 105 The averaged times to TB $\langle t_{TB} \rangle$ of NPN_Std device were observed at $I_S = 0.54$ A when the device was subjected to two temperatures; (a) the room temperature (b) the temperature gradient. The $\langle t_{TB} \rangle$ at the temperature gradient was longer and approximated to traveling time across the device width ($200\text{ }\mu\text{m}$), and the time of CF standing on DE before TB event $\langle t_{DE} \rangle$ was shortened for about 20 ns.

3.6 Summary of CF(s) modes

Voltage waveforms	Moving CF(s) schematics	Description
		CF made the first turnabout (P1) at the nearest DE, observed only at low $I_S = 0.25$ A.
		CF preferably turned around for the first time on the far DE at $I_S \geq 0.4$ A.
		The device exhibited the TB at the 1 st arrival of CF on DE at $I_S > 0.53$.
		The device exhibited the TB when CF visited (P3) the preheated DE, where induced by CF from the previous passage (P1), observed at $I_S \approx 0.3-0.5$ A.
		CF1 disappeared (D) from DE. The early TB happened ($I_S \geq 0.45$ A) after the transition of two CFs to one CF (CF1+2) and that CF1+2 arrived the same-preheated DE. In this mode time T_{TB} was shortened.
		CF1 disappeared (D) from DE after it attempted to turn around DE.

		<p>Device did not exhibit the TB, if two CFs moved toward the opposite DEs. Time T_{TB} was extended.</p>
		<p>CF1 disappeared from DE, at the same time CF2 arrived the opposite DE.</p>
		<p>CF1 disappeared from DE. Then the current was totally occupied by CF2. Thereafter CF1+2 tried to split itself up during moving.</p>
		<p>At $I_S = 0.75$, CF1 and CF2 had large sizes. The 1st large V_{PEAK} (P1) was corresponded to the meeting of CFs (M). TB happened when CF1 and CF2 arrived the DEs.</p>
		<p>Small increasing voltage (ΔV) was a result of CF moved through the preheated passage. Two CFs existed until time t_{TB}. This experiment was observed by the 2 Beams Michelson Int..</p>
		<p>CF1 met ($M = P1$) CF2 before it disappeared (D) from DE. ($I_S > 0.53$ A). Then TB happened when CF1+2 arrived the DE.</p>
		<p>CF1 and CF2 moved past each other ($M = P1$). Then CF1 disappeared (D) from DE, while CF2 was turning around the opposite DE (Unusual voltage step appeared instead of voltage peak). TB happened when CF1+2 arrived the preheated DE.</p>

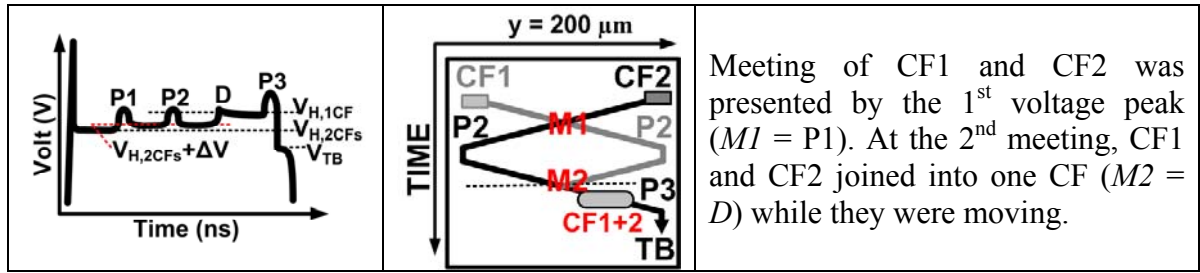


Table 10 Schematics of voltage waveforms in the 1st column and the CF(s) movement in space-time in the 2nd column relate to the waveform were observed in the linear device. All notations in both columns are the same; $P1, \dots, P3$ = CF turnabout device end, D = CF disappeared, M = Meeting of two CFs, $CF1+2$ = Transition of two CFs to one CF, $V_{H,1CF}$ = Holding voltage in single CF mode, $V_{H,2CFs}$ = Holding voltage in two CFs mode, and ΔV = The increased holding voltage due to CF moving through the preheated passage

Chapter 4

Conclusion

The CF behavior in the smart power ESD protection devices has been studied through the electrical and optical measurements. Some important factors determining the CF behavior have been found: stress current I_S , the thermal prehistory in the device, the different layout of device, ambient temperature and temperature gradient along the device width. The results can be summarized as follows:

Basic CF characteristics:

- 1) The measured CF size (W_{CF}) was about $\approx 20\text{-}25\text{ }\mu\text{m}$ that matches with the distance between collector and emitter edges (L).
- 2) The filament speed (V_{CF}) increased proportionally to I_S ; however it slightly decreased at the higher ambient temperature in the devices.
- 3) CF spent time of 30-40 ns on DE of linear device for raising the temperature gradient at the front wall before it could move further through the previously heated passage.
- 4) The current redistribution between multiple CFs yielded the meeting or splitting phenomena.

The dependence of stress current I_S :

- 1) The random distribution of initial CF position was narrowed down at the higher stress current.
- 2) The averaged CF number increased proportionally to the increase of current I_S .
- 3) The time t_{TB} was shortened by increasing of current I_S .

The thermal effects:

- 1) In long pulse duration (τ) the CF had much more complicate behavior than in short τ because CF characteristic was influenced by the previously induced temperature in the device.
- 2) The voltage step indicates CF moving through the preheated passage. So long as the induced temperature by CF continuously accumulated in device, the voltage was increased stepwise.
- 3) The homogeneously elevated temperature had no impact on the random triggering CF position, only the temperature gradient could narrow down the random distribution of initial position to a colder DE of linear device.
- 4) Due to the heat accumulation in device, the increase of width (or diameter), increasing the roundtrip time, allows the device exhibiting TB at higher I_S .

5) With increasing of the ambient temperature, the time t_{TB} was shortened step wise such was observed in Table 9; Mode A (B) changed to Mode B (C). These modes presented the TB happening at DE for the increased ambient temperature up to 100°C. If the ambient temperature increased to about 180°C, the TB could present at a triggered CF position as observed in Mode D.

The different device layouts:

1) The linear device preferably exhibited TB at DE, but the other structures exhibited at a random position. Therefore the devices without DE were more robust.

2) The voltage step indicates the CF entering the passage at elevated temperatures, and the CF moving through the passage with the access resistance change and base resistance change (R_A and R_B).

3) In linear device, the voltage step was an evidence of transition of two CFs to single CF as a consequence of the CF disappearance from a device end.

4) The high R_A along passage leads to the TB during two CFs meetings within that region as observed in Meander device.

5) Resistance R_B played a more important role on moving CF than R_A ; the moving speed would be significantly reduced, if CF entered the region of high R_B .

Practical relevance of the work:

Some aspects about current filament behavior causing the thermal destruction and the structures of ESD protection devices were briefly commented that could be the practical information as followed;

1) One could expect the large width of linear device had more robustness due to it offered a long roundtrip time of single CF to preheated DE at low current regime ($I_S < 0.3$ A). (Mode A in Table8) However, the larger widths did not always offer the longer time to TB (t_{TB}). Because the random triggering CF position and moving direction regulated the traveling time to DE, one could observed the larger device width had a shorter time t_{TB} than a smaller device at the nearly same I_S ($I_S = 0.5$ A). [83]

2) 13% of waveform exhibited two CFs modes, while the rest exhibited one CF mode at $I_S = 0.47$ A. Less than 50% of waveforms of two CFs the complex dynamics could shorten t_{TB} to be at an earlier than t_{TB} of single CF in linear structure at a fixed I_S (0.45 A). Likewise, more number of CFs at higher I_S ($N > 2$) could shorten more t_{TB} due to the wider distribution of initial CF positions and the current redistribution among them.

3) The stopping of CF after TB for a long period of burnout in linear devices could be considered as non destructive effect, only if the I_S was relatively low (Burnout time of up to 200 ns was safe for $I_S < 0.5$ A). On the other hand, most of devices failed after a few pulses with long burnout (≥ 200 ns) at high $I_S > 0.7-0.8$ A.

4) The linear structure has a weak point at DE; therefore, the structures without DE could withstand more number of long pulses due to the random location of TB event.

5) The meeting of two CFs in region with a higher resistance (R_A or R_B) in traveling passage caused the TB event, but not in region with a lower resistance at the same I_S ; therefore the collinear edges of collector/base and emitter/base junctions should be an optimal layout such as the circular structure.

6) With large structures the temperature gradient influenced on the initial CF position and location of TB event. But the small device the temperature gradient could be

considered as the homogeneous temperature distribution; therefore, the initial CF position and TB location were expected to be similar to the situation of at room temperature.

Large ESD protection devices consuming large silicon area did not always contribute the best protective performance due to there were many restrictions. Therefore, the ESD protection devices should be designed to fit into the ESD protection window of each application.

References

- [1] A. Amerasekera and J. Verwey, "ESD in integrated circuits", *Qual. Reliab. Eng. Int.*, vol.8, pp. 259-272, 1992.
- [2] C. Fürböck, K. Esmark, M. Litzenberger, D. Pogany, G. Groos, R. Zelsacher, M. Stecher, and E. Gornik, "Thermal and free carrier concentration mapping during ESD event in smart power ESD protection devices using an improved laser interferometric technique", *Microelectron. Reliab.*, vol. 40, pp. 1365-1370, 2000.
- [3] D. Pogany, S. Bychikhin, J. Kuzmik, V. Dubec, N. Jensen, M. Denison, G. Groos, M. Stecher, and E. Gornik, "Thermal distribution during destructive pulses in ESD protection devices using a single-shot two-dimensional interferometric method", *Solid. State. Electronics*, vol. 49, no. 3, 2005, pp. 421-429.
- [4] C. Fürböck, D. Pogany, M. Litzenberger, E. Gornik, N. Seliger, H. Gossner, T. Müller-Lynch, M. Stecher, W. Werner, "Interferometric temperature mapping during ESD stress and failure analysis of smart power technology ESD protection devices", *J. Electrostatics*, vol. 49 (3-4), pp. 195-213 (2000).
- [5] D. Pogany, C. Fürböck, M. Litzenberger, G. Groos, K. Esmark, P. Kamvar., H. Gossner, M. Stecher, and E. Gornik, "Study of trigger instabilities in Smart Power Technology ESD protection devices using a laser interferometric thermal mapping technique", *EOS/ESD Symp.* (2001), p. 214-225.
- [6] K. Skadron, et al., "Temperature-Aware Computer Systems: Opportunities and Challenges," *IEEE Micro*, Vol. 23, No. 6, November/December 2003, pp. 52 - 61.
- [7] [M Chaine, CT Liong, and HF San, "A Correlation Study Between Different Types of CDM Testers and 'Real' Manufacturing In-Line Leakage Failures," in *Proceedings of the EOS/ESD Symposium* (Las Vegas, NV: ESD Association, 1994): 63–68
- [8] ISO TR 10605, International Organization for Standardization, "Road vehicles – Electrical disturbances from electrostatic discharges", Geneva, Switzerland, 1994.
- [9] IEC 61000-4-2, "Electromagnetic compatibility (EMC) – Part 4-2: testing and measurement techniques – electrostatic discharge community test. Ed 2.0, 2008-12, ISBN: 2-8318-1019-7.
- [10] ESD Association. ESD standard test method for electrostatic discharge sensitivity testing – Human Body Model (HBM) component level (ESD STM5.1-2001), of ESD Association Working Group WG 5.1; 2001. JEDEC electrostatic discharge (ESD) sensitivity testing Human Body Model (HBM), JESD22-A114D; March 2006.
- [11] ESD Association. ESD standard test method for electrostatic discharge sensitivity testing – Machine Model (MM) component level (ESD STM5.2-1998), of ESD Association Working Group WG 5.3.1; 1998.
- [12] ESD Association. ESD standard test method for electrostatic discharge sensitivity testing – Charged Device Model (CDM) component level (ESD STM5.3.1-1999), of ESD Association Working Group WG 5.3.1; 2001.
- [13] "EOS/ESD-S5.1-1993," EOS/ESD Association Standard for Electrostatic Discharge (ESD) Sensitivity Testing –Human Body Model (HBM) – Component Level, June 9, 1993.
- [14] MIL-STD-883D, Notice 8, Method 3015.7, "Electrostatic Discharge Sensitivity Test," 1998.

- [15] "EOS/ESD-S5.2-1994," ESD Association Standard for Electrostatic Discharge (ESD) Sensitivity Testing –Machine Model (MM) – Component Level, June 2, 1994.
- [16] ISO 7637-1, International Organization for Standardization, "Road vehicles-Electrical disturbance by conduction and coupling", Geneva, Switzerland, 1990.
- [17] R.A. Ashton, "System Level ESD testing: The test setup", Conformity, December 2007, p. 34.
- [18] D. Johnsson, M. Mayerhofer, J. Willemen, U. Glaser, D. Pogany, E. Gornik, and M. Stecher, "Avalanche Breakdown Delay in High- Voltage p-n Junctions Caused by Pre-Pulse Voltage From IEC 61000-4-2 ESD Generators", IEEE Trans. Dev. Reliab., vol. 9, No.3, September 2009, p. 412-418.
- [19] M. Denison, "Single stress safe operating area of DMOS transistors integrated in Smart Power Technologies", Dissert. Uni. Bremen, 2005.
- [20] Murari B., Smart Power ICs, Springer, Berlin 1996.
- [21] C. Salamero, N.Nolhier, A. Gendron, M. Bafleur, P. Besse, M. Zecri, TCAD methodology for ESD robustness prediction of smart power ESD devices. IEEE Trans. Dev. Mat. Reliab, vol. 6, no. 3 2006 pp.399-407.
- [22] T. J. Green and W. K. Denson, "A review of EOS/ESD field failures in military equipment", in Proc. EOS/ESD Symp., 1988, pp.7-14.
- [23] C. Duvvury, R. N. Rountree, Y. Fong, and R. A. Mcphee, "ESD phenomena and protection issues in CMOS output buffers", in Proc. IRPS, 1987, p.174.
- [24] C. Duvvury and R. Rountree, "A synthesis of ESD protection scheme", in Proc. EOS/ESD Symp., 1991, p.88.
- [25] M. D. Ker, "Whole-Chip ESD protection design with efficient VDD-to-VSS ESD clamp circuits for submicron CMOS VLSI", IEEE Trans. Elect. Dev., vol. 46, no. 1, pp. 173-183, Jan 1999.
- [26] M. Mergens, M. Mayerhofer, J. Willemen, M. Stecher, "ESD Protection Considerations in Advanced High-Voltage Technologies for Automotive", EOS/ESD Symposium 06-54.
- [27] Ming-Dou Ker, and Kuo-Chun Hsu, "Overview of On-Chip Electrostatic Discharge Protection Design With SCR-Based Devices in CMOS Integrated Circuits", IEEE, Dev. Relia., vol. 5, No. 2, June 2005.
- [28] D. Johnsson, M. Mayerhofer, J. Willemen, U. Glaser, D.Pogany E. Gornik, M. Stecher, Avalanche breakdown delay in high voltage PN-junctions, caused by pre-current from IEC 61000-4-2 generators, IEEE Trans. Dev. Mat. Reliability, 2009, vol.9, 2009, p.412-418.
- [29] N. Jensen, G. Groos, M. Denison, J. Kuzmik, D. Pogany, E. Gornik, M. Stecher, "Coupled bipolar transistors as very robust ESD protection devices for automotive applications", EOS/ESD Symp., Las Vegas, NV, 2003.
- [30] D. Pogany, Fellow, IEEE, D. Johnsson, S. Bychikhin, K. Esmark, P. Rodin, M. Stecher, E. Gornik, and H. Gossner, "Measuring Holding Voltage Related to Homogeneous Current Flow in Wide ESD Protection Structures Using Multilevel TLP", IEEE Trans. Elect. Dev., Vol. 58, No. 2, February 2011.
- [31] B K Ridley, "Specific Negative Resistance in Solids", Proc. Phys. Soc. ,82, 1963, p. 954.
- [32] V. L. Bonch-Bruevich, I. P. Zvjagin, and A. G. Mironov, Domain Electrical Instabilities in Semiconductors, Consultant Bureau, New York, 1975.
- [33] Seliger N, Habas P and Gornik E, "A study of backside laser-prober signals in MOSFETs", Microel. Engn., 1995, 31, pp. 87-94.
- [34] Kasapi S, Tsao, C-C, Wilsher K, Lo W and Somani S, "Laser beam backside probing of CMOS integrated circuits", Microel. Reliab. 1999; 39, pp. 957-961.

- [35] E. Schöll, "Nonlinear Spatio-Temporal Dynamics and Chaos in Semiconductors Cambridge University Press", Cambridge, 2001.
- [36] D. Pogany, D. Johnsson, S. Bychikhin, K. Esmark, P. Rodin, E. Gornik, M. Stecher, H. Gossner, "Nonlinear dynamics approach in modeling of the on-state-spreading - related voltage and current transients in 90nm CMOS silicon controlled rectifiers", International Electron Devices Meeting (IEDM), Baltimore, USA; 12-07-2009 - 12-09-2009; in: "IEDM 09", 2009, 509 - 512.
- [37] M. Meixner, P. Rodin, E. Schöll, A. Wacker, "Lateral density fronts in globally coupled bistable semiconductors with S- or Z-shaped current voltage characteristics". *Eur. Phys. J. B*, vol.13, 2000, pp.157-168
- [38] D. Pogany, V. Dubec, S. Bychikhin, C. Fürböck, M. Litzenberger, G. Groos, M. Stecher, and E. Gornik, "Single-shot thermal energy mapping of semiconductor devices with nanosecond resolution using holographic interferometry", *IEEE Electron Device Lett.*, vol. 23, pp. 606-608, Oct. 2002.
- [39] C. Fürböck, K. Esmark, M. Litzenberger, D. Pogany, G. Groos, R. Zelsacher, M. Stecher, and E. Gornik, "Thermal and free carrier concentration mapping during ESD event in smart power ESD protection devices using an improved laser interferometric technique", *Microelectron. Reliab.*, vol. 40, pp. 1365-1370, 2000.
- [40] P. Rodin, "Theory of traveling filaments in bistable semiconductor structures", *Physical Revue B, Condensed Matter and Materials Physics*, Vol. 69, No. 4, p. 45307-1-11, 2004.
- [41] A. Amerasekera, and J. A. Seitchik, "Electrothermal Behavior of Deep Submicron nMOS Transistors Under High Current Snapback (ESD/EOS) Conditions", *IEDM'94 Techn. Digest*, 1994, p. 455-458.
- [42] S. K. Ghandhi, *Semiconductor Power Devices*, New York: Wiley, 1997.
- [43] W. R. Runyan, "Silicon Semiconductor Technology", New York: McGraw-Hill. 1965.
- [44] A. Amerasekera, L.V.Roozendaal, J. Bruines, and F. Kuper, "Characterization and Modeling of Second Breakdown in NMOST's for the Extraction of ESD-Related Process and Design Parameters", *IEEE Trans. Elect. Devices*, vol. 38, no. 9, Sept 1991.
- [45] D. Pogany, S. Bychikhin, J. Kuzmik, V. Dubec, N. Jensen, M. Denison, G. Groos, M. Stecher, and E. Gornik, *IEEE, IEDM'2002 special issue of IEEE TDMR*, 2002.
- [46] H. A. Schaff and J. C. French, "Second breakdown in transistors", *IRE Trans. Electron Devices*, vol. ED-9, pp. 129-136, Mar. 1962.
- [47] I. P. Herman, "Real-time optical thermometry during semiconductor processing", *IEEE J.Sel.Top.Quant.Electr.*, vol. 1, no.4, pp. 1047-1053, 1995.
- [48] J.Y. Glaceta and S. Berne, "A practical system for hot spot detection using fluorescent microthermal imaging", *Microelec. and Reliab.*, vol. 36, issues 11-12, Nov.-Dec. 1996, p 1811-1814.
- [49] W. Claeys, S. Dilhaire, and V. Quintard, "Laser probing of thermal behavior of electronic components and its application in quality and reliability testing", *Microelectronic Eng.*, vol. 24, pp. 411-420, 1994.
- [50] H. W. Icenogle, B. C. Platt, and W. L. Wolfe, "Refractive indexes and temperature coefficients of germanium and silicon", *Applied Optics*, vol. 15, no. 10, pp. 2348-2351, 1976.
- [51] V. M. Donnelly and J. A. McCualley, "Infrared laser interferometric thermometry: a nonintrusive technique for measuring semiconductor wafer temperatures", *J. Vac.Sci.Technol.*, vol. A8, no.1, pp.84-92, 1990.

- [52] M. Goldstein, "Heterodyn Interferometer zur Detektion elektrischer und thermischer Signale in integrierten Schaltungen durch die Substratrückseite, Ph.D. Thesis, TU Munich, Munich, 1993.
- [53] E.F. Burtsev, I.V. Grekhov and N.N. Kryukova. Localization of the current in silicon diodes at high forward current densities. Soviet Physics Semiconductors, vol. 4, no. 10, pp. 1675[±] 1680, 1971.
- [54] V.A. Vashchenko, J.B. Martynov, V.F. Sinkevitch and A.S. Tager. Current instability in GaAs n⁺-i-n⁺ structures as a limitation of the maximum drain voltage in power MESFETs. Solid State Electronics, vol. 39, no. 7, pp. 1027[±] 1031, 1996.
- [55] C. Duvvury, C. Diaz and T. Haddock. Achieving uniform nMOS device power distribution for sub-micron ESD reliability. In Proc. of the Int. Electron Devices Meeting, pages 131[±] 134, 1992.
- [56] J. Oetjen, R. Jungblut, U. Kuhlmann, J. Arkenau and R. Sittig. Current Filamentation in bipolar power devices during dynamic avalanche breakdown. Solid State Electronics, vol. 44, pp. 117[±] 123, 2000.
- [57] K.H. Oh, C. Duvvury, K. Banerjee and R.W. Dutton. Analysis of nonuniform ESD current distribution in deep submicron NMOS transistors. IEEE Trans. Electron Devices, vol. 49, pp. 2171[±] 2182, 2002.
- [58] W. B. Smith, D. H. Pontius, and P. P. Budenstein, "Second breakdown and damage in junction devices", IEEE Trans. Electron Devices, vol. 20, pp. 731-744, 1973.
- [59] T. Maloney and N. Khurana, "Transmission Line Pulsing techniques for circuit modeling of ESD phenomena", in Proc. EOS/ESD Symp., 1985, pp.49-54.
- [60] M. Blaho, L. Zullino, H. Wolf, R. Stella, A. Andreini, H. A. Gieser, D. Pogany, and E. Gornik, "Internal Behavior of BCD ESD Protection Devices Under TLP and Very-Fast TLP stress", IEEE Trans. Dev. and Materials Relia., vol. 4, No. 3, Sept. 2004.
- [61] M. Denison, M. Blaho, P. Rodin, V. Dubec, D. Pogany, D. Silber, E. Gornik, M. Stecher, "Moving Current Filaments in Integrated DMOS Transistors Under Short-Duration Current Stress", IEEE Transactions on Electron Devices, **51** (2004), 10; 1695 - 1703.
- [62] G. Krieger, "Thermal response of integrated circuit input devices to an electrostatic energy pulse", IEEE Trans. Electron Devices, vol. ED-34, pp. 877-882, Apr. 1987.
- [63] M. Bertolotti, V. Bogdanov, A. Ferrari, A. Jascow, N. Nazorova, A. Pikhtin, and L. Schirone, "Temperature dependence of the refractive index in semiconductors", J. Opt. Soc. Am. B, vol. 7, 1990, pp.918-922.
- [64] J. C. Sturm and C. M. Reaves, "Silicon temperature measurement by Infrared absorption: Fundamental processes and doping effects", IEEE Trans. Electron Devices, vol.39, no.1, 1992, pp. 81-88.
- [65] R. A. Soref, B. R. Bennett, Electrooptical Effects in Silicon, IEEE J. Quant. Electron. **23**, 123 (1987).
- [66] D. K. Schroder, R.N. Thomas and J. C. Swartz, "Free carrier absorption in silicon", IEEE Trans. Electron Device, ED-25, 1978, pp. 254-261.
- [67] N. Seliger, P. Habas, D. Pogany and E. Gornik, "Time-resolved analysis of self-heating in power VDMOSFETs using backside laser probing", Solid State Electron, 41, 1997, pp. 1285-1292.
- [68] D. Pogany, S. Bychikhin, C. Fürböck, M. Litzenberger, and E. Gornik, "Quantitative Internal Thermal Energy Mapping of Semiconductor Devices Under Short Current Stress Using Backside Laser Interferometry", IEEE Trans. Electron Devices, vol. 49, No. 11, Nov. 2002.

- [69] J. A. McCaulley, V. M. Donnelly, M. Vernon, and I. Taha, "Temperature dependence of the near-infrared refractive index of silicon, gallium arsenide, and indium phosphide", *Phys. Rev. B.*, vol. 49, 1994, pp. 7408-7417.
- [70] D. Pogany, S. Bychikhin, E. Gornik, M. Denison, N. Jensen, G. Groos, and M. Stecher, "Moving current filaments in ESD Protection devices and their relation to electrical characteristic", *IEEE 41st Annual Inter. Reliab. Phy. Symp.*, Texas, 2003.
- [71] D. Pogany, S. Bychikhin, M. Litzenberger, E. Gornik, G. Groos and M. Stecher, "Extraction of spatio-temporal distribution of power dissipation in semiconductor devices using nanosecond interferometric mapping technique", *Appl. Phys. Lett.*, 81, 2002, pp. 2881-2883.
- [72] M. Litzenberger, "Investigation of internal behavior in CMOS ESD protection devices under high current stress", PhD Dissertation, Vienna University of Technology, Vienna, 2003.
- [73] Litzenberger M, Fürböck C, Bychikhin S, Pogany D and Gornik E. Scanning Heterodyne Interferometer Setup for the Time-Resolved Thermal and Free-Carrier Mapping in Semiconductor Devices. *IEEE Trans. Instrum. Meas.*, vol. 54, no. 6, 2005, pp. 2438-2445.
- [74] V. Dubec, S. Bychikhin, M. Blaho, D. Pogany, E. Gornik, J. Willemen, N. Qu, W. Wilkening, L. Zullino and A. Andreini: "A dual-beam Michelson interferometer for investigation of trigger dynamics in ESD protection devices under very fast TLP stress," *Microel. Reliab.*, 43, 2003, pp. 1557-1561.
- [75] Viktor Dubec, "Advanced optical interferometric methods for nanosecond mapping of semiconductor devices under high energy pulses", Ph.D Dissertation, Vienna University of Technology, Vienna, 2005.
- [76] V. Dubec, S. Bychikhin, D. Pogany, E. Gornik, T. Brodbeck, W. Stadler, "Backside interferometric methods for localization of ESD-induced leakage current and metal shorts", *Microelec. Reliab.*, vol. 47, (2007), pp. 1549-1554.
- [77] M. Denison, M. Blaho, D. Silber, J. Joost, N. Jensen, M. Stecher, V. Dubec, D. Pogany and E. Gornik, "Hot spot dynamics in quasi vertical DMOS under ESD stress", *Proc. ISPSD'03*, 2003, pp. 80-83.
- [78] D. Pogany, V. Dubec, S. Bychikhin, C. Fuerboeck, M. Litzenberger, S. Naumov, G. Groos, M. Stecher, E. Gornik, "Single-Shot Nanosecond Thermal Imaging of Semiconductor Devices Using Absorption Measurements", *IEEE Trans. Dev. Mat. reliab.*, vol. 3, no. 3, 2003, pp. 85-88.
- [79] V. Dubec, S. Bychikhin, M. Blaho, M. Heer, D. Pogany, M. Denison, N. Jensen, M. Stecher, G. Groos, E. Gornik, "Multiple-time-instant 2D thermal mapping during a single ESD event", *Microelectronics Reliability*, 44 (2004), pp. 1793 - 1798.
- [80] W. Mamane, D. Johnsson, P. Rodin, S. Bychikhin, V. Dubec, M. Stecher, E. Gornik, and D. Pogany, "Interaction of traveling current filaments and its relation to a nontrivial thermal breakdown scenario in avalanching bipolar transistor", *Journal of Applied Physic*, vol. 105, 084501 (2009)
- [81] M. Denison, M. Blaho, P. Rodin, V. Dubec, D. Pogany, D. Silber, E. Gornik, and M. Stecher, "Moving Current Filaments in Integrated DMOS Transistors Under Short-Duration Current Stress", *IEEE Trans. Electron Dev.*, vol. 51, No. 10, 2004, pp. 1695-1703.
- [82] G. Wachutka, "Analytical model for the destruction mechanism of GTO-like devices by avalanche injection", *IEEE Trans. Electron Devices*, vol. 38, pp. 1516-1523, Oct. 1991.
- [83] D. Johnsson, W. Mamane, S. Bychikhin, D. Pogany, E. Gornik, and M. Stecher, "Second Breakdown behavior in bipolar ESD Protection Devices during low current long

duration stress and its relation to moving current-tubes”, IEEE International Reliab. Phys. Symp., IRPS, 2008, p. 240-246.

[84] S. Bychikhin was acknowledged for the results of thermal simulation by COMSOL software and the 2D phase images with IV waveforms of oval NPN device.

[85] S. Reggiani, E. Gnani, M. Rudan, G. Baccarani, S. Bychikhin, J. Kuzmik, D. Pogany, E. Gornik, M. Denison, N. Jensen, G. Groos, and M. Stecher, “A new numerical and experimental analysis tool for ESD devices by means of the transient interferometric technique,” IEEE Electron Dev. Lett., vol. 26, pp. 916-918, 2005.

[86] W. Mamanee, S. Bychikhin, D. Johnsson, N. Jensen, M. Stecher, E. Gornik, and D. Pogany, “Effect of elevated ambient temperature on thermal breakdown behavior in BCD ESD protection devices subjected to long electrical overstress pulses”, IEEE TDMR, 2012

[87] H. Gossner, T. M. Lynch, K. Esmark, M. Stecher, “Wide range control of the sustaining voltage of ESD protection elements realized in a smart power technology,” EOS/ESD Symp. 1999, pp. 19-27.

[88] D. Johnsson was acknowledged for the measured voltage of round NPN device.

[89] E. Schöll, Nonequilibrium phase transitions in semiconductors, (Springer, 1987).

[90] A. Alekseev, S. Bose, P. Rodin, E. Schöll, “Stability of current filaments in bistable semiconductor systems with global coupling”, Phys. Rev. E, vol. 57, 1998, pp. 2640-2649.

List of Publications

A. Publications in Journals

- [1] W. Mamanee, S. Bychikhin, D. Johnsson, N. Jensen, M. Stecher, E. Gornik, and D. Pogany, "Effect of elevated ambient temperature on thermal breakdown behavior in BCD ESD protection devices subjected to long electrical overstress pulses", *IEEE Trans. Dev. Mat. Reliab.*, 2011. (Submission of the revised version)
- [2] W. Mamanee, D. Johnsson, P. Rodin, S. Bychikhin, V. Dubec, M. Stecher, E. Gornik and D. Pogany, "Interaction of traveling current filaments and its relation to a non-trivial thermal breakdown scenario in avalanching bipolar transistor", *J. Appl. Phys.*, 2009; **105**: 084501-1-5.
- [3] M. Heer, S. Bychikhin, W. Mamanee, D. Pogany, A. Heid, P. Grombach, M. Klaussner, W. Soppa, B. Ramler: "Experimental and numerical analysis of current flow homogeneity in low voltage SOI multi-finger gg-NMOS and NPN ESD protection devices"; *Microelectronics Reliability*, 47 (2007), S. 1460 - 1465.
- [4] D. Pogany, S. Bychikhin, M. Heer, W. Mamanee, and E. Gornik, "Application of transient interferometric mapping method for ESD and latch-up analysis"; *Microelectronics Reliability*, **51** (2011), S. 1592 - 1596.

B. Conference contributions

- [1] W. Mamanee, S. Bychikhin, D. Johnsson, N. Jensen, N. Stecher, E. Gornik, and D. Pogany, "Effect of Chip Heating on Thermal Breakdown Occurrence in SPT ESD Protection Devices subjected to 0.5-1 μ s Long Current Pulses", *Int. Electrostatic Discharge Workshop* (IEW2009), Lake Tahoe, CA, May 18-21, 2009.
- [2] W. Mamanee, D. Johnsson, S. Bychikhin, M. Stecher, K. Esmark, H. Gossner, E. Gornik, P. Rodin, and D. Pogany, "Pulse risetime effect on current filamentary modes and interaction of current filaments in ESD protection devices", *Proc. Int. Electrostatic Discharge Workshop* (IEW2010), Tutzing, Germany, May 10-13, 2010.
- [3] D. Johnsson, W. Mamanee, S. Bychikhin, D. Pogany, E. Gornik, and M. Stecher, Second breakdown in bipolar ESD protection devices during low current long duration stress and its relation to moving current-tubes. *Proc. IRPS 2008*, April 27-May 1, 2008, Phoenix, USA, p. 240-246.
- [4] D. Pogany, S. Bychikhin, W. Mamanee, E. Gornik, D. Johnsson, K. Esmark, H. Gossner, M. Stecher, P. Rodin, "Interacting traveling current filaments and spreading fronts in sandwiched semiconductor nanostructures"; Talk: 59. Jahrestagung der Österreichischen Physikalischen Gesellschaft, Innsbruck; 09-02-2009 - 09-04-2009; in: "Bulletin SPG/SSP", (2009), 87. *Microelectronics Reliability*, 51 (2011), 1592 - 1596.

[5] D. Pogany, S. Bychikhin, M. Heer, W. Mamanee, V. Dubec, E. Gornik, D. Johnsson, K. Domanski, K. Esmark, W. Stadler, H. Gossner, and M. Stecher, "Application of transient interferometric mapping (TIM) technique for analysis of ns time scale thermal and free carrier dynamics in ESD protection devices"; Poster: Optical localization techniques Workshop, Toulouse; 01-26-2009 - 01-27-2009.

Symbols and Acronyms

A. List of frequently used symbols

Symbol	Unit	Description
φ	[rad]	Phase of Laser beam
$\Delta\varphi$	[rad]	Induced optical phase shift
I_S	[A]	Stress current (Current through the DUT)
L	[μm]	The Ohmic length
n		Refractive index
Δn		Refractive index change
E_{2D}	[nJ. μm^{-2}]	2D thermal energy density
P_{2D}	[mW. μm^{-2}]	Instantaneous 2D power distribution density
τ	[ns]	Time duration of stress pulse
τ_{delay}	[ns]	The added delay time to duration of stress pulse
λ	[nm]	Laser light wavelength
V_{PEAK}	[V]	Voltage peak
V_{CF}	[$\mu\text{m}.\text{ns}^{-1}$]	Speed of moving current filament
T	[$^{\circ}\text{C}$]	Temperature
T_{AMB}	[$^{\circ}\text{C}$]	Ambient temperature of the DUT
$T_{ELEVATED}$	[$^{\circ}\text{C}$]	Elevated DUT temperature by heat chuck
T_{CF}	[$^{\circ}\text{C}$]	Temperature in current filament
T_{CRIT}	[$^{\circ}\text{C}$]	The critical temperature of thermal breakdown
T_{FRONT}	[$^{\circ}\text{C}$]	Temperature at the front-wall of current filament
T_{BACK}	[$^{\circ}\text{C}$]	Temperature at the back-wall of current filament
T_{CF-MAX}	[$^{\circ}\text{C}$]	Maximum temperature in current filament
ΔT	[$^{\circ}\text{C}$]	Temperature change in DUT
S_{2BEAMS}		Distance between dual beams of Michelson Interferometry setup
N		Number of current filaments
I_{TH}	[μA]	Thermally generated current
I_{AV}	[μA]	Avalanche generated current
I_{FAIL}	[μA]	Failure device current
I_{LEAK}	[μA]	Leakage current in the DUT
$\langle J \rangle$	[A. μm^{-1}]	Averaged current density per device width
V_H	[V]	Holding voltage
V_{BD}	[V]	Breakdown voltage
V_{TR}		
V_H	[V]	Holding voltage
$V_{H,1CF}$		Holding voltage of single current filament mode

$V_{H,2CFs}$		Holding voltage of two current filaments mode
W_D	[μm]	Device width of linear DUT
W_{CF}	[μm]	Width of current filament
$y(x,y,t)$		Moving distance of current filament in space and time
t_{IMAGE}	[ns]	Imaging time instant of 2D TIM technique
t_{STAND}	[ns]	Standing time of current filament at its triggered position
t_{DE}	[ns]	Time of current filament to turn around device end
t_{MEET}	[ns]	Meeting time of two moving current filaments
t_{TB}	[ns]	Time to thermal breakdown
t_{TURN}	[ns]	Time of CF to complete a roundtrip distance
t_r	[ns]	Rise time of stress pulse
R_A	[Ω]	Access resistance in buried layer
R_B	[Ω]	Base resistance in bipolar device
S		Starting CF position
D		Disappearance of current filament
M		Meeting event of two current filaments
$P1, P2, \dots$		The order of voltage peak

B. List of Acronyms

Acronyms	Description
BD	Device breakdown
BL	Buried layer
CDM	Charged device model
CF	Current filament
CFs	Multiple current filaments
DE	Device end of linear DUT
DUT	Device under test
ESD	Electro static discharge
HBM	Human body model
IEC	International Electrotechnical Commission
ISO	International Standardization Organization
IV	Current-voltage characteristic
LB	Laser branch
MM	Machine model
NDR	Negative differential resistance
NPN	Bipolar junction transistor
PD	Protection device
SCR	Silicon controlled rectifier
SPT	Smart Power Technology
TB	The (2 nd) thermal breakdown
TIM	Transient Interferometric Mapping
TLP	Transmission line pulse/pulser
YAG	Yttrium Aluminum Garnet laser

Acknowledgement

I would like to acknowledge Prof. Dr. Erich Gornik, the former head of Institute for Solid State Electronics, Vienna University of Technology and Prof. Dr. Emmerich Bertagnolli, the present head of this institute for giving me to conduct until complete the Ph.D study.

I would like to express my gratitude to Assoc. Prof. Dr. Dionyz Pogany for giving me a great opportunity to start the Ph.D study at our institute. I especially acknowledge his crucial guidance in academic research and encouragement he contributed to me as a foreign student over several years.

I want to acknowledge Dr. Sergey Bychikhin for his laboratory instruction, useful discussion, and friendly collaboration during the experiments. Not only that, he also provided me the thermal simulations, incorporated into the scientific journals and this dissertation. I am grateful to my colleagues Dr. Viktor Dubec and Dr. Michael Heer for all suggestions and helpful hands.

Furthermore I am thankful to the collaborative partners of Infineon Technologies AG in Germany, Dr. Matthias Stecher and David Johnsson, for providing the ESD device samples. Additionally, I am overwhelmed with gratitude for the financial support for three years from the Austrian Exchange Service (ÖAD); in which, my Ph.D. study would not have been possible without their organizing. My thanks go to Prof. Nicolas Nolhier for being one of committees on my dissertation jury.

Lastly I want to thank my family profoundly; my parents and brother, who encouraged me in life and supported me become the person I am today.

Biography

Wasinee Mamanee was born in Chiang Mai, Thailand, on October 28th, 1981. She finished the high school at Bunyawat Witthayalai School, in Lampang, Thailand in 1998. She received the Bachelor of engineering from the Department of Electrical engineering, Sirindhorn International Institute of Technology, Thailand, in 2003. She received the Master of engineering in Microelectronics from the school of Advanced Technology, Asian Institute of Technology, Thailand, in 2005. The scope of her master study was the fabrication of bio-MEMS based on the semiconductor fabrication process.

In October 2006, she started the Ph.D. study and joined the group of device characterization of ESD protection device at Institute for Solid State Electronics, Vienna University of Technology, Austria. Her current research focuses on the investigation of current filament behavior and the effect of temperature change leading to the degradation in ESD protection devices under stressing with long duration of HBM-like pulses.